

Department of Physics and Astronomy

University of Heidelberg

Diploma thesis

in Physics

submitted by

Sebastian Erne

born in Wangen i. Allg.

2012

**Characterization of
solitonic states
in a trapped ultracold Bose Gas**

This diploma thesis has been carried out by

Sebastian Erne

at the

Institute of Theoretical Physics

under the supervision of

Prof. Dr. Thomas Gasenzer

Charakteristiken solitonischer Zustände in ultrakalten Bosegasen endlicher Ausdehnung:

In dieser Arbeit werden die Einflüsse von Solitonen auf ein eindimensionales ultrakaltes Bosegas endlicher Ausdehnung untersucht. Wir beschreiben den Zustand eines Gases kurz nach dem Übergang in die kondensierte Phase im Kontext turbulenten Verhaltens. Auf der Grundlage jüngster Entwicklungen im Feld der Vortexdynamik in mehrdimensionalen Systemen beschreiben wir den solitonischen Zustand innerhalb eines erweiterten Modells zufällig verteilter Solitonen. Von besonderem Interesse sind nicht-triviale Effekte auf Grund der endlichen Ausdehnung des Systems. Sie erscheinen in der Impulsverteilung in Form von charakteristischen Multi-peaks. Diese Effekte sind auch hinsichtlich einer experimentellen Bestimmung des solitonischen Zustandes von großer Bedeutung. Wir simulieren die klassischen Bewegungsgleichungen für stochastisch gewählte Anfangszustände numerisch, um Möglichkeiten der Bestimmung des solitonischen Zustandes aufzuzeigen. Untersucht wird der Einfluss von Solitonen auf ein Kondensat bei verschiedenen Temperaturen in einer harmonischen oder anharmonischen Falle auf einem AtomChip. In diesem Zusammenhang werden bei einer Quadrupolanregung des Gases die Messung der Impulsverteilung *im Fokus* und die Steifheit des Kondensates für ein von Defekten dominierten Gas ausführlich diskutiert.

Characterization of solitonic states in a trapped ultracold Bose Gas:

In this thesis the dynamics of solitonic excitations in a finite size ultracold Bose gas in one spatial dimension is studied. This is of great interest in the context of the time evolution of a gas shortly after the near-adiabatic crossover into a Bose-Einstein condensate. In this thesis we propose an interpretation of this state in terms of turbulence. Motivated by recent work on turbulent vortices, the solitonic state is analytically described within an extended model of randomly distributed solitons. Of particular experimental relevance are nontrivial finite size effects found in the momentum distribution, in the form of characteristic multi-peak structures. The possibilities for an experimental observation of the solitonic state are addressed via numerical simulations of, either harmonically or anharmonically confined, condensates at different temperatures. This is done by solving the classical field equations for stochastically sampled initial states on a discrete lattice. In this context the measurement of the momentum distribution *in focus*, in the presence of a quadrupole excitation of the gas, and the stiffness of highly excited states, where the momentum distribution is dominated by the density of the defect, are extensively discussed.

Contents

1	Introduction	1
2	Theoretical Background	5
2.1	One-dimensional cold quantum gases	5
2.1.1	Bogoliubov theory for quasicondensates	6
2.1.2	Experimental realization	12
2.2	The Truncated-Wigner method	14
3	Solitons	17
3.1	Solitonic solution	17
3.2	Interaction of solitons	20
3.3	Movement in traps	22
4	Random soliton model	25
4.1	Analytic derivation of the spectrum	25
4.2	Scaling analysis	29
4.3	Comparison with grid simulations	30
4.3.1	Homogeneous background density	30
4.3.2	Inhomogeneous background density	35
4.4	Double peak structure of the spectrum	37
5	Experimental characterization of solitonic states	45
5.1	Experimental setup and initial state	45
5.2	Measurement of the single-particle momentum distribution	47
5.3	Time evolution	50
5.3.1	Condensate regime	51
5.3.2	Quasicondensate regime	58
5.3.3	Many soliton state	60
6	Discussion and outlook	65
A	Appendix	69
A.1	Expansion of the Hamiltonian	69
A.2	Sampling of the Wigner distribution	69
A.3	Dimensionless GPE	70
A.4	Split Operator method	71
A.5	Detection algorithm for solitons	71

1 Introduction

Nowadays, over eighty years after the proposal of Bose-Einstein condensation by Styrendranath Bose and Albert Einstein [12, 20] in 1924, ultracold atomic gases are considered a perfect model system for the investigation of fundamental quantum physics. Because a large number of atoms occupy the same quantum state, quantum phenomena can be studied on a macroscopic scale. Since the first creation of a Bose-Einstein condensate (BEC) in a laboratory in 1995 [2, 18] huge progress has been made in the creation and manipulation of BECs. The development of experimental techniques has for example enabled scientists to investigate BECs in highly anisotropic trapping potentials. Due to a strong confinement in selected spatial dimensions, the dynamics in these higher dimensions are frozen out and the system behaves one- or two-dimensional respectively. Trapping techniques such as *e.g.* magneto-optical traps, where the splitting of the internal Zeeman levels of an atom by an anisotropic magnetic field leads to a spatially dependent absorption rate of counterpropagating laser beams [27, 48], and therefore a force towards the center of the trap, or atom chips [24, 23, 59], where strong electromagnetic fields confine the gas above the surface of a chip, are commonly used. The latter has the advantage that it allows for a fast and stable creation of the condensate and precise manipulation of the trapping potential.

In one-dimensional systems it is of particular interest to investigate finite size systems. Although a second order phase transition, which is defined in the thermodynamic limit, does not exist in one dimension, Ketterle and van Durten [31] proved that for a finite size system below a certain temperature the occupation number of the ground state grows rapidly. This is consistent with the quasicondensate theory, introduced by Popov [52], which states that phase coherence can be established on a length scale of the order of the thermal coherence length. For a finite size system at sufficiently low temperatures it can exceed the size of the cloud. Therefore a BEC can be created even in one dimension. Understanding the finite size effects is also very important, because compared to the thermodynamic limit nontrivial effects can occur.

To date, one of the most active branches in the investigation of ultracold Bose gases is the dynamics of non-equilibrium systems. Many-body states far away from the thermal equilibrium can show a much wider range of characteristics than equilibrium systems. Fundamental questions, such as the relaxation to thermal equilibrium, the possibility and characterization of transient states, and the influence of topological excitations are of great interest for a wide range of physical situations spanning from the inflation of the early universe [39, 7], strongly correlated matter produced in heavy-ion collisions [3, 5, 43] to the formation of Bose-Einstein condensates [1, 6, 44]. Among the wealth of possible non-equilibrium configurations the

most interesting for theoretical and experimental studies are those at which generic-time evolutions get stuck for an extraordinarily long time. Critical points far from equilibrium, so-called nonthermal fixed points, are connected to the emergence of universal properties like power-law behavior of correlation functions. An interesting question is how they are related to the emergence and dynamics of topological defects [45, 25, 46, 57].

For classical turbulence Richardson first described the energy transport in the form of a cascade [54], where large eddies split up into smaller ones until a length scale is reached where the energy dissipates and the system reaches the thermal state. In his paper from 1941 Kolmogorov [35] derived the famous $k^{-5/3}$ -law for the energy spectrum of the turbulent state, based on the assumption of self-similarity. Turbulent states in a superfluid system, called superfluid turbulence or quantum turbulence, have been the subject of intensive studies in the context of helium [28, 19]. Compared to classical turbulence the picture changes drastically, because the topological defects are quantized objects found in the form of vortices and vortex-lines in two and three dimensions. Due to this quantization, the creation and annihilation processes are distinctly different. Important progress has been recently made in understanding these turbulent states, from the prediction of power-laws for the momentum distribution out of a non-perturbative quantum field method [1] to the connection of these power-laws to the vortical excitations [45, 25, 46]. Defects in a one dimensional Bose gas are found in the form of solitons. In contrast to vortices, these can continuously be deformed into the ground state. This shows the essential difference between turbulence in one- and multi-dimensional systems, making them an important and fascinating subject of investigation. In this thesis we propose the possibility of a non-thermal fixed point, connected to the solitonic excitations. It is shown to exist through the emergence of a transient power-law behavior of the momentum distribution derived with a model of randomly distributed solitons and confirmed by numerical simulations [57]. The Random Soliton Model was inspired by the point-vortex model from Onsager [47], and used by Rajantie and Tranberg [53], who studied non-equilibrium dynamics in relativistic field theories, and developed such a model for solitonic kinks in a free gas.

The creation of solitons can be achieved in different ways, among them are the collision of condensates [66], an interaction quench or a second order phase transition. The last is described by the Kibble-Zurek mechanism (KZM) which states that the number of defects created during a near-adiabatic phase transition depends on the crossing rate [71, 72]. The predicted power-law behaviour, which depends on the universal properties of the transition, was observed in [67]. Recent developments suggest that solitons can also occur spontaneously in a thermal system [30], which seems plausible as solitons are continuously connected to the ground state. This shows that it is of great relevance to understand the impacts of solitonic excitations on a ultracold Bose gas.

In general the equations of motion of a many-body system become too complex to be solved analytically. It is therefore necessary to develop simplified models that describe certain aspects of their properties correctly or to solve the equations by

numerical simulations. In this thesis both methods are applied. We give an extension of the Random Soliton Model to the case of a finite size of the system and to solitons with an arbitrary value of the greyness $\nu = v_s/c_s$, where c_s is the Bogoliubov speed of sound. The latter allows for comparison with experiments of harmonically confined gases where the soliton velocity v_s is no longer preserved. Furthermore we show that for a solitonic state the finite size of the system exhibits nontrivial effects for different observables in particular the one body momentum distribution. It is pointed out that under certain constraints the momentum distribution shows a characteristic multi-peak structure. The model is verified by comparing it to numerical simulations on a grid. In addition we study an experiment, done by the group of Prof. Schmiedmayer in Vienna [58, 13], by using numerical simulations in the condensate and quasicondensate regime to show how these effects can be measured. In this context we investigate important experimental questions regarding the effects of a anharmonicity of the trapping potential and the measurement protocol to gain the momentum distribution. For the former we find a characteristic double peak structure when a quadrupole excitation of the gas is present. For the latter we reproduce the results of Shvarchuck *et al.* [61], who derived a formula for momentum distribution measurement *in focus*. Finally, the dynamics of highly excited solitonic states are analyzed leading to the so called stiffness of the condensate, where the quadrupole excitation vanishes.

Outline

In **Chapter 2** we present the first part of the theoretical background. First we give a brief overview of one dimensional cold quantum gases based on the exactly solvable Lieb-Liniger model. Then the quasicondensate regime is described in detail using an extended Bogoliubov approach in phase-density representation of the field. The validity of the equations for quasi-one dimensional systems are briefly discussed. Thereafter, the theoretical framework of our numerical simulations, namely the Truncated-Wigner method, is described. **Chapter 3** deals with the basic equations of solitons, regarding their analytical solution, interaction and movement in traps. The concept of the soliton phase space is introduced. In **Chapter 4** we derive the extended version of the Random Soliton Model. It is compared to grid simulations in several cases. The last part of this chapter addresses the effects caused by the finite size of a system, and explains the emergence of the double peak structure. In **Chapter 5** we show the results of the numerical simulations for an experimental setup on an atom chip. We explain the measurement of the momentum distribution via free expansion of the cloud and the measurement in focus. The time evolution for a gas with a quadrupole excitation at different temperatures and different soliton numbers as well as harmonical or anharmonical confinement are compared. Finally, the case of highly excited states are discussed.

2 Theoretical Background

Bose-Einstein condensation in $d < 3$ dimensions differs drastically from the three dimensional case, in which there is true long-range order in the one-body density matrix below the critical temperature $T_c^{d=3}$, see *e.g.* [51, 48]. In the thermodynamic limit, the Hohenberg inequality [38, 29] rules out the existence of a true condensate at finite temperature for $d < 3$ dimensions. For $d = 2$ this true long-range order is preserved at absolute zero temperature, whereas for $d = 1$ even at $T = 0$ no perfect phase coherence can be established. This means that in a one-dimensional system in the thermodynamic limit there is no second order phase transition. However Ketterle and van Durten [31] have established that at temperatures $T < N\hbar\omega/\ln(2N)$ the population of the ground state grows rapidly for a harmonically confined ideal gas of N atoms. In this section we will see, that for a weakly interacting gas at sufficiently low temperatures, density fluctuations are suppressed whereas the phase fluctuations are not and the system is in the so called quasicondensate regime, introduced by Popov [52].

2.1 One-dimensional cold quantum gases

Before we start with an analytical mean field description of the quasicondensate, which is the relevant state for this thesis, we give, for completion, an overview of the different regimes of a one-dimensional Bose gas.

Lieb and Liniger [37], [36] obtained an exact solution of the many-body problem for a one-dimensional uniform Bose gas with repulsive interaction, considering the Hamiltonian

$$H_{\text{LL}} = -\frac{\hbar^2}{2m} \sum_{j=1}^N \frac{\partial^2}{\partial z_j^2} + g_{1D} \sum_{1 \leq i < j \leq N} \delta(z_i - z_j) , \quad (2.1)$$

which can be solved by a Bethe-Ansatz [8]. Yang and Yang [68] used a thermodynamic Bethe-Ansatz to describe finite-temperature systems in equilibrium. It is useful to define the degeneracy temperature:

$$T_d = \frac{\hbar^2 \rho_{1D}^2}{2mk_B} , \quad (2.2)$$

for which the thermal de-Broglie wavelength $\lambda_T = \sqrt{2\pi\hbar^2(mk_B T)^{-1}}$ becomes of the order of the mean particle separation (ρ_{1D}^{-1}). For $T < T_d$, quantum statistics apply and we can characterize the state depending on the strength of the coupling

constant. Further, the dimensionless Lieb-Liniger parameter is defined as

$$\gamma_{\text{LL}} = \frac{mg_{1\text{D}}}{\hbar^2 \rho_{1\text{D}}} , \quad (2.3)$$

denoting the mean particle separation in units of the interaction length ($\hbar^2/mg_{1\text{D}}$). The Lieb-Liniger parameter shows the counter-intuitive fact that interactions in a one-dimensional system become more dominant with decreasing density. With the aid of γ_{LL} we can now identify two different regimes for $T < T_d$.

- **strongly interacting regime ($\gamma_{\text{LL}} \gg 1$):**

The system is in the Tonks-Girardeau limit [65] [26] where the so called 'fermionization'-effect takes place. Due to the strong repulsive interactions the atoms cannot be in the same place in space and thus the system exhibits Fermi-like features. In contrast to a fermionic system, occupancy of the same momentum-modes are still allowed [65] [26]. In this regime every atom has to be described by a different wave function, therefore a mean field description is not possible.

- **weakly interacting regime ($\gamma_{\text{LL}} \ll 1$):**

For $T \ll T_d$ density fluctuations are greatly suppressed by the repulsive interaction and the system is in the so called quasicondensate regime. As the temperature rises the system enters the quantum decoherent regime, where density fluctuations are no longer negligible, and the system is close to the classical thermal decoherent regime ($T \gg T_d$). For very low temperatures even phase fluctuations are suppressed on a length scale $l_0(T)$, showing that it is possible in one dimension to create a true condensate in a finite size system.

We will now give a qualitative description of the quasicondensate regime in a mean field picture with an extended Bogoliubov approach, which was confirmed to be valid for weakly interacting one dimensional systems [37] [36] [41]. The conditions for the validity of the mean field description and a calculation for the one-dimensional coupling constant $g_{1\text{D}}$ for an actual experiment will be addressed in the last part of this section, where we will discuss how quasi-one-dimensional systems can be achieved for realistic trapping potentials.

2.1.1 Bogoliubov theory for quasicondensates

We consider a dilute system of N scalar bosons in a potential $V(z)$. In the case of a weakly interacting gas, where three-body interactions can be neglected, the microscopic interaction potential can be replaced by an effective, soft potential, which in the low-energy limit (s-wave scattering regime) reduces to

$$U(z_1 - z_2) = g_{1\text{D}} \delta(z_1 - z_2) . \quad (2.4)$$

The effective one-dimensional coupling constant for a realistic trapping potential will be computed later on. Be reminded that it is not the same as the three-dimensional

$g_{3D} = 4\pi\hbar^2 a_s/m$, with the s-wave scattering length a_s , obtained in the low-energy limit of the partial wave expansion. The grand canonical Hamiltonian becomes

$$\hat{H} = \int dz \hat{\psi}^\dagger(z) \left[-\frac{\hbar^2}{2m} \partial_z^2 + V(z) - \mu + \frac{g_{1D}}{2} \hat{\psi}^\dagger(z) \hat{\psi}(z) \right] \hat{\psi}(z) . \quad (2.5)$$

The intuitive idea of the Bogoliubov theory, in the $U(1)$ -symmetry preserving version [16], is to split the bosonic field operator as $\hat{\psi} = \phi_0 \hat{a}_0 + \delta\hat{\psi}$, where ϕ_0 is a macroscopically occupied mode of the field (condensate mode), \hat{a}_0 is the annihilation operator of the condensate mode, and $\delta\hat{\psi}$ compensates the quantum and thermal fluctuations in the other modes. Under the assumption that the mean number of non-condensed particles is much smaller than the number of condensed particles $\langle \delta\hat{N} \rangle \ll |N_0| \simeq N$, one can solve the field equations of motion perturbatively in orders of $\sqrt{\langle \delta\hat{N} \rangle / N}$. Unfortunately, because there is no macroscopically occupied field mode this approach is not applicable to the quasicondensate regime. However, in the case of weak density-fluctuations, an extended Bogoliubov approach can still be used in the phase-density representation of the field

$$\hat{\psi}(z) = \sqrt{\hat{\rho}(z)} e^{i\hat{\Theta}(z)} , \quad (2.6)$$

with the density and phase operator defined as

$$\begin{aligned} \hat{\rho}(z) &= \hat{\psi}^\dagger(z) \hat{\psi}(z) , \\ [\hat{\rho}(z), \hat{\Theta}(z')] &= i\delta(z - z') . \end{aligned} \quad (2.7)$$

We present the results of Mora and Castin [41], who proposed an improved Bogoliubov approach for quasicondensates. Their approach is based on a lattice model, for which it is possible to give a careful definition of the phase-operator. Whereas for a continuous description one has to introduce an arbitrary energy cutoff to prevent divergences, due to the non-rigorous definition of the phase, the lattice model enables one to introduce an energy cutoff from the beginning of the calculation.

Before starting with the perturbative expansion of the Hamiltonian, we give a definition of the lattice model. The results can also be directly applied to the numerical simulations presented in Chaps. (4 & 5). The discretization of the space is done by collecting all particles on a length scale l at the nodes of the spatial grid. As a consequence we get the discrete expressions

$$\begin{aligned} z &\rightarrow jl \quad \text{with } z \in \mathbb{Z} \\ \delta(z - z') &\rightarrow \frac{\delta_{zz'}}{l} \\ \partial_z f(z) &\rightarrow \frac{f(z + l) - f(z - l)}{2l} \\ \partial_z^2 f(z) &\rightarrow \frac{f(z + l) + f(z - l) - 2f(z)}{l^2} . \end{aligned} \quad (2.8)$$

Furthermore we get a coarse-grained average over all physical quantities, hence an energy cutoff

$$E_{\text{cut}} = \frac{\hbar^2}{ml^2} . \quad (2.9)$$

To ensure the independence of the solution on the cutoff, all characteristic energies ($\mu, k_B T$) have to be smaller than E_{cut} which coincides with l being smaller than the corresponding characteristic length scales. This leads to

$$l < \xi \quad \text{and} \quad l < \lambda_T , \quad (2.10)$$

with the healing length $\xi = \hbar/\sqrt{m\mu}$ and the thermal de-Broglie wavelength λ_T . With the assumption of small density fluctuations ($\text{Var}[\hat{\rho}(z)] \ll \langle \hat{\rho}(z) \rangle^2$) we get the restrictions

$$\begin{aligned} 1 &\ll \rho(z)\lambda_T \sim \frac{T_d}{T} \\ 1 &\ll \rho(z)\xi \sim \gamma_{LL}^{-2} , \end{aligned} \quad (2.11)$$

where $\rho(z) = \langle \hat{\rho}(z) \rangle$ is the mean density. The terms on the right hand side show the connection to the Lieb-Linger model. We see that the theory is applicable for a weakly interacting gas with a temperature well below the degeneracy temperature T_d . On the other hand the definition of an approximately hermitian operator $\hat{\Theta}(z)$ fulfilling the discrete version of the commutation relation (2.7), which does not exist exactly, requires that we have a large mean number of particles in every box of length l . Since this becomes problematic for $l \rightarrow 0$ there is a lower boundary for the lattice spacing.

Having properly defined the spacial lattice we can now write the Hamiltonian (2.5), by using (2.6) and (2.8), in density-phase representation on a lattice

$$\begin{aligned} \hat{H} = \sum_z l &\left[-\frac{\hbar^2}{2ml^2} \sqrt{\hat{\rho}_z} (e^{i(\hat{\Theta}_{z+l}-\hat{\Theta}_z)} \sqrt{\hat{\rho}_{z+l}} + e^{i(\hat{\Theta}_{z-l}-\hat{\Theta}_z)} \sqrt{\hat{\rho}_{z-l}} - 2\sqrt{\hat{\rho}_z}) \right] \\ &+ \left[\hat{\rho}_z \left(V(z) - \mu + \frac{g_{1D}}{2} (\hat{\rho}_z - \frac{1}{l}) \right) \right] . \end{aligned} \quad (2.12)$$

In the quasicondensate regime we can write the density operator as

$$\hat{\rho}(z) = \rho_0(z) + \delta\hat{\rho}(z) , \quad (2.13)$$

where $\rho_0(z)$ will be given by the zeroth order of the expansion of the Hamiltonian and $\delta\hat{\rho}(z)$ are small density fluctuations. Now we can define the small parameters for the perturbative expansion, namely

$$\kappa_1 = \frac{|\delta\hat{\rho}|}{\rho_0} \ll 1 \quad \text{and} \quad \kappa_2 = |l\partial_z \hat{\Theta}| \ll 1 , \quad (2.14)$$

where $|\star|$ denotes the typical value. Physically this means that we have small den-

sity fluctuations as compared to ρ_0 and small phase fluctuations on a length scale of l . It can be shown that κ_1 and κ_2 can be chosen to be of the same order of magnitude, therefore they contribute to the same order in the systematic expansion of the Hamiltonian. We expand the Hamiltonian to second order in these parameters to determine the density and phase fluctuations. Here only the results of the calculation are presented, and the expansion of the Hamiltonian is given in Appendix (A1). The zeroth order in $\kappa_{1,2}$ determines the density profile ρ_0 , the mean field solution, by the condition that $\sqrt{\rho_0}$ solves the discrete version of the Gross-Pitaevskii equation (GPE)

$$\left[-\frac{\hbar^2}{2m} \partial_z^2 + V(z) - \mu + g_{1D}\rho_0 \right] \sqrt{\rho_0} = 0 . \quad (2.15)$$

This equation is of particular interest, as it is the basis of our classical field description described in the next section. The numerical schemes are given in Appendix A2 and A3. The first order correction to the Hamiltonian vanishes due to (2.15). In second order, by using the Heisenberg equation of motions for $\hat{\Theta}$ and $\delta\hat{\rho}$ and the GPE, we can introduce the canonical transformation

$$\hat{B} = \frac{\delta\hat{\rho}}{2i\sqrt{\rho_0}} + \sqrt{\rho_0}\hat{\Theta} , \quad (2.16)$$

which maps the equations for a quasicondensate into the Bogoliubov equations

$$i\hbar\partial_t \begin{pmatrix} \hat{B} \\ \hat{B}^\dagger \end{pmatrix} = \mathcal{L}_{\text{GP}} \begin{pmatrix} \hat{B} \\ \hat{B}^\dagger \end{pmatrix} , \quad (2.17)$$

with

$$\mathcal{L}_{\text{GP}} = \begin{pmatrix} -\frac{\hbar^2}{2m}\partial_z^2 + V(z) - \mu + 2g_{1D}\rho_0 & -g_{1D}\rho_0 \\ g_{1D}\rho_0 & -\left(-\frac{\hbar^2}{2m}\partial_z^2 + V(z) - \mu + 2g_{1D}\rho_0\right) \end{pmatrix} . \quad (2.18)$$

This shows that the standard diagonalization of the Bogoliubov Hamiltonian can be applied [11, 16]. One introduces the normal eigenmodes (u_j, v_j) of the operator \mathcal{L}_{GP} with energy ϵ_j along with the bosonic quasiparticle creation and annihilation operators \hat{a}_j^\dagger and \hat{a}_j with the usual commutation relation $[\hat{a}_j, \hat{a}_{j'}^\dagger] = \delta_{j,j'}$. Therefore the modes are normalized according to

$$\sum_z l [|u_j(z)|^2 - |v_j(z)|^2] = 1 . \quad (2.19)$$

With these definitions one can express the operators $(\hat{B}, \hat{B}^\dagger)$ in the quasiparticle eigenmodes

$$\begin{pmatrix} \hat{B} \\ \hat{B}^\dagger \end{pmatrix} = \sum_j \begin{pmatrix} u_j \\ v_j \end{pmatrix} \hat{a}_j + \begin{pmatrix} v_j^* \\ u_j^* \end{pmatrix} \hat{a}_j^\dagger , \quad (2.20)$$

where the contributions of the zero-energy mode and the anomalous mode of the

$U(1)$ -symmetry preserving Bogoliubov approach are neglected. This is justified, because we are interested in a canonical ensemble, *i. e.* a gas with a fixed number of atoms, rather than the grand canonical ensemble, where fluctuations of the total number of atoms give rise to an additional term in the Hamiltonian. With the use of Eq. (2.16) and the explicit solution of Eq. (2.18) it is now possible to derive an expression for the density and phase fluctuations:

$$\begin{aligned}\delta\hat{\rho}(z) &= \sum_j \delta\rho_j(z)\hat{a}_j + \text{H.c.} \\ \hat{\Theta}(z) &= \sum_j \Theta_j(z)\hat{a}_j + \text{H.c.},\end{aligned}\tag{2.21}$$

with

$$\begin{aligned}\delta\rho_j(z) &= \sqrt{\rho_0(z)}i[u_j(z) - v_j(z)] \\ \Theta_j(z) &= \frac{1}{2\sqrt{\rho_0(z)}}[u_j(z) + v_j(z)].\end{aligned}\tag{2.22}$$

Solutions are given in the Thomas-Fermi (TF) regime, of a harmonically confined gas. We insert the potential

$$V(z) = \frac{1}{2}m\omega^2 z^2\tag{2.23}$$

into the Eq. (2.15) and (2.18). By neglecting the kinetic term, which is the usual TF approximation, we can solve the equations and get in first order the mean field density profile of the TF condensate

$$|\psi_0(z)|^2 = \rho_0(z) = \frac{1}{g_{1D}}[\mu_{\text{TF}} - V(z)] = n \left[1 - \left(\frac{z}{R_{\text{TF}}}\right)^2\right]\tag{2.24}$$

if $\mu_{\text{TF}} > V(z)$ and zero elsewhere, with the peak density $n = \mu_{\text{TF}}/g_{1D}$ and the TF-radius $R_{\text{TF}}^2 = 2\mu_{\text{TF}}/m\omega^2$. The chemical potential is fixed by imposing the normalization condition $\sum_z \rho_0(z) = N$, with the total number of particles N , and is given by

$$\mu_{\text{TF}} = \left[\frac{3}{4}\sqrt{\frac{m}{2}}g_{1D}\omega N\right]^{\frac{2}{3}}.\tag{2.25}$$

In the case of a harmonic potential the TF density profile takes the form of an inverted parabola. Physically it represents a state where the energy required to add a particle is the same everywhere in the cloud. By inserting the mean field solution into Eq. (2.18) we get two coupled differential equations for (u_j, v_j) , which, by substituting $f_j^\pm = u_j \pm v_j$, can be solved by

$$f_j^\pm(\tilde{z}) = \left(\frac{j + \frac{1}{2}}{R_{\text{TF}}}\right)^{\frac{1}{2}} \left[\frac{2\mu_{\text{TF}}(1 - \tilde{z}^2)}{\epsilon_j}\right]^{\pm\frac{1}{2}} P_j(\tilde{z}),\tag{2.26}$$

where $j \in \mathbb{N}$, P_j are Legendre polynomials, $\tilde{z} = z/R_{\text{TF}}$, and the spectrum of the quasiparticle excitations is given by

$$\epsilon_j = \hbar\omega \sqrt{\frac{j(j+1)}{2}} . \quad (2.27)$$

This allows us to write down the operators for the density and phase fluctuations [60]

$$\begin{aligned} \delta\hat{\rho}(z) &= \sqrt{\rho_0(z)} \sum_{j=1}^{\infty} i f_j^-(\tilde{z}) \hat{a}_j + \text{H.c.} \\ \hat{\Theta}(z) &= \frac{1}{2\sqrt{\rho_0(z)}} \sum_{j=1}^{\infty} f_j^+(\tilde{z}) \hat{a}_j + \text{H.c.} . \end{aligned} \quad (2.28)$$

The equations above allow us to study the influence of temperature on the density and phase fluctuations [49]. Since the operators $\hat{a}_j, \hat{a}_j^\dagger$ have the usual bosonic commutation relations, the thermal occupation number for the excitations is given by $N_j = [\exp(\epsilon_j/k_B T) - 1]^{-1}$. The vacuum contribution for the mean square fluctuations of the density and the phase are of the order of $\sqrt{\gamma_{\text{LL}}}$ and are therefore small for any realistic size of the cloud. The thermal fluctuations of the density on a length scale $|z - z'| \gg \xi$ are found to be $\langle [\delta\hat{\rho}(z) - \delta\hat{\rho}(z')]^2 \rangle_T \approx n^2(T/T_d)\min\{(T/\mu), 1\}$ and are highly suppressed if $T \ll T_d$. Thus for sufficiently low temperatures the total field operator can be written as

$$\hat{\psi}(z) = \sqrt{\rho_0} e^{i\hat{\Theta}(z)} , \quad (2.29)$$

with ρ_0 being the solution of the mean field GPE (2.15) given by Eq. (2.24) and the phase operator (2.28). The state has the same density-density correlations as a pure condensate. In accordance with the absence of a true condensate in one dimension, the one-body density matrix does not show a true long range order, but is, under the assumption that mostly the lowest excitations contribute to the fluctuations of the phase ($N_j \simeq k_B T/\epsilon_j$), given by [49][52]

$$\begin{aligned} g_1(z, z') &= \langle \hat{\psi}^\dagger(z) \hat{\psi}(z') \rangle = \sqrt{\rho_0(z)\rho_0(z')} e^{-\langle [\hat{\Theta}(z) - \hat{\Theta}(z')]^2 \rangle/2} , \\ \text{with} \quad \langle [\hat{\Theta}(z) - \hat{\Theta}(z')]^2 \rangle &= \frac{4T\mu_{\text{TF}}}{3T_d\hbar\omega} \left| \log \left[\frac{(1-\tilde{z}')(1+\tilde{z})}{(1+\tilde{z}')(1-\tilde{z})} \right] \right| . \end{aligned} \quad (2.30)$$

However for sufficiently low temperatures $T < T_\Theta = T_d\hbar\omega/\mu_{\text{TF}}$ the mean square of the phase fluctuations are approximately one on a length scale $|z - z'| \sim R_{\text{TF}}$. Thus for $T \ll T_\Theta$ phase fluctuations are suppressed on a length scale that exceeds the spatial width of the cloud and there is a true condensate in the finite size system. In the following we are interested in the behavior of the gas at low temperatures ($T \ll T_d$), where only phase fluctuations are present. A state with $T_\Theta < T \ll T_d$

is referred to as a thermal state, whereas for $T \ll T_\Theta$ the gas is considered a true condensate. In Fig. (2.1) we show the phase of a single realization and the normalized first order correlation function $g_1(0, z)/\sqrt{\rho_0(0)\rho_0(z)}$ averaged over 5000 realizations for different temperatures $T \ll T_d$. Phase fluctuations become stronger as the temperature rises and lead to a sharp decrease of g_1 . In accordance with Eq. (2.28) the fluctuations become stronger as the density decreases, which diminishes the coherence and leads to the additional decrease of g_1 for $z \rightarrow 1$ as compared to the homogenous case. This effect becomes less important with rising temperature since there is no phase coherence for distances well below the TF-radius.

2.1.2 Experimental realization

Huge progress has been made in the last decades in the creation of Bose-Einstein condensates in highly anisotropic traps. It has become possible to investigate quasi one- and two-dimensional systems. A quasi one-dimensional system is given by a strong axial confinement ω_\perp in two directions, here chosen in x - and y -direction, and a soft longitudinal confinement $V(z)$. If the system fulfills $\mu, k_B T \ll \hbar\omega_\perp$ all the atoms are in the transversal ground state. With all the transversal excitations frozen out, the system behaves like a one-dimensional system with a ω_\perp -dependent coupling constant. The effective one-dimensional classical field equation can be found by choosing a trial wave function

$$f(\mathbf{r}, t) = \phi(x, y, t, \sigma(z, t))\psi(z, t) = \frac{e^{-(x^2+y^2)/2\sigma^2(z, t)}}{\sqrt{\pi}\sigma(z, t)}\psi(z, t), \quad (2.31)$$

where we make the ansatz of a gaussian wave function in the transversal directions. Requiring stationarity of the classical action functional,

$$S[\psi] = \int dt d\mathbf{r} \psi^*(\mathbf{r}, t) \left[i\hbar\partial_t + \frac{\hbar}{2m} \nabla^2 + V(\mathbf{r}) - \frac{g_{3D}}{2} |\psi(\mathbf{r}, t)|^2 \right] \psi(\mathbf{r}, t), \quad (2.32)$$

after integration along x and y , leads to the relation $\sigma = \sigma(\psi)$ and a nonpolynomial nonlinear Schrödinger equation (NPSE) for $\psi(z, t)$ [55, 50]. In general this equation has to be solved numerically, but given the limit of a weakly interacting gas $a_s n_{1D} \ll 1$ all atoms are in the transversal gaussian ground state and, with $\sigma^2 = a_\perp^2 = \hbar/m\omega_\perp$, the NPSE reduces to the effective one-dimensional GPE (2.15) with the coupling constant given by

$$g_{1D} = 2\hbar a_s \omega_\perp. \quad (2.33)$$

The condition for the validity of the GPE (2.11), states that the healing length ξ is much larger than the mean inter-particle distance. In the case of a harmonic confinement $V(z) = 1/2m\omega_\parallel^2 z^2$ for a quasi-one dimensional system of N particles this takes the form

$$N \frac{\omega_\parallel}{\omega_\perp} \left(\frac{a_\perp}{a_s} \right)^2 \gg 1. \quad (2.34)$$

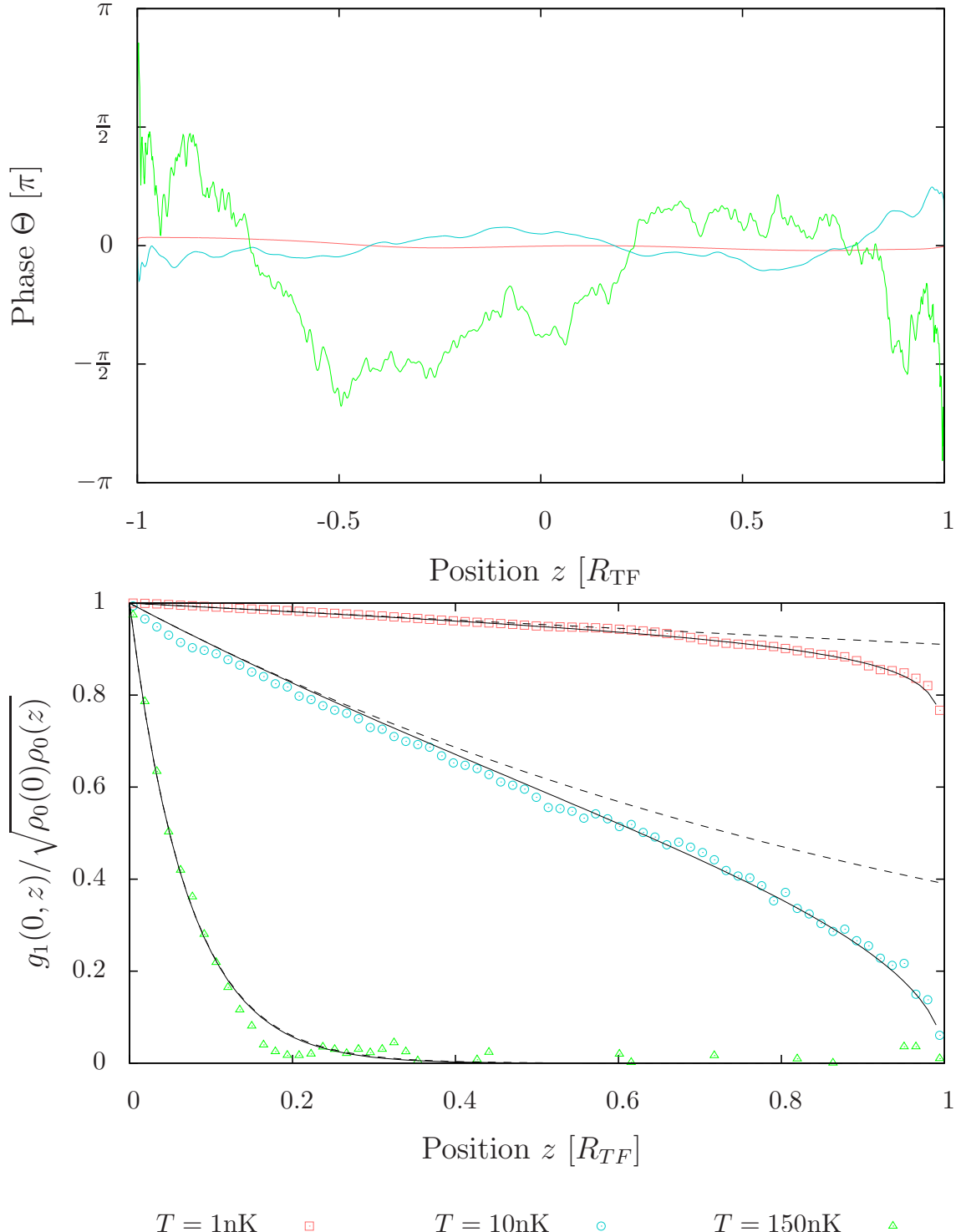


Figure 2.1: Bose gas in the TF regime at finite temperature. Upper picture: Phase of the field in a single realization for different temperatures, the phase fluctuations increase as the temperature rises; Lower picture: Normalized first order coherence function $g_1(0, z) / \sqrt{\rho_0(0)\rho_0(z)}$ for different temperatures with the analytical predictions of the Bogoliubov approach (2.30) (solid lines), note the decrease for $z \rightarrow 1$ due to the decrease of the density. For comparison the corresponding curves for a homogenous system are displayed (dashed lines).

2.2 The Truncated-Wigner method

The truncated Wigner approximation (TWA) is based on the phase space dynamics of quantum mechanics, pioneered by Moyal [42]. See *e.g.* [51, 9, 62] for a review. For ordinary canonical variables, like coordinates and momenta, any operator can, by a so called Weyl-transformation, be mapped onto an ordinary function in phase space, often called the Weyl symbol of the operator. The Weyl-transformation of the density matrix $\hat{\rho}$ is defined as the Wigner distribution, which plays the role of a classical probability distribution. In contrast to the latter the Wigner distribution is not positively definite and can therefore not be itself interpreted as a probability. The Wigner distribution, together with the Weyl symbols of a number of operators, gives a complete description of the system. This concept can be extended to a many-body system for which the TWA is defined as the coherent state representation of the phase space in the leading semiclassical order (first order in \hbar). Using coherent states, the Weyl symbol of an operator $\hat{A}(\hat{\psi}^\dagger, \hat{\psi})$ is given by

$$a_W(\psi, \psi^*) = \int d\phi d\phi^* \langle \psi - \frac{\phi}{2} | \hat{A}(\hat{\psi}^\dagger, \hat{\psi}) | \psi + \frac{\phi}{2} \rangle e^{-|\psi|^2 + \frac{1}{2}(\phi^*\psi - \phi\psi^* - \frac{1}{4}|\phi|^2)}, \quad (2.35)$$

where the components of the vector $\psi = \{\psi_j\}$ are the complex amplitudes of the single particle eigenstates. The Wigner function $W(\psi, \psi^*)$ is defined as the Weyl symbol of the density matrix. The time evolution of the Wigner function is given by the Weyl-transform of the Neumann-equation

$$i\hbar \partial_t \hat{\rho} = [\hat{H}, \hat{\rho}] . \quad (2.36)$$

The TWA is to expand this equation up to first order in \hbar , where it reduces to the Liouville equation

$$i\hbar \partial W \approx \{H, W\}_c = \sum_j \left(\frac{\partial H}{\partial \psi_i} \frac{\partial W}{\partial \psi_i^*} - \frac{\partial W}{\partial \psi_i} \frac{\partial H}{\partial \psi_i^*} \right) . \quad (2.37)$$

The expectation value of any operator can now be calculated through

$$\langle \hat{A}(\hat{\psi}^\dagger, \hat{\psi}) \rangle_t = \int d\psi d\psi^* W(\psi, \psi^*, t) A_W(\psi, \psi^*) . \quad (2.38)$$

Since we want to numerically evolve the fields in time, it is useful to calculate the expectation value in the Heisenberg picture,

$$\langle \hat{A}(\hat{\psi}^\dagger, \hat{\psi}, t) \rangle = \int d\psi_0 d\psi_0^* W_0(\psi_0, \psi_0^*) A_W(\psi(t), \psi^*(t)) . \quad (2.39)$$

As can be seen from the Liouville equation the time evolution of $\psi(t)$ is given by the GPE. For many important classes of quantum states the Wigner function is positive (or well approximated by a positive function). We can therefore sample an initial

state according to the Wigner distribution, evolve the field along a trajectory given by the GPE, compute the observable, and average over many realizations to get the expectation value. As the numerical integration of the GPE can be implemented easily (see Appendix A3, A4), this method is feasible and very accurate for high occupation numbers $n(k)$.

An important aspect of the Wigner representation is that it goes beyond mean field, as half a particle of quantum noise is added to every mode to mimic quantum fluctuations. This can be seen by calculating *e.g.* $\langle \psi^* \psi \rangle_W$. In the phase space representation this reflects the fact that the Wigner distribution always has a finite width that must at least fulfill the uncertainty principle. Due to this uncertainty one has to restrict the modes taken into account to avoid divergencies by *e.g.* considering a lattice model [62] or introducing a c-field region which has a finite amount of modes and evolves according to the classical GPE equation [9]. The TWA considers the condensed part as well as the excited states combined in a single field, which enables us to safely use it in the quasicondensate regime. The explicit form of the Wigner distribution for the Bogoliubov formalism can be found in Appendix A2.

The validity of the classical equations of motion was also derived by Berges and Gasenzer [4] in a path integral formalism, where the paths were restricted by a delta-function to the classical evolution. By comparing the quantum mechanical and classical time evolution of an initial density matrix they found good accordance in the limit of high occupation numbers $n(k)$.

3 Solitons

Solitons are non-dispersive wave solutions of a nonlinear system. They can be found in a wide range of physical situations, spanning from the earth's atmosphere [63], water surface waves [56] to optics [40]. Our main interest is the occurrence of solitons in a one-dimensional Bose gas, described by the nonlinear GPE. Depending on the interaction one distinguishes between bright (attractive interaction) and dark (repulsive interaction) solitons, which represent a localized rise or decrease of the density respectively. Since we investigate cold quantum gases of ^{87}Rb , with an s-wave scattering length of $a_s \approx 5.3\text{nm}$ and therefore repulsive interaction, we restrict our investigation to dark solitons. This chapter summarizes the basic properties regarding their analytical solution, interaction, and movement in a harmonically confined gas.

3.1 Solitonic solution

In general, a dark soliton is a stationary solution of the homogenous nonlinear Schrödinger equation, first described by Zakharov and Shabat [69]. This equation is equal in form to the GPE in absence of an external potential $V = 0$. For repulsive interactions the analytic solution of one solitonic excitation is

$$\phi_\nu^{(1)}(z, t) = \sqrt{n} \left[i\nu + \gamma^{-1} \tanh \left(\frac{z - (z^0 + \nu c_s t)}{\sqrt{2}\xi\gamma} \right) \right] e^{i\mu t} \quad (3.1)$$

where the parameters are given by

'Lorentz factor'	$\gamma^{-1} = \sqrt{1 - \nu^2}$
greyness	$\nu = \frac{v_s}{c_s}$
Bogoliubov speed of sound	$c_s = \sqrt{\frac{ng}{m}}$
healing length	$\xi = \frac{1}{\sqrt{mng}}$
homogenous background density	n
chemical potential	μ

(3.2)

The soliton represents a localized density minimum, with the maximum density depression $n_{\min}/n = \nu^2$, associated with a phase jump of $\Delta\theta \leq \pi$ and moves in the medium with constant velocity v_s . In the following, a soliton with $v_s = 0$ is called

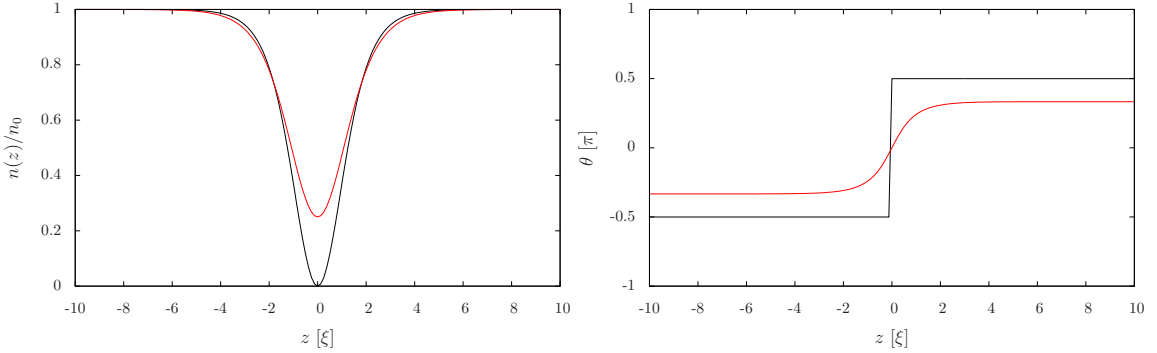


Figure 3.1: Density profile and phase of a single black (black curve) and grey (red curve) soliton.

black and a soliton with $v_s \neq 0$ is called grey. Fig. (3.1) shows the density profile and the phase of the Bose field for a black soliton (black curve) and a soliton of greyness $\nu = 0.5$ (red curve). We see that the width of the soliton is approximately given by ξ , whereas the width of the phase jump of a grey soliton is given by $\xi\gamma^{-1}$, which goes to infinity as $\nu \rightarrow 1$. More explicitly the phase change, as z varies from $-\infty$ to $+\infty$, is

$$\beta \equiv \Delta\theta = 2 \arccos(\nu) . \quad (3.3)$$

The energy E_s of a soliton, calculated by taking the difference between the grand canonical energies with and without a solitonic excitation, is

$$E_s = \frac{4}{3} \hbar c_s n (1 - \nu^2)^{-3/2} . \quad (3.4)$$

For small velocities the soliton behaves like a particle with mass $m = -4nc_s^{-1}$, which shows, in accordance to the density modulation, that the soliton is actually a hole excitation rather than a particle. Further we see that the energy decreases for higher velocities. This means that dissipative effects, *e.g.* collisions with thermal excitations, result in an acceleration of the soliton which disappears as $\nu \rightarrow 1$. This effect was calculated in [22] and is in a truly one dimensional system the cause for the decay of solitons. In higher dimensional systems, solitons are not stable and decay *e.g.* to vortex pairs or transversal excitations [21, 32]. This phenomenon is called the *snaking instability*. Finally, the physical momentum carried by the wave function due to the presence of the soliton can be calculated via the current $j(z)$, and is given by

$$p = m \int dz j(z) = -2\hbar n \nu \sqrt{1 - \nu^2} , \quad (3.5)$$

and has a maximum at $\nu \approx 0.7$.

Based on the work of Zakharov and Shabat [69], Blow and Doran [10] derived an

analytical solution for two solitonic excitations in a homogenous medium

$$\begin{aligned} \phi_{\nu_1, \nu_2}^{(2)}(z, t) = & \left[1 - \frac{2i}{\Gamma} \left\{ \frac{2}{\gamma_1 + \gamma_2} \left(\frac{1}{i\gamma_1 + \nu_1} + \frac{1}{i\gamma_2 + \nu_2} \right) \right. \right. \\ & + (i\gamma_1 - \nu_1) \left(\frac{1}{\gamma_1} + \frac{e^{2z\xi^{-1}\gamma_1}}{\epsilon_1} \right) + (i\gamma_2 - \nu_2) \left(\frac{1}{\gamma_2} + \frac{e^{2z\xi^{-1}\gamma_2}}{\epsilon_2} \right) \left. \right\} \right] e^{-2i\mu t}, \end{aligned} \quad (3.6)$$

with

$$\begin{aligned} \Gamma = & (\nu_1 - i\gamma_1)(\nu_2 - i\gamma_2) \left(\frac{e^{2z\xi^{-1}\gamma_1}}{\epsilon_1} + \frac{1}{\gamma_1} \right) \left(\frac{e^{2z\xi^{-1}\gamma_2}}{\epsilon_2} + \frac{1}{\gamma_2} \right) \\ & \frac{1}{(\gamma_1 + \gamma_2)^2} \left(\frac{1}{\nu_1 + i\gamma_1} + \frac{1}{\nu_2 + i\gamma_2} \right) \\ \epsilon_j = & e^{2\gamma_j(z_j^0\xi^{-1} + 2\nu_j c_s t)}. \end{aligned} \quad (3.7)$$

This equation allows for the calculation of the exact propagation of two dark solitons, including their collisions. In the following we are interested in highly excited states. Because of that we need a formula for an arbitrary number of solitons. Since there is neither a closed exact formula for N_s solitons nor an analytical solution for the harmonically confined gas, we use the ansatz

$$\psi(z) = \psi_0(z) \prod_{i=1}^{N_s} n^{-1/2} \phi_{\nu_i}^{(1)}(z - z_i), \quad (3.8)$$

for an ensemble of N_s uncorrelated and well separated solitons, from here on referred to as a dilute ensemble. This is valid, because a soliton at position z_i changes the wave function $\psi(z)$ for $|z - z_i| \gg \xi$ only by a constant phase factor $e^{i\beta_i}$. Note that due to the neglect of correlations this field does in general not represent a solution of the GPE in which the soliton remain non-dispersive. In local density approximation we can also use this ansatz for a harmonically confined gas. The diluteness criterion requires a minimum size of the system for a given number of solitons N_s . We consider well separated solitons in a way that both the density dips and the phase jumps of two different solitons are well separated on the average. The density dip has an approximate width of $\Delta z_{\text{dip}} \simeq 4\xi$ which is nearly independent of the greyness ν . Since the phase jump has a width $\Delta z_{\Delta\theta}^{(\nu)} \simeq 4\gamma_\nu \xi$ for finite ν and $\Delta z_{\Delta\theta}^{(0)} = 0$, we see that the diluteness criterion requires an approximate minimum box length of $L_{\min} = 4\gamma_\nu \xi N_s$. Since $\gamma_\nu \rightarrow \infty$ as $\nu \rightarrow 1$ we consider $0 \leq |\nu| < 1$, which is no restriction since a soliton in the limit $|\nu| = 1$ has completely vanished. Keep in mind that for simulations with randomly distributed solitons, without a numerical verification of a vanishing overlap, we need in general $L \gg L_{\min}$.

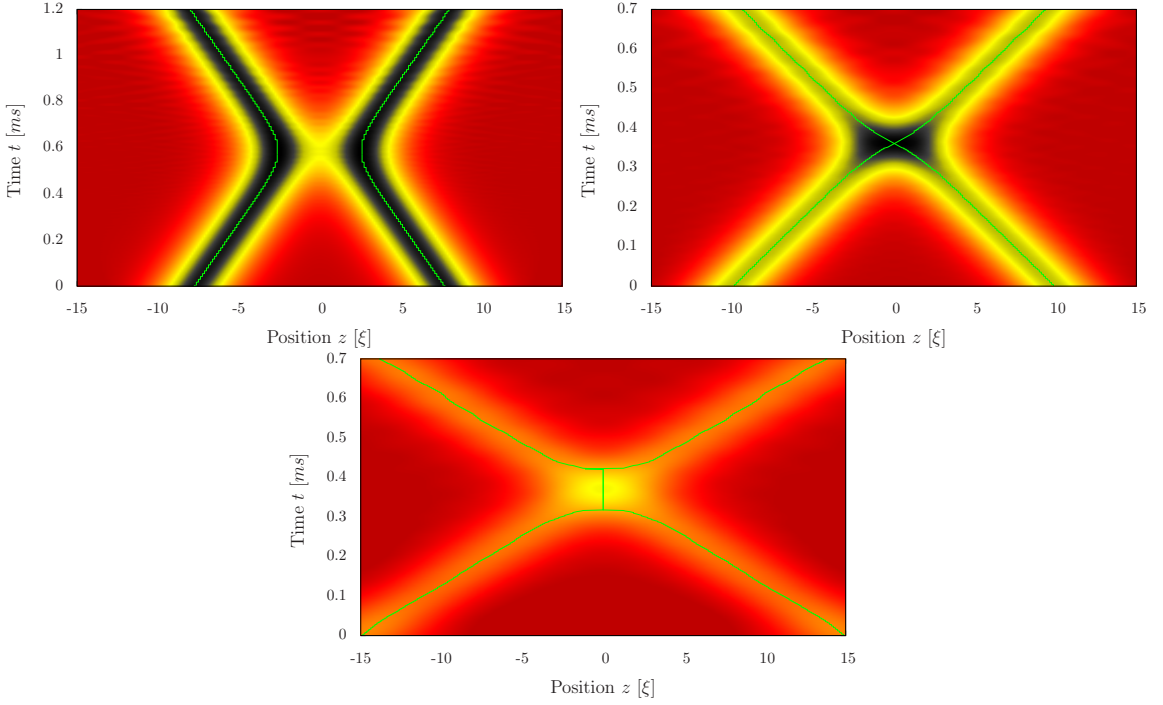


Figure 3.2: Symmetric scattering of two solitons with the density of the condensate displayed in colors. Left picture: $|\nu| = 0.3$, the solitons behave like classical particles and are always well separated; Right picture: $|\nu| = 0.5$, the solitons have the critical velocity and overlap completely for one moment; Lower picture: $|\nu| = 0.8$, the solitons stick together for a while. Note that for the last two pictures the solitons cannot be distinguished from each other after the collision.

3.2 Interaction of solitons

The simple ansatz (3.8) fails to analytically describe the interaction of solitons, as it is only valid in the limit where they are well separated. In order to get analytical predictions the exact Eq. (3.6) must be analyzed. For the case of a fixed absolute value of the greyness, it is possible to derive a formula for the minimum separation z_0 of the two solitons (see *e.g.* [66])

$$z_0 = \frac{1}{\sqrt{n(1 - \nu^2)}} \cosh^{-1}(\nu^{-1} - 2\nu)\xi . \quad (3.9)$$

This equation shows that we have a repulsive interaction between the solitons on a length scale on the order of the healing length. For velocities $\nu < 0.5$ the solitons have a minimal distance $z_0 > 0$ and are always well separated. Therefore each soliton continuously slows down and changes the sign of its velocity. At the point of closest approach we have $\nu = 0$ and the soliton is black. For the critical velocity $\nu = 0.5$ we get $z_0 = 0$. This means that the solitons overlap completely at the collision point and

cannot be distinguished from each other any more. Above the critical velocity the formula is not able to describe the scattering process. For higher velocities $\nu > 0.5$ the solitons even stick together for a while before separating again. The fact that we are not able to say if the solitons changed the sign of their velocity or just passed through each other implies that there is no point in time during the collision where the solitons turn black. The three different collision regimes are shown in Fig. (3.2). The solid lines show the trajectories of the density minimum at the center of the soliton. The huge difference in the scattering behavior above and below the critical velocity shows that we can distinguish between a particle like regime ($\nu < 0.5$) and a wave like regime ($\nu \geq 0.5$). Other possibilities to describe the scattering process are

- **Inverse scattering:** This method was used by Zakharov and Shabat [70] and is based on the inverse scattering transform. In this approach the exact two-soliton solution is regarded to separate in two single soliton solutions for asymptotic times $t \rightarrow \pm\infty$. They are assumed to preserve their velocity and only experience a phase shift, which corresponds to a spatial shift of the soliton. This method gives the correct asymptotic behavior for any velocity ν . However, due to the assumption of a preserved velocity, the dynamics close to the collision point cannot be described.
- **Effective potential:** Based on the analytic two-soliton solution Kivshar and Krolkowski [34] derived, an effective velocity dependent interaction potential by regarding the solitons as always well separated particles. Therefore the formula is a good approximation for solitons in the particle like regime. For two solitons with the same absolute value of the greyness the potential reads

$$V(z(t), \nu(t)) = \frac{\mu\gamma^2(t)}{2m \sinh^2[2\xi^{-1}\gamma(t)z(t)]} , \quad (3.10)$$

with $z = -z_1 = z_2$

The interaction is repulsive on length scales of the order of the healing length and becomes stronger as the soliton slows down. The advantage of the effective potential ansatz is, that it is not limited to truly one dimensional homogenous systems and can easily be generalized to multi-soliton collisions [66].

The approaches above are only valid in certain velocity or time regions and one has to evaluate which approach is best to describe the collision. Finally it is important to point out that the effect of a repulsive interaction is not only restricted to soliton-soliton collisions, but occurs in general with every defect or excitation in the gas. For example the acceleration of the soliton caused by interactions with phononic excitations, as mentioned above, or the interaction with a sharp edge of a confined condensate at very low temperatures. The second effect is confirmed in the next section, where we investigate the dynamics of solitons in harmonically confined gases.

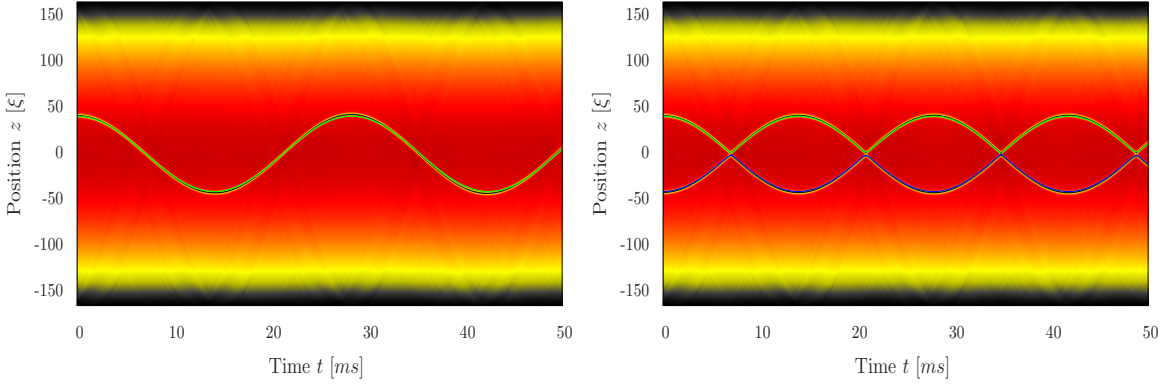


Figure 3.3: Oscillation of one (left picture) and two (right picture) solitons in real space. The density of the bose gas is displayed in colors. The solid lines show the predicted oscillation with $\omega_s = \omega_{\parallel}/\sqrt{2}$ with a deviation of 1.5% for the right picture caused by the collisions of the solitons.

3.3 Movement in traps

Many experiments, *e.g.* for an interaction quench [57], or the kind of experiment we will consider in Chapt. (5), work with a harmonically confined gas. For a sufficiently shallow harmonic potential, $l_{HO}/\xi \gg n_s^{-1}$, we can describe the Bose field in local density approximation. The dynamics of a soliton moving in a condensate in the TF-state was first described by Bush and Anglin [14] who showed that the soliton oscillates with the reduced frequency $\omega_s = \omega_{\parallel}/\sqrt{2}$, with the longitudinal trap frequency ω_{\parallel} . At the classical turning points the soliton momentarily turns black. The oscillation in real space of one and two solitons is shown in Fig. (3.3). The solid lines (green, blue) show the analytical harmonic oscillation. A single soliton oscillates with the predicted frequency ω_s , whereas for two solitons the frequency is 1.5% higher, which is caused by the collisions of the solitons. The movement of solitons can also be visualized in the dimensionless phase space $(z/z_c, \nu)$, where z_c is a characteristic length scale to describe the spatial extension of the condensate. For a Bose gas in the TF regime we have $z_c = R_{TF}$. Consequently z/R_{TF} and ν both range from -1 to 1 . In the particle like regime the trajectory of a single soliton is a circle in phase space with radius $\nu_{\max} = z_{\max}/R_{TF}$ which is traced out with constant angular velocity ω_s . The left picture of Fig. (3.4) shows the trajectory for a single soliton initially placed at $z/R_{TF} = 0.25$ (red) and $z/R_{TF} = 0.5$ (blue), with $\nu(t = 0) = 0$ in both cases. The picture in the middle shows the collision of two solitons (red and blue) in a harmonic trap initially placed asymmetrically at $2z_1/R_{TF} = -z_2/R_{TF} = 0.5$. As a consequence of the small velocities the solitons are always well separated and move in the subspaces $z/R_{TF} > 0$ and $z/R_{TF} < 0$. For higher velocities the dynamics differ from that of a classical particle. In the right picture of Fig. (3.4) the trajectory of a soliton initially placed at $z/R_{TF} = 0.75$ with $\nu(t = 0) = 0.8$ is displayed. We can see that the soliton moves nearly free in the region of high density and slows down very fast as it approaches the edges

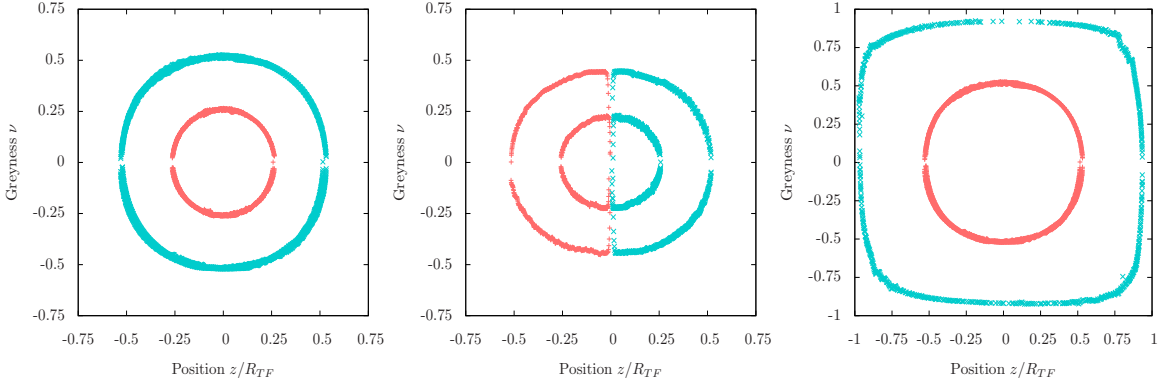


Figure 3.4: Soliton oscillations displayed in phase space $(z/R_{TF}, \nu)$. Left picture: One soliton for different initial position $(0.25, 0)$ (red curve) and $(0.5, 0)$ (blue curve); Middle picture: Two solitons initially asymmetric at $(0.25, 0)$ (red curve) and $(0.5, 0)$ (blue curve), due to the small velocities the solitons are distinguishable and move in the subspaces $z/R_{TF} \gtrless 0$; Right picture: One soliton for different initial positions $(0.5, 0)$ (red curve) and $(0.75, 0.8)$ (blue curve), note the deviation from the classical circular trajectory for the fast soliton.

of the gas, which shows the repulsive interaction between the edge and the soliton. In a Bose gas at finite temperature these fast solitons are less important for two reasons. Firstly the edges of the TF profile get smoothed, thereby diminishing the repulsive interaction, and secondly the fast solitons are likely to decay by being accelerated by phononic excitations above the Landau critical velocity c_s . Therefore considering solitons distributed inside a circle of radius 1 around the center of phase space, which corresponds to the dynamics of a classical particle of mass $2m$, is a good approximation for a stable soliton distribution. The scattering at the edges is important because it ensures the stability of solitons in the presence of *e.g.* a breathing excitation of the condensate. The trajectories get bent by the moving edge of the TF profile and therefore prevent the decay of the soliton caused by simply moving out of the region of non-vanishing density. Fig. (3.5) shows the time evolution of a condensate in a harmonic potential $\omega_{\parallel} = 2\pi 30$ Hz with one solitonic excitation, initially at $z/R_{TF} = 0.73$ with $\nu(t=0) = 0.8$, after the trap frequency was changed to $\omega_{\parallel} = 2\pi 55$ Hz at $t = 0$ to initiate the breathing excitation. For comparison the trajectory of the soliton without the breathing excitation is displayed (green line). One can clearly see how the trajectory is bent as the soliton approaches the edge. For highly excited states, see figure (3.6), the bending of trajectories, due to the breathing excitation, leads to an oscillating focusing (high density of solitons in at the center of the cloud) and defocusing (solitons oscillate with the cloud out to the maximum extent) of the solitons. This is caused by the different oscillation frequencies of the breathing excitation, with $\omega_b = \sqrt{3}\omega_{\parallel}$ for a true one-dimensional system [33], and the solitons $\omega_s = \omega_{\parallel}/\sqrt{2}$, whereby it is inevitable that fast solitons approach the edge of the cloud.

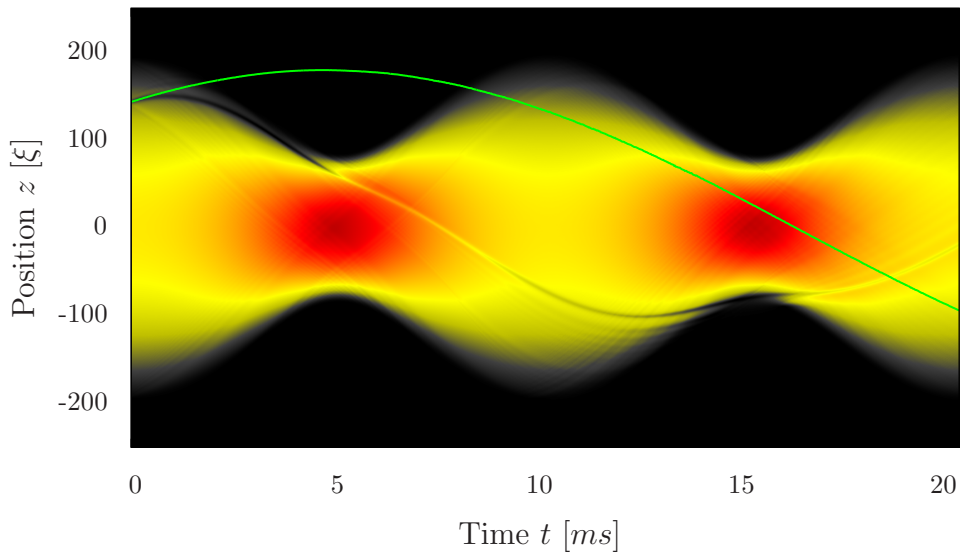


Figure 3.5: Condensate with a breathing excitation and one soliton initially at $(0.73, 0.8)$, with density encoded in colors. For comparison the trajectory of the soliton without the breathing (green line). The soliton remains stable because the trajectories bend and the soliton slows down as it approaches the edges of the TF profile.

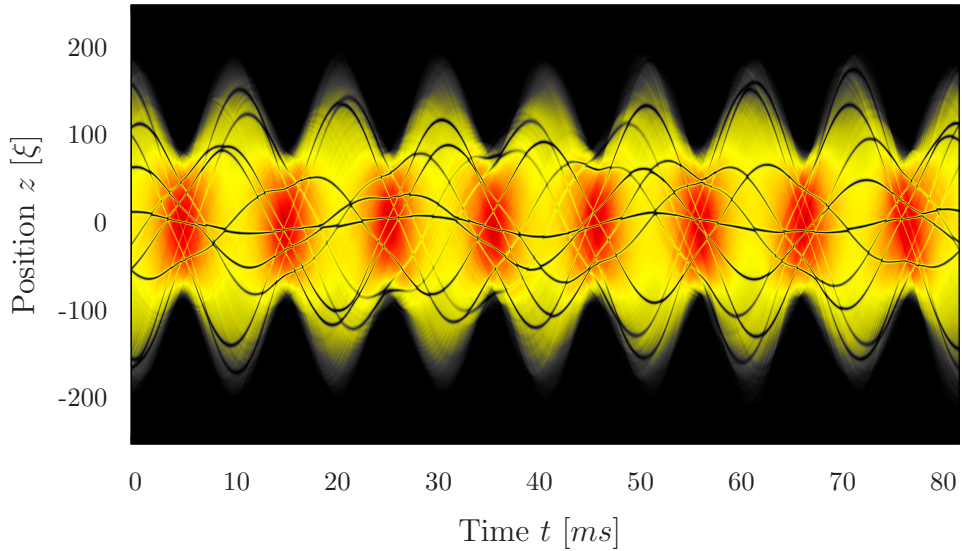


Figure 3.6: Condensate with a breathing excitation and $N_s = 10$ solitons. Note the focusing for $30\text{ms} \leq t \leq 40\text{ms}$ and the defocusing for $60\text{ms} \leq t \leq 70\text{ms}$.

4 Random soliton model

Motivated by the previously discovered connection between (quasi-) topological field configurations, strong wave turbulence and non-thermal fixed points we analyze in this chapter the influence of solitons on the momentum distribution of the gas. The results open a view on solitary wave dynamics from the point of view of critical phenomena far from thermal equilibrium. Due to the previously described properties of solitons (Chapt. (3)), namely the continuous connection to the ground state and the repulsive interaction on a short length scale, the solitonic state is well described by a random state in phase space. Therefore our main interest is to calculate the analytical spectrum for grey solitons. The results will then be compared to numerical results in several cases. In the last part we will look at how the finite size of the system affects a spectrum, and confirm the emergence of a double peak structure.

4.1 Analytic derivation of the spectrum

Here the goal is to derive an analytic formula for the spectrum $|\psi(k, t_0)|^2$ of the gas in the presence of solitons at a time t_0 . The time t_0 is considered arbitrary but fixed so we can drop all the time dependencies in this chapter. Based on the work of Rajantje and Tranberg [53], we derive an expression in the case of an inhomogeneous background density $n_0(z)$ perturbed by randomly distributed solitons of finite width and density n_s [57].

The consideration of only black solitons, would be a large restriction considering the fact that the solitonic excitation can be continuously deformed to the ground state. Because of this the emergence of only black solitons in an actual experiment is rather unlikely. We are further interested in the case of harmonically confined gases, where the velocity of a soliton is no longer preserved. Regarding this our goal is to derive an expression of the spectrum for an inhomogeneous background density $n_0(z) = |\psi_0(z)|^2$ perturbed by a dilute ensemble of solitons with density n_s , random position, and velocity.

First we calculate the spectrum for infinitely thin solitons by giving an expression for the first-order correlation function in real space $g^{(1)}(z_1, z_2)$ and calculating the Fourier transform $g^{(1)}(k, k')$. We consider a background wave function $\psi_0(z)$ which is disturbed by N_s solitons $\{z_i, \nu_i\}$ that are randomly positioned, in a poissonian way, and have a probability distribution $P(\nu)$ of the greyness. With the size of the system L the soliton density is given by $n_s = \frac{N_s}{L}$. Since for $|\bar{z}| = |z_1 - z_2| \gg \xi$ a soliton represents only a phase change of the wave function

$$\psi(z_2) = e^{i\beta\nu} \psi_0(z_1), \quad (4.1)$$

we can give an expression for $g^{(1)}(z_1, z_2)$. For one soliton, at random position z_i , the probabilities that the wave function has either experienced a phase jump, if $z_i \in (z_1, z_2)$, or not are

$$\begin{aligned}\mathbb{P}(z_i \notin (z_1, z_2)) &= 1 - |\bar{z}|L^{-1}, \\ \mathbb{P}(z_i \in (z_1, z_2)) &= |\bar{z}|L^{-1}.\end{aligned}\quad (4.2)$$

In order to get a closed formula for an arbitrary number of solitons we assume an averaged phase jump per soliton of $\langle e^{i\beta_\nu} \rangle_{P(\nu)}$. As we will see later, the derived formula is exact for a fixed absolute value of the greyness $|\nu| = \text{const.}$ and a good approximation for the general case. Hence we obtain

$$\begin{aligned}g^{(1)}(z_1, z_2) &= (1 - |\bar{z}|L^{-1})\psi_0(z_1)\psi_0(z_2) + |\bar{z}|L^{-1} \left[\int d\nu P(\nu) e^{i\beta_\nu} \right] \psi_0(z_1)\psi_0(z_2) \\ &= [1 - |\bar{z}|L^{-1}(1 - \int d\nu P(\nu) e^{i\beta_\nu})]\psi_0(z_1)\psi_0(z_2)\end{aligned}\quad (4.3)$$

For two solitons we can use the same arguments, thus receiving

$$\begin{aligned}\mathbb{P}(z_i \wedge z_j \notin (z_1, z_2)) &= (1 - |\bar{z}|L^{-1})^2 \\ \mathbb{P}(z_i \vee z_j \in (z_1, z_2)) &= 2|\bar{z}|L^{-1}(1 - |\bar{z}|L^{-1}) \\ \mathbb{P}(z_i \wedge z_j \in (z_1, z_2)) &= (|\bar{z}|L^{-1})^2 \\ \Rightarrow g^{(1)}(z_1, z_2) &= [1 - |\bar{z}|L^{-1}(1 - \int d\nu P(\nu) e^{i\beta_\nu})]^2 \psi_0(z_1)\psi_0(z_2).\end{aligned}\quad (4.4)$$

For N_s solitons we consequently arrive at

$$g^{(1)}(z_1, z_2) = [1 - |\bar{z}|L^{-1}(1 - \int d\nu P(\nu) e^{i\beta_\nu})]^{N_s} \psi_0(z_1)\psi_0(z_2). \quad (4.5)$$

If we take the limit of an infinitely large system $L \rightarrow \infty$, thereby keeping n_s fixed, we get

$$g^{(1)}(z_1, z_2) = e^{-2n_s \chi |\bar{z}|} \psi_0(z_1)\psi_0(z_2), \quad (4.6)$$

with χ being the average over $\chi_i = \frac{1}{2}(1 - e^{i\beta_{\nu_i}})$ given by

$$\chi = \frac{1}{2} \int d\nu P(\nu) [1 - e^{i\beta_\nu}] \quad (4.7)$$

We will see in section (4.3) that, due to the convergence of Eq. (4.5) to an exponential function, we can use Eq. (4.6) for a finite size system with a sufficiently large number of solitons N_s . The effects of a finite size system, which are most dominant for small N_s or non-uniform distributions, will be discussed in the last section (4.4) of this chapter. In the following we use $L \rightarrow \infty$, and therefore Eq. (4.6). To get the momentum distribution we calculate the Fourier transform of the correlator. We consider the case of an inhomogeneous background wave function and therefore

have to use the convolution theorem several times

$$\begin{aligned}\mathcal{FT}[(f * g)(x)] &= \hat{f}(k)\hat{g}(k) \\ \mathcal{FT}[f(x)g(x)] &= (\hat{f} * \hat{g})(k)\end{aligned}\tag{4.8}$$

$$\begin{aligned}g^{(1)}(k, k') &= \int \int dz_1 dz_2 e^{-ikz_1} e^{ik'z_2} g^{(1)}(z_1, z_2) \\ &= \int \int dz_1 dz_2 e^{-ikz_1} e^{ik'z_2} \psi_0(z_1) \psi_0(z_2) e^{-2n_s \chi |z_1 - z_2|} \\ &= \int dz_2 e^{ik'z_2} \psi_0(z_2) \int dz_1 \underbrace{\psi_0(z_1) e^{-ikz_1}}_{g_k(z_1)} \underbrace{e^{-2n_s \chi |z_1 - z_2|}}_{f(z_2 - z_1)} \\ &= \int dz_2 e^{ik'z_2} \psi_0(z_2) [g_k * f](z_2) \\ &= [\hat{\psi}_0 * \widehat{[g_k * f]}](k') .\end{aligned}\tag{4.9}$$

With the aid of the convolution theorem we can evaluate the above expression

$$\begin{aligned}\widehat{g_k * f}(k') &= \hat{g}_k(k') \hat{f}(k') \\ \hat{g}_k(k') &= \int dz e^{-ikz} \psi_0(z) e^{ik'z} = \int dz e^{-i(k-k')z} \psi_0(z) = \hat{\psi}_0^*(k - k')\end{aligned}\tag{4.10}$$

and get the final result for the correlator in momentum space

$$g^{(1)}(k, k') = [\hat{\psi}_0(k') * (\hat{\psi}_0^*(k - k') \hat{f}(k'))] ,\tag{4.11}$$

with $\hat{f}(k)$ being the Fourier transform of $f(|z_1 - z_2|)$

$$\hat{f}(k) = \frac{4n_s \operatorname{Re}(\chi)}{(2n_s \operatorname{Re}(\chi))^2 + (k - 2n_s \operatorname{Im}(\chi))^2} .\tag{4.12}$$

For a symmetric wave function we get for $k = k'$ the one-body momentum distribution

$$n(k) = n_0(k) * \hat{f}(k)\tag{4.13}$$

The next step towards a more realistic model is to consider the finite width of the solitons. For a dilute ensemble we can write the total wave function as (see Chapt. (3.1))

$$\psi(z) = \psi_0(z) \prod_{i=0}^{N_s} \phi_{\nu_i}(z - z_i) .\tag{4.14}$$

The derivative of this field gives

$$\psi'(z) = \psi'_0(z) \prod_i \phi_{\nu_i}(z - z_i) + \psi_0(z) \sum_i \phi'_{\nu_i}(z - z_i) \prod_{j \neq i} \phi_{\nu_j}(z - z_j) .\tag{4.15}$$

Since in the case of a dilute ensemble of solitons, for any i ,

$$\begin{aligned}\phi'_{\nu_i}(z - z_i) &\equiv \frac{d\phi_{\nu_i}(z - z_i)}{dz} \simeq 0 \quad \text{as} \quad |z - z_i| \gg \xi \\ \phi_{\nu_j}(z - z_j) &\simeq e^{i\beta_{\nu_j}\Theta(z_i - z_j)} \quad \text{as} \quad z_j \notin [z + z_i, z - z_i]\end{aligned}\quad (4.16)$$

Eq. (4.15) can in local density approximation be simplified to

$$\psi'(z) \simeq \left[\psi_0(z) \sum_i \delta(z - z_i) \prod_{j \neq i} e^{i\beta_{\nu_j}\Theta(z - z_j)} \right] * \phi'_{\nu_i}(z) . \quad (4.17)$$

The term in square brackets is proportional to the derivative of the field describing an ensemble of N_s infinitely thin solitons ($\xi \rightarrow 0$), at positions $\{z_i\}$,

$$\psi'(z) \simeq \left[\psi_0(z) \sum_i \frac{\gamma_i}{2} \psi'_{\xi \rightarrow 0}(z_i) \delta(z - z_i) \right] * \phi'_{\nu_i}(z) \quad (4.18)$$

Note that the derivative $\psi'_{\xi \rightarrow 0}(z_i)$ gives a sum of terms, each proportional to a delta distribution, but only one of these remains when evaluated at z_i , which gives the term in square brackets. Although one could now calculate the Fourier transform of $\langle \psi'(z_1)^* \psi'(z_2) \rangle$ we can simplify the calculation by noting that

$$\mathcal{FT}(\langle \psi'(z_1)^* \psi'(z_2) \rangle) \sim \left\langle \sum_{i,j} \frac{\gamma_i \gamma_j}{\sinh(\frac{\pi \xi k \gamma_i}{\sqrt{2}}) \sinh(\frac{\pi \xi k \gamma_j}{\sqrt{2}})} \right\rangle \sim \frac{\gamma^2}{\sinh^2(\frac{\pi \xi k \gamma}{\sqrt{2}})} , \quad (4.19)$$

where we have assumed for the second equality that the dependance of ν_i on $\gamma_i / \sinh(\frac{\pi \xi k \gamma_i}{\sqrt{2}})$ is negligible. Due to the fact that this assumption is inevitable in order to get to a closed formula we can rewrite Eq. (4.18) as

$$\psi'(z) \simeq \left[\frac{\gamma}{2} (\psi_0 \psi_{\xi \rightarrow 0})'(z) \right] * \phi'_{\nu}(z) , \quad (4.20)$$

which is in accordance with the earlier assumption of an averaged phase jump. With the aid of the convolution theorem we can now easily compute the Fourier transform

$$\begin{aligned}k\psi(k) &= k \int dz e^{ikz} \psi(z) = \int dz (-i \frac{d}{dz} e^{ikz}) \psi(z) = i \int dz e^{ikz} \psi'(z) \\ &= i \int dz e^{ikz} \left\{ \left[\frac{\gamma}{2} (\psi_0 \psi_{\xi \rightarrow 0})'(z) \right] * \phi'_{\nu}(z) \right\} = \frac{i\gamma}{2} \mathcal{FT}((\psi_0 \psi_{\xi \rightarrow 0})(z)) \mathcal{FT}(\phi'_{\nu}(z)) \\ &= \frac{k^2 \gamma}{2i} \mathcal{FT}((\psi_0 \psi_{\xi \rightarrow 0})(z)) \mathcal{FT}(\phi_{\nu}(z))\end{aligned}\quad (4.21)$$

$$\Rightarrow |\psi(k)|^2 = \frac{k^2 \gamma^2}{4} |(\psi_0 \psi_{\xi \rightarrow 0})(k)|^2 |\phi_{\nu}(k)|^2 . \quad (4.22)$$

This means that we can write the one-body momentum distribution for an ensemble of solitons with a finite width as the product of the one-body momentum distribution for an ensemble of infinitely thin solitons, given by Eq. (4.13), and the Fourier transform of the normalized analytic solution of a single soliton, given by

$$\phi_\nu(k) = i \left[2\pi\nu\delta(k) + \frac{\sqrt{2}\pi\xi}{\sinh(\frac{\pi\xi\gamma}{\sqrt{2}}k)} \right]. \quad (4.23)$$

If we put this together, we obtain the one-body momentum distribution in local density approximation for a dilute ensemble of N_s solitons, with greyness distributed according to the probability distribution $P(\nu)$ on an inhomogeneous background density $n_0(z)$:

$$n(k) = |\psi(k, t_0)|^2 = \left[n_0(k) * \frac{4n_s \operatorname{Re}(\chi)}{(2n_s \operatorname{Re}(\chi))^2 + (k - 2n_s \operatorname{Im}(\chi))^2} \right] \frac{\left(\frac{\pi\xi\gamma k}{\sqrt{2}}\right)^2}{\sinh^2(\frac{\pi\xi\gamma k}{\sqrt{2}})}, \quad (4.24)$$

with χ given by Eq. (4.7).

Before we compare the analytical result to grid simulations we first analyze the expected shape of the spectrum given by Eq. (4.24).

4.2 Scaling analysis

The maximum of the spectrum is at $k = 2n_s \operatorname{Im}(\chi)$ which is non-vanishing for $\operatorname{Im}(\chi) \neq 0$. This means that we have an overall flow in the system, reverse to the mean velocity of the solitons, due to the fact that a soliton represents a hole excitation. We can assume $\operatorname{Im}(\chi) = 0$ for solitons randomly distributed in phase space. For an inhomogeneous background density with a characteristic length scale σ the spectrum is governed by the following scales:

- $k \ll k_{n_s} = 2n_s \operatorname{Re}(\chi) < \sigma^{-1}$: The spectrum is given by the convolution of the background spectrum with a nearly constant value. Therefore the spectrum establishes a plateau.
- $\sigma^{-1} \ll k \ll k_{n_s}$: The spectrum is dominated by the shape of the background momentum distribution. The possibility of observing this regime depends on the particular background density.
- $k_{n_s} \ll k \ll k_{\text{kink}} = \frac{\sqrt{2}}{\pi\xi\gamma}$: The spectrum exhibits scaling behaviour $n(k) \sim k^{-2}$.
- $k_{\text{kink}} \ll k$: The finite width of the soliton solution causes a sharp decline.

4.3 Comparison with grid simulations

In this section, we analyze the derived momentum distribution Eq. (4.24) for different situations and compare the results with grid simulations on a lattice of G sites.

In order to judge the quality of our analytical spectrum $n_{\text{theo}}(k)$ we compute the reduced χ^2_{fit} of the fit, calculated using the well known formulae:

$$\begin{aligned} n(k) &= \langle |\psi(k)|^2 \rangle = \frac{1}{N_{\text{sim}}} \sum_i |\psi_i(k)|^2 \\ \Delta n(k) &= \sqrt{\frac{1}{N_{\text{sim}}(N_{\text{sim}} - 1)} \sum_i [|\psi_i(k)|^2 - n(k)]^2} \\ &= \sqrt{\frac{1}{N_{\text{sim}} - 1} [\langle (|\psi(k)|^2)^2 \rangle - n(k)^2]} \\ \chi^2_{\text{fit}} &= \frac{1}{f} \sum_k \left[\frac{n_{\text{theo}}(k) - n(k)}{\Delta n(k)} \right]^2, \end{aligned} \quad (4.25)$$

with the sum taken over the discrete lattice momenta and $f = G - g$ is the number of degrees of freedom, g being the number of fit parameters. The value $\sqrt{\chi^2_{\text{fit}}}$ can be interpreted as the mean deviation of the theoretical spectrum from the simulation in units of the standard deviation $\Delta n(k) \approx \mathcal{O}(10^{-20})$. Therefore a value $\sqrt{\chi^2_{\text{fit}}} \leq 3$ can be regarded as an excellent result.

4.3.1 Homogeneous background density

First, we consider the case of a homogeneous background density $n_0(z) = n_0$. Hence the local density approximation is exact and, considering $n_0(k) = n_0 \delta(k)$, we can write the analytical spectrum as

$$n(k) = \left[\frac{4n_0 n_s \operatorname{Re}(\chi)}{(2n_s \operatorname{Re}(\chi))^2 + (k - 2n_s \operatorname{Im}(\chi))^2} \right] \frac{\left(\frac{\pi \xi \gamma k}{\sqrt{2}} \right)^2}{\sinh^2\left(\frac{\pi \xi \gamma k}{\sqrt{2}} \right)} \quad (4.26)$$

with $\chi = \frac{1}{2} \int d\nu P(\nu) [1 - e^{i\beta_\nu}]$.

In the following we examine the spectrum for different distributions $P(\nu)$. Due to the fact that we calculate the spectra on a lattice with periodic boundary conditions, we choose ensembles of solitons such that there is no phase jump at the edges. For black solitons this means taking an even number of solitons whereas for grey solitons we restrict the ensemble to cases where the phase jump at the edges is a multiple of 2π . Keep in mind that this is only a limitation to the simulations and not of the analytic formula.

Constant absolute value of the greyness

First we consider the case of an absolute value of the greyness $|\nu| = |\nu_0|$. In this limit, the analytic formula Eq. (2.24) becomes exact, because the local density and averaged phase jump approximations are fulfilled, leading to $\beta_0 = 2 \arccos(\nu_0)$ and $\gamma_0^{-1} = \sqrt{1 - \nu_0^2}$.

The most general ensemble of solitons with fixed absolute value of the greyness is an ensemble of solitons moving with probability P in positive ($\nu = +\nu_0$) and with probability $Q = 1 - P$ in negative direction ($\nu = -\nu_0$). We can write the probability distribution $P(\nu)$ as

$$P(\nu) = P\delta(\nu - \nu_0) + Q\delta(\nu + \nu_0). \quad (4.27)$$

Consequently by inserting in Eq. (4.32) we get

$$\begin{aligned} \chi &= \frac{1}{2}(1 - \cos(|\beta_0|)) + \frac{i}{2}(1 - 2P)\sin(|\beta_0|) \\ n(k) &= \left[\frac{2n_0 n_s (1 - \cos(|\beta_0|))}{(n_s(1 - \cos(|\beta_0|)))^2 + (k - n_s(1 - 2P)\sin(|\beta_0|))^2} \right] \frac{\left(\frac{\pi\xi\gamma_0 k}{\sqrt{2}}\right)^2}{\sinh^2(\frac{\pi\xi\gamma_0 k}{\sqrt{2}})}. \end{aligned} \quad (4.28)$$

In the case of only black solitons ($\nu_0 = 0$) the above formula reduces to

$$n(k) = \left[\frac{4n_0 n_s}{(2n_s)^2 + k^2} \right] \frac{\left(\frac{\pi\xi k}{\sqrt{2}}\right)^2}{\sinh^2(\frac{\pi\xi k}{\sqrt{2}})}. \quad (4.29)$$

For infinitely thin solitons we get the corresponding formula by considering

$$\lim_{\xi \rightarrow 0} \left[\frac{\left(\frac{\pi\xi k}{\sqrt{2}}\right)^2}{\sinh^2(\frac{\pi\xi k}{\sqrt{2}})} \right] = 1. \quad (4.30)$$

We will now compare the analytical equations (4.28) - (4.29) to grid simulations on a lattice of size $G = 16384$.

Fig. (4.1) shows the results of the numerical ensemble average for black solitons with different values of the healing length ξ , for a fixed number of solitons $N_s = 2$ fixed. The solid lines correspond to the respective analytical spectra of Eq. (4.29), with the mean deviation from the computed spectra given in Tab. (4.1).

	$\xi = 0\mu m$	$\xi = 0.8\mu m$	$\xi = 1.6\mu m$
$\sqrt{\chi_{\text{fit}}^2}$	1.12	3.50	2.26

Table 4.1: Reduced chi-square values for respective fits in figure (4.1)

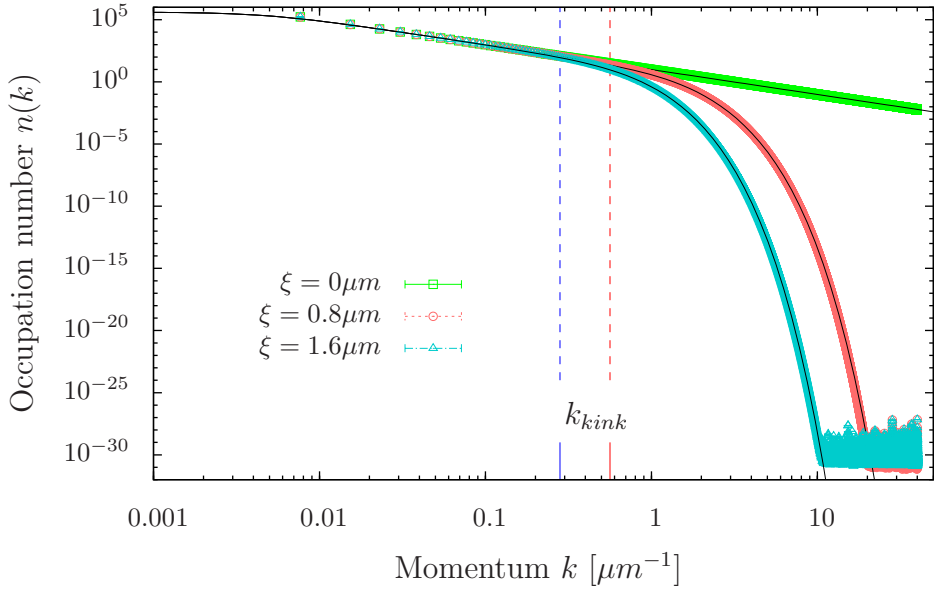


Figure 4.1: Momentum distributions for two randomly distributed solitons with healing length $\xi = 0$ (green curve), $\xi = 0.8\mu m$ (red curve), and $\xi = 1.6\mu m$ (blue curve). Vertical lines show the respective momenta k_{kink} above which the spectrum exhibits a sharp decline. For $\xi = 0$ (green curve) $k_{\text{kink}} \rightarrow \infty$ takes effect.

For $k \gg k_{\text{kink}} = \sqrt{2}(\pi\xi)^{-1}$ the spectrum exhibits the exponential decay due to the finite width of the solitons. The deviation at high momenta for $\xi = 0.8\mu m$ is an effect of the finite grid spacing, which is constant for all three cases. As a consequence the number of grid points, and hence the resolution, increases for larger healing lengths leading to better accordance, as can be seen by comparison with the curve for $\xi = 1.6\mu m$. For very small occupation numbers we see numerical noise caused by the limited machine precision of the double numbers. The $\sqrt{\chi^2_{\text{fit}}}$ parameters above are calculated for the momentum range in which we expect the simulations to be accurate. Because the shape of the spectrum for $\xi \neq 0$ at high momenta is, after a simple rescaling, independent of the healing length, we adopt the dimensionless variable $\tilde{k} = k\xi$, where $\tilde{k}_{\text{kink}} = \sqrt{2}(\pi\gamma)^{-1}$ and $\tilde{k}_{n_s} = 2\tilde{n}_s \text{Re}(\chi)$ with $\tilde{n}_s = n_s\xi$. Therefore we can keep the healing length fixed and vary only the soliton density. From here on we drop the tilde for the variable k .

The spectra for $N_s = 2, 20, 200$ solitons are displayed in Fig. (4.2). Solid lines represent the respective analytical results of Eq. (4.29) with a mean deviation given in Tab. (4.2).

The calculated spectra are in good accordance with the theoretical results, showing the expected scaling behavior $n(k) \sim k^{-2}$ in the regime $\tilde{k}_{n_s} \ll k \ll \tilde{k}_{\text{kink}}$ and the appearance of a plateau for $k \ll \tilde{k}_{n_s}$. For $N_s = 200$, there is a strong deviation from the predicted spectrum at high momenta, caused by the violation of the diluteness criterion given at the beginning of this chapter.

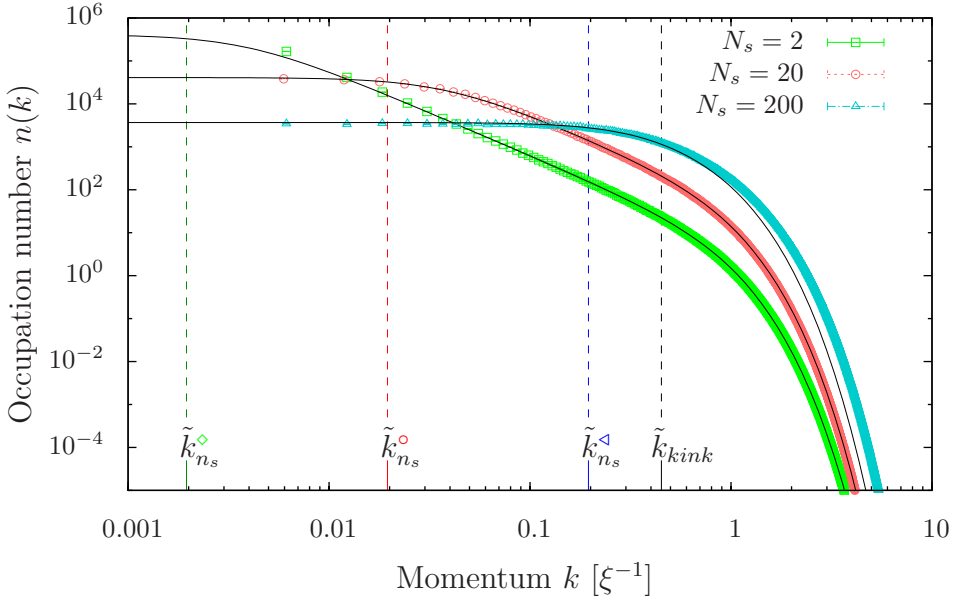


Figure 4.2: Momentum distributions for $N_s = 2$ (green curve), $N_s = 20$ (red curve), and $N_s = 200$ (blue curve) randomly distributed solitons with fixed healing length $\xi = 0.8\mu m$. Note the rescaled momentum variable.

	$N_s = 2$	$N_s = 20$	$N_s = 200$
$\sqrt{\chi_{\text{fit}}^2}$	2.12	2.34	44.81

Table 4.2: Reduced chi-square values for respective fits in figure (4.2)

Having seen the shape of the momentum distribution in the presence of black solitons, we now focus on the case of a non-vanishing greyness. First, we consider a fixed absolute value of the greyness $|\nu| = \nu_0$, for which we can use the exact formula (4.28). Figure (4.3) shows examples of the different soliton distributions. The upper left (right) picture shows the spectrum for $N_s = 20$ solitons with a constant positive greyness $\nu \simeq 0.3$ ($\nu \simeq 0.7$). The upper (lower) branch in each picture corresponds to the negative (positive) branch of the spectrum, and the inset figures show the spectrum on a linear scale. We can clearly see the peak of the momentum distribution at non-zero momentum and the gap between the branches increasing which coincides with the momentum carried by the soliton. Eq. (4.28) shows, that the position of the peak is proportional to $N_s p_s^\nu$, where p_s^ν is the momentum carried by a soliton of greyness ν , by noting that $n_s \text{Im}(\chi) \sim N_s(1-P)\nu\sqrt{1-\nu^2} \sim N_s(1-P)p_s$. The bottom right hand figure, which shows the mean momentum \bar{p} normalized to $N_s p_s^{\max}$, with p_s^{\max} being the maximum possible momentum carried by one soliton, for an ensemble of $N_s = 40$ solitons with fixed greyness confirms that also $\bar{p} = N_s p_s$. The bottom left hand figure shows the spectrum for $N_s = 12$ solitons with a fixed absolute value of the greyness $|\nu| \simeq 0.7$ moving with probability $P = 2/3$ in positive

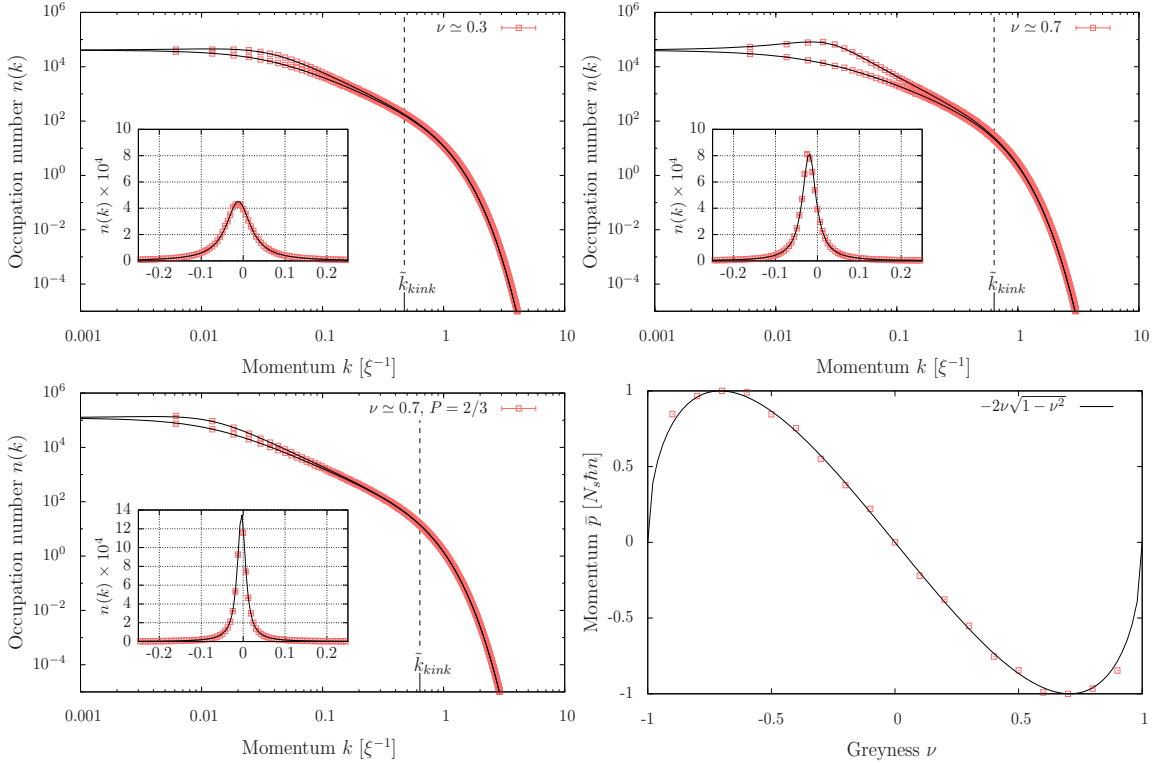


Figure 4.3: Momentum distributions for fixed absolute value of the greyness $|\nu| = \nu_0$ for N_s solitons moving with probability P in positive and $Q = 1 - P$ in negative direction. Solid black lines correspond to the analytical predictions of Eq. (4.28). Upper picture: $N_s = 20$, $P = 1$, $\nu_0 \simeq 0.3$ (left), $\nu_0 \simeq 0.7$ (right); Bottom left picture: $N_s = 12$, $P = 2/3$, $\nu \simeq 0.7$; Bottom right picture: Dependence of the mean momentum on the greyness of $N_s = 40$ solitons moving in one direction (red squares), solid black line is the analytical prediction of Eq. (3.5).

and $Q = 1/3$ in negative direction. Due to the imbalance of left and right moving solitons the system also has an overall flow, which vanishes for $P = Q = 1/2$. For completion we show the reduced chi-square parameter in Tab. (4.3).

Random greyness

Having seen the different effects of solitons on the spectrum in these idealized cases, we now turn to the more realistic case of an ensemble of solitons randomly distributed in phase space. Because we consider a flat distribution in phase space we can assume $\text{Im}(\chi) = 0$. Therefore the approximate expression for the spectrum takes the form:

$$n(k) = \left[\frac{4n_0 n_s \text{Re}(\chi)}{(2n_s \text{Re}(\chi))^2 + k^2} \right] \frac{\left(\frac{\pi \xi \gamma k}{\sqrt{2}} \right)^2}{\sinh^2 \left(\frac{\pi \xi \gamma k}{\sqrt{2}} \right)}, \quad (4.31)$$

	top left	top right	bottom left
$\sqrt{\chi_{\text{fit}}^2}$	2.48	2.45	2.21

Table 4.3: Reduced chi-square values for respective fits in figure (4.3)

with the yet to be determined parameters χ and γ . Fig. (4.4) shows the spectrum for an ensemble of $N_s = 20$ solitons randomly distributed in phase space (red squares). The solid line shows the analytical fit according to Eq. (4.31) with $\text{Re}(\chi) = 0.7$ and $\gamma = 1.05$. Compare this to the analytical average $\text{Re}(\chi) = 2/3$. The spectrum and analytical fits for $N_s = 20$ black (green triangles, dashed line) and $N_s = 20$ soliton with fixed greyness $\nu \simeq 0.7$ and $P = Q = 1/2$ (blue circles, dashed-dotted line) are plotted for comparison. Note the change of the scaling regime with γ . The reduced chi-square values are given in Tab. (4.4).

	random	black	$P = Q = 1/2$
$\sqrt{\chi_{\text{fit}}^2}$	2.73	2.33	2.28

Table 4.4: Reduced chi-square values for respective fits in figure (4.4)

4.3.2 Inhomogeneous background density

We now consider the case of an inhomogeneous background density $n(z)$. For the different cases regarded before we get the corresponding formulae simply by replacing the homogeneous background density n_0 with the convolution of the inhomogeneous momentum distribution $n_0(k)$:

$$n(k) = \left[n_0(k) * \frac{4n_s \text{Re}(\chi)}{(2n_s \text{Re}(\chi))^2 + (k - 2n_s \text{Im}(\chi))^2} \right] \frac{\left(\frac{\pi \xi \gamma k}{\sqrt{2}} \right)^2}{\sinh^2\left(\frac{\pi \xi \gamma k}{\sqrt{2}} \right)} \quad (4.32)$$

$$\text{with } \chi = \frac{1}{2} \int d\nu P(\nu) [1 - e^{i\beta_\nu}]$$

As discussed in section (4.1) the applicability of Eq. (4.32) to a finite system requires sufficiently large soliton numbers N_s . This ensures the convergence of the exact formula (4.5) to an exponential function (4.6). The advantage of this approximation is that we have a closed formula, and are therefore able to easily analyze the spectrum as a function of the soliton density n_s . Since the overall shape of the momentum distribution in the homogeneous case remain valid in the presence of an inhomogeneous bulk density, we restrict the presented analysis here to the

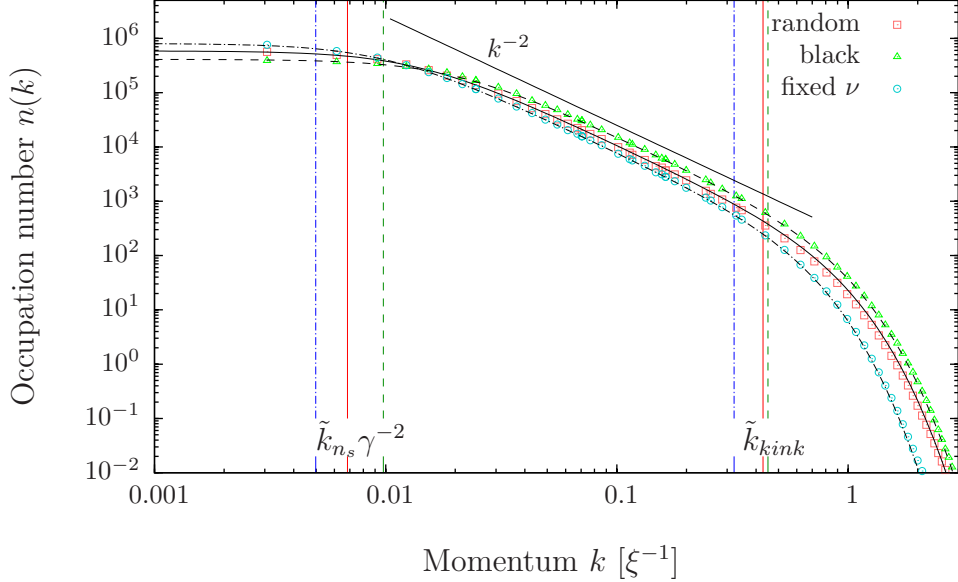


Figure 4.4: Momentum distribution for solitons randomly distributed in phase space (red squares). For comparison we show the spectra for randomly distributed black solitons (green triangles) and solitons with a fixed absolute value of the greyness $|\nu| \simeq 0.7$ choosing an equal number of right and left movers (blue circles). Black lines correspond to the analytical curves from Eq. (4.31) with $\text{Re}(\chi) = 0.7$ and $\gamma = 1.05$ as fit parameters for the case of random greyness. Between the horizontal lines we see the expected scaling behavior.

most realistic case for an actual experiment, namely an ensemble of solitons randomly distributed inside a circle with radius one around the center of phase space. We consider a Bose gas in the Thomas-Fermi regime, with the background density given by $n_0(z) = n_0(1 - (z/R_{TF})^2)$. The result for the numerical ensemble average for $N_s = 20$ solitons is shown in Fig. (4.5) (red squares). The solid line corresponds to the analytical formula with $\text{Re}(\chi) = 0.78$, $\text{Im}(\chi) = 0$ and $\gamma = 1.1$, which, because of the convolution, has to be calculated numerically. For comparison we plotted the spectrum for the same number of black solitons randomly distributed across the trap (blue circles and dashed-dotted line). The corresponding chi-square values are given in table (4.5).

	random	black
$\sqrt{\chi_{\text{fit}}^2}$	2.43	2.17

Table 4.5: Reduced chi-square values for respective fits in Fig. (4.4)

We can see that the analytical formula agrees very well with numerical simulations

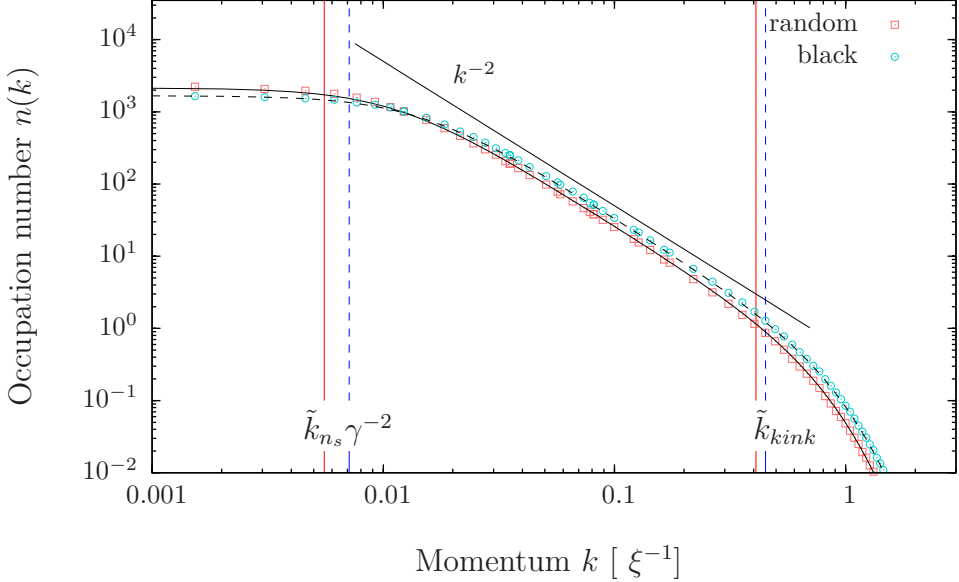


Figure 4.5: Momentum distribution for $N_s = 20$ solitons on a TF background density randomly distributed in phase space (red squares). The solid black line is the analytical prediction with $\text{Re}(\chi) = 0.78$, $\text{Im}(\chi) = 0$ and $\gamma = 1.1$. For comparison the spectrum of randomly distributed black solitons (blue circles) and the analytical prediction (black dashed line).

in all considered cases, which justifies the approximations done to derive a closed formula for the spectrum. Due to the fact that we do not have any restrictions on the greyness or the particular shape of the background density, the formula can be applied by experimentalists to verify the presence of solitons via the measurement of the momentum distribution. This presents us with a great opportunity especially for experiments in which the resolution is not good enough to see the solitons directly in the density images.

4.4 Double peak structure of the spectrum

So far we have only considered the case of a sufficiently high number of solitons randomly distributed flat across the whole phase space. However, as we saw in Sect. (4.1), the behavior of the first-order coherence function in the case of a finite size system changes drastically for small soliton numbers. In the limit of an infinite system ($L \rightarrow \infty$) these changes do not occur, since either $n_s \rightarrow 0$ if $N_s = \text{const.}$ or $N_s \rightarrow \infty$ if $n_s = \text{const.}$. Therefore the first-order coherence function always exhibits an exponential decay. We now analyze a trapped condensate with a small number of solitons, and see a surprising effect, namely a double peak structure in the spectrum. Because this structure appears in trapped systems, it is also relevant for cold atom experiments.

The emergence of a double peak structure for a harmonically confined, finite size

system can be seen by considering the case of one soliton at an arbitrary fixed position z_0 . We can write the wave function in local density approximation as

$$\psi_{\nu,\gamma,\xi}(z) = \psi_0(z)\phi_{\nu,\gamma,\xi}(z - z_0), \quad (4.33)$$

with the wave function of the undisturbed background $\psi_0(z)$ and the single soliton solution $\phi_{\nu,\gamma,\xi}$ of a soliton with greyness ν and healing length ξ . For a symmetric background, with a finite width $2R$, and one black soliton at the center of the trap ($z_0 = 0$), the wave function above changes its sign and is, independent of ξ , an odd function of z therefore leading to $n(k = 0) = 0$, which indicates the possible emergence of a double peak structure of the spectrum. For $z_0 \rightarrow R$ the wave function becomes more and more symmetric, which leads to a steady rise of the zero mode $n(k = 0)$ to its undisturbed value. Concurrently the maxima of the spectrum at non-zero k have to decrease. In the case of a grey soliton the spectrum is asymmetric due to the momentum carried by the soliton. The occupancy number of zero mode is given by $n(k = 0) = \nu^2 n_0(k)$. The picture at the upper left corner of Fig. (4.6) shows the spectra of a TF bulk density with one soliton at the center of the trap for two different values of the greyness. For an ensemble of N_s randomly distributed solitons the analytical predictions derived in the previous sections are, in the short wavelength limit, in good agreement with the numerical simulations. The assumption of an exponential decay of the first order correlation function in a finite size system enabled us to derive a closed formula of the spectrum for an arbitrary number of solitons. But this assumption is not justified in the long wavelength limit or for small N_s , and the exact formula

$$g^{(1)}(z_1, z_2) = [1 - |\bar{z}|L^{-1}(1 - \int d\nu P(\nu)e^{i\beta_\nu})]^{N_s} \psi_0(z_1)\psi_0(z_2) \quad (4.34)$$

must be used instead. This is best seen by taking a look at the normalized first-order coherence function $\tilde{g}_1(z, z') = g_1(z, z')/\sqrt{n(z)n(z')}$. In the upper right picture of Fig. (4.6) we show $\tilde{g}_1(0, z)$ for different numbers N_s of black solitons randomly distributed across a TF bulk density. The solid lines correspond to the exact analytic Eq. (4.34) whereas the dashed lines are the approximated predictions of an exponential decay (4.6). This illustrates the huge difference for small soliton numbers, caused by the finite size of the system and therefore the certainty of finding the soliton in a finite region. It also shows good accordance for $N_s \gtrsim 10$, where the approximation becomes valid, and the analytical and numerical spectra coincide for $|k| \gtrsim 0$. This discrepancy demonstrates that, in order to obtain the spectrum for small soliton numbers, we have to analyze the exact equation. However, two problems occur. Firstly we cannot give a closed formula of the Fourier transform of $\tilde{g}_1(z, z')$ given by Eq. (4.34) and secondly, due to the finite size, the variables z, z' are no longer independent and we cannot use the convolution theorem (4.10). Therefore the momentum distribution for a given number of infinitely thin solitons has to be computed numerically via the Fourier transform of Eq. (4.34). In the case of a finite width the corresponding formula are again given by Eq. (4.22). In the lower left pic-

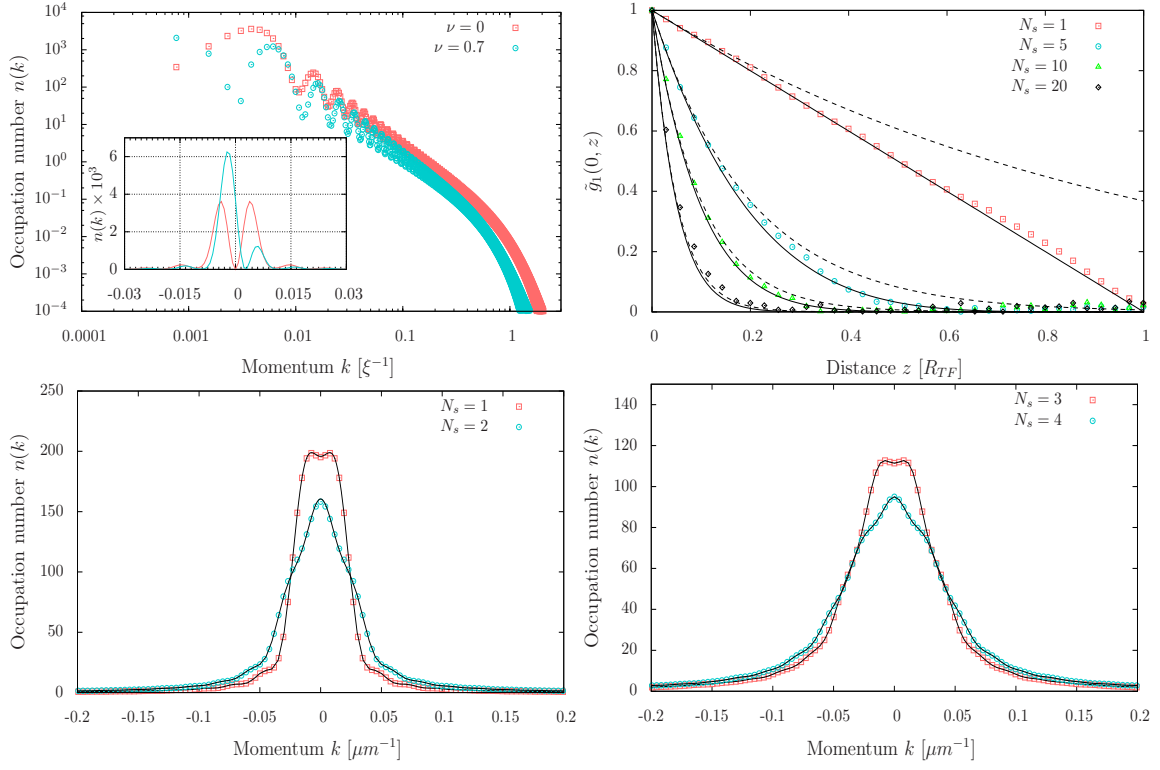


Figure 4.6: Upper left picture: Momentum distribution for one soliton at the center of the trap with $\nu = 0$ (red squares) and $\nu = 0.5$ (blue circles); Upper right picture: Normalized first order coherence function for an ensemble of 5000 configurations of N_s black solitons randomly distributed across the whole condensate (colored points). Black lines show the respective analytical predictions of eq. (4.34) (solid) and eq. (4.6) (dashed). Lower pictures left (right): momentum distribution for an ensemble of $N_s = 1, 2$ ($N_s = 3, 4$) black solitons distributed over the whole condensate. Colored points: results of the numerical ensemble average, solid lines: analytical predictions of eq. (4.34)

ture of Fig. (4.6) the spectra for an ensemble of 5000 configurations with one (red squares) and two (blue circles) infinitely thin black solitons distributed flat across the whole TF condensate are displayed. The solid lines correspond to the analytical predictions of the momentum distribution according to Eq. (4.34). The lower right picture shows the respective curves for three and four solitons. In all cases very good agreement can be seen. Comparing the spectra for one and three solitons we see that the double peak structure becomes less pronounced for a higher soliton number. This coincides with the convergence of \tilde{g}_1 to an exponential function, for which the analytical spectrum is always peaked around zero. The differences of the momentum distribution for odd or even numbers of solitons will be discussed later on. We would like to point out, that although Eq. (4.34) gives the exact spectrum for an arbitrary number of solitons with random greyness, distributed flat across the whole

condensate, for a sufficiently high number of solitons it is more practical to use the approximate Eq. (4.32) as it allows an easy analysis of the shape of the momentum distribution dependent on the characteristic soliton parameters $\{n_s, \nu, \xi\}$.

Double peak for a single non-uniform distributed soliton

It is obvious from Eq. (4.34) that the double peak structure has to vanish for higher velocities, because the spectrum is continuously deformed into its unperturbed ground state as $|\nu| \rightarrow 1$. This behavior is generic for any ensemble of solitons distributed according to a distribution $P(z, \nu)$, and we can predict limitations for the occurrence of the multipeak structure by solving the corresponding problem for one black soliton. The doublepeak structure vanishes above a critical velocity $\nu_{crit} = \nu_{crit}(P(z))$. Therefore we insert the single soliton solution $\phi_{\nu, \gamma, \xi}$ and write Eq (4.33) as:

$$\begin{aligned}\psi_{\nu, \gamma, \xi}(z) &= \psi_0(z) \left[\sqrt{1 - \nu^2} \tanh \left(\frac{z - z_0}{\gamma \xi \sqrt{2}} \right) + i\nu \right] \\ &= \sqrt{1 - \nu^2} \psi_{\nu=0, \xi(\nu)}(z - z_0) + i\nu \psi_0(z),\end{aligned}\quad (4.35)$$

where $\psi_{\nu=0, \xi(\nu)}(z - z_0)$ is the wavfunction for a black soliton with the healing length $\xi(\nu) = \xi\gamma$ on the background ψ_0 . With this we can write the one body density matrix for N_i realizations for solitons $\{z_i, \nu_i\}$ distributed according to the probability distribution $P(z, \nu)$ as:

$$\begin{aligned}n_{\nu, \gamma, \xi}(z, z') &= \frac{1}{N_i^2} \sum_{\{z_i, \nu_i\}, \{z_j, \nu_j\}} \sqrt{(1 - \nu_i^2)} \sqrt{(1 - \nu_j^2)} \psi_{\nu=0, \xi(\nu)}(z - z_i) \psi_{\nu=0, \xi(\nu)}^*(z' - z_j) \\ &\quad + \nu_i \nu_j \psi_0(z) \psi_0^*(z') \\ &\quad - i\sqrt{1 - \nu_i^2} \nu_j \psi_{\nu=0, \xi(\nu)}(z - z_i) \psi_0^*(z') \\ &\quad + i\sqrt{1 - \nu_j^2} \nu_i \psi_{\nu=0, \xi(\nu)}^*(z' - z_j) \psi_0(z).\end{aligned}\quad (4.36)$$

The last two terms on the right hand side are responsible for the asymmetry of the spectrum in case of an overall flow of the system. By assuming a vanishing flow in average these terms become negligible. If we further assume an averaged phase jump per soliton, which is again exact for a fixed absolute value of the greyness, we can easily compute the Fourier transform and get the spectrum

$$n_{\nu, \gamma, \xi}(k) = (1 - \nu^2) n_{\nu=0, \xi(\nu)}^{(1)}(k) + \nu^2 n_0(k)\quad (4.37)$$

with $n_{\nu=0, \xi(\nu)}^{(1)}(k)$ being the one body momentum distribution for one black soliton distributed according to $P(z, \nu = 0)$ with the healing length $\xi(\nu) = \xi\gamma$. Since we are at this point mostly interested in the spectrum for small values of k we can

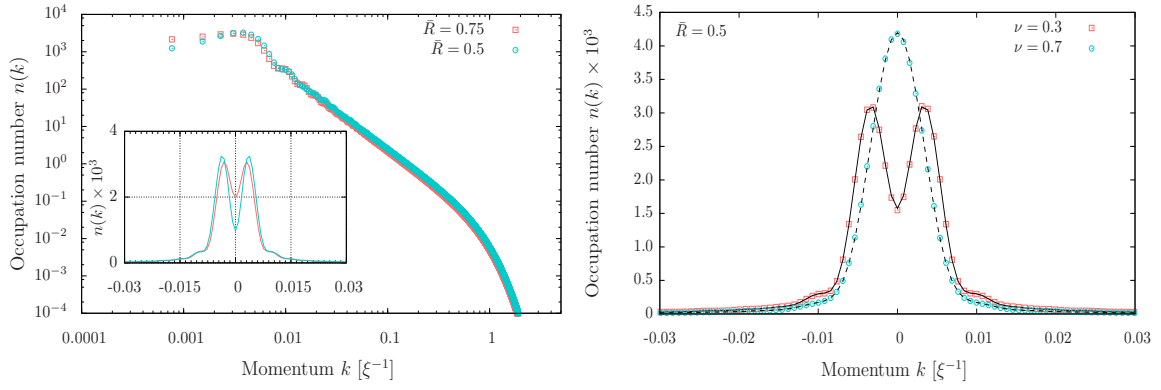


Figure 4.7: Momentum distributions for one soliton on an inhomogeneous TF background. Left picture: Ensemble average of one black soliton randomly distributed across a fraction $\bar{R} = 0.75$ (red squares), $\bar{R} = 0.5$ (blue circles) around the center of the trap; Right picture: Ensemble average of one grey soliton, $\nu = 0.3 < \nu_{\text{crit}}$ (red squares) and $\nu = 0.7 > \nu_{\text{crit}}$ (blue circles), randomly distributed across the fraction $\bar{R} = 0.5$ of the TF background. The solid lines correspond to the analytical curves of Eq. (4.37).

set $\xi(\nu) = \xi$, keeping in mind that Eq. (4.37) is only valid for $k \ll k_{\text{kink}}$. This equation allows us to determine the whole spectrum for any value of the greyness, by a deformation of the corresponding problem for one black solitons distributed according to $P(z, 0)$, and particularly the velocity dependence of the low momentum modes. This defines the critical velocity ν_{crit} above which the zero mode ($n(k = 0)$) has the highest occupation number. Since the Fourier transform of the normalized first order coherence function for N_s solitons can be written as N_s convolutions of the \tilde{g}_1 for one soliton, ν_{crit} sets an upper boundary for the mean velocity above which the multipeak structure vanishes for any N_s . For more than one soliton the above calculation can also be done, but does not lead to such a simple formula, because the final expression involves the fields explicitly.

We take as an example the non-uniform soliton distribution to be flat across a fraction $\bar{R} = z_{\text{max}}/R_{\text{TF}} < 1$ of the condensate. The spectra for two different values of \bar{R} are shown in the left picture of Fig (4.7). The occupation number of the zero mode decreases with \bar{R} and becomes zero for $\bar{R} \rightarrow 0$. By using the respective spectrum as $n_{\nu=0,\xi}^{(1)}(k)$ we can calculate the spectra for an arbitrary value of the greyness. In the right picture, we show the results of the numerical ensemble average for a fixed absolute value of the greyness (red and blue points) and the spectrum we expect from Eq. (4.37) (solid lines). There is perfect agreement for $k \ll k_{\text{kink}}$. The spectrum changes its shape from a double to a single peak structure depending on the greyness of the soliton. In the upper two pictures of Fig. (4.8) the occupation number of the first eight grid momentum modes, calculated using Eq. (4.37), are plotted as a function of the greyness. For small values of the greyness we see that the zero mode n_0 lies below the higher modes $n_{k_i \neq 0}$, which is the regime of the double

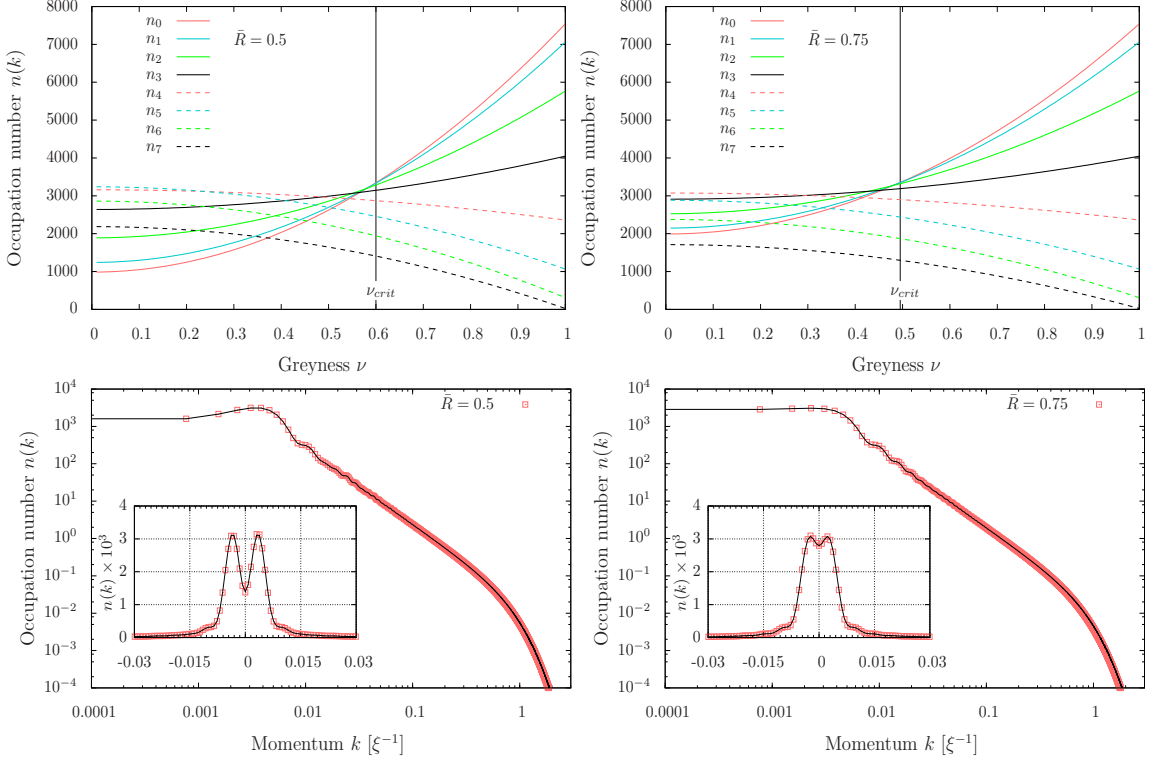


Figure 4.8: Upper row: Occupation number of the first 8 grid-momentum modes as a function of ν for $\bar{R} = 0.5$ (left) and $\bar{R} = 0.75$ (right) given by (4.37). The critical velocity ν_{crit} is marked by the vertical line; Lower row: Ensemble average momentum distribution of one soliton randomly distributed in a circle of radius $\bar{R} = 0.5$ (left), $\bar{R} = 0.75$ (right) around the center of phase space. The solid lines are the analytical curves of Eq. (4.37) with $\nu = 0.3$ (left), $\nu = 0.38$ (right).

peak structure, whereas for $\nu \rightarrow 1$ the occupation numbers, independently of \bar{R} , take the undisturbed values $n_0(k)$ of the Thomas Fermi background. The vertical line shows the critical soliton velocity $\nu_{crit}(\bar{R})$ above which the double peak structure vanishes. The lower pictures in Fig (4.8) display the spectra for an ensemble of one solitons randomly distributed in a circle with radius $\bar{R} < 1$ around the center of phase space (squares) and the respective curves given by Eq. (4.37) with ν as a free parameter, which is fixed by the occupation number of *e.g.* the zero mode. For the left (right) picture with $\bar{R} = 0.5$ ($\bar{R} = 0.75$) we find $\nu \simeq 0.30$ ($\nu \simeq 0.38$) and see again very good agreement with the analytical predictions. The double peak structure for $\bar{R} = 0.75$ has nearly vanished, caused by the rise of the mean velocity of the ensemble and the simultaneous decrease of the critical velocity with \bar{R} , which coincides with a decrease of the density near the center of phase space. This shows that the double peak becomes more pronounced for any distribution $P(z, \nu)$ with a higher probability of finding solitons near the center of phase space. Finally we take a look at the momentum distribution for two solitons distributed randomly inside

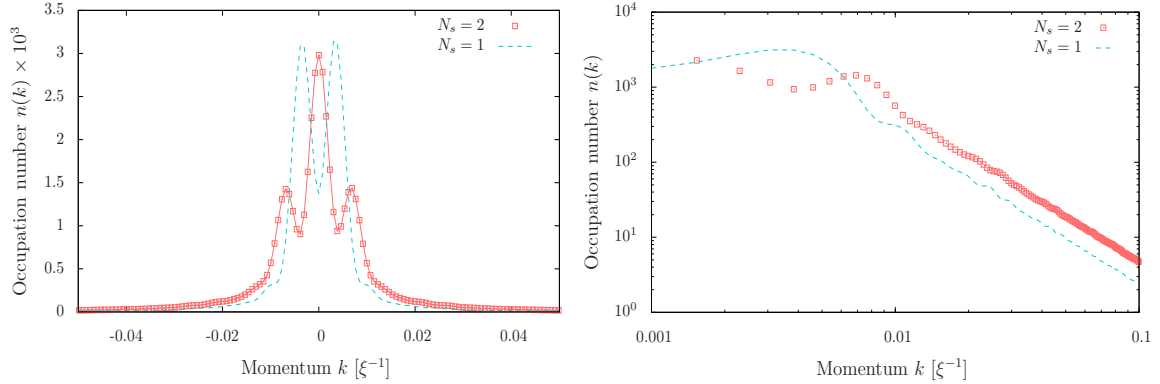


Figure 4.9: Triple peak structure of the spectrum on a linear (left picture) and double-logarithmic (right picture) scale for an ensemble of $N_s = 2$ solitons distributed flat inside a circle of radius $\bar{R} = 0.5$ around the center of phase space (red squares). For comparison the results for the numerical ensemble average for one soliton (blue dashed lines).

a circle of radius $\bar{R} = 0.5$ around the center of phase space (Fig. (4.9)). We can see that the spectrum has a triple peak structure, caused by the very pronounced double peak for one soliton (blue dashed lines), due to the high density near the center of phase space. Therefore we can distinguish between an odd (double peak structure) and even (triple peak structure) number of solitons. By comparison to the case $\bar{R} = 1$ we see that the critical velocity for the emergence of the triple peak structure lies below that of the double peak, and hence we have only a single peak. For higher soliton numbers additional peaks arise in the spectrum. However, as they diminish in height, the determination of the soliton number by counting the peaks in the spectrum is only possible for $N_s \leq 5$. Finally, it is important to keep in mind, that this behaviour is not only restricted to the TF regime, but occurs in every finite size system, because the emergence of the multi-peak structure is simply related to the certainty of finding a soliton in a finite region of space.

In this chapter we derived an analytical formula for the momentum distribution of a condensate in the presence of solitonic excitations. The emergence of a power-law behavior in a range of momenta between the inverse of the inter-soliton distance and the inverse healing length suggests the connection between a non-thermal fixed point and solitonic excitations. In this momentum range the system appears self-similar. This confirms our interpretation of the solitonic state in terms of turbulence. Furthermore we derived a formula in case of a trapped condensate, which is of great relevance for experimental observations. The spectrum shows a multi peak structure for low momenta and also the transient power-law behavior described above. The emergence of these finite size effects was connected to the mean velocity of the soliton ensemble.

5 Experimental characterization of solitonic states

In this chapter we analyze the impacts of solitons in a realistic experimental setting. The work was inspired by the appearance of a strong double peak structure in the expanded density, during an experiment recently done in Vienna in the group of Prof. Schmiedmayer [58, 13]. The common way to measure the momentum distribution is through a free expansion of the cloud. This technique will be explained in the second section of this chapter (5.2). In order to make the numerical and experimental results easier to compare the free expansion of the cloud was also simulated. In this thesis we focuss on the possibilities to characterize the solitonic state. However, since this part of the thesis was highly influenced by the experiment done in Vienna, we refer at some points to the experimental observations, in order to illustrate their accordance with the numerical results.

5.1 Experimental setup and initial state

The experiment takes place on an atom chip with a highly anisotropic trapping potential [24, 23, 59]. The trap frequencies are $\omega_{\perp} = 3.3\text{kHz}$ for the transversal confinement and $\omega_{\parallel} = \omega = 23\text{Hz}$ in the longitudinal direction. The initial sample contains $N \approx 55000$ atoms at a temperature $T \approx 800\text{nK}$, and is therefore above the critical temperature of a quasi one-dimensional condensate. A quench is performed by linearly ramping down the transversal confinement with a rate R_Q , thereby quickly removing the transversely excited states. After the quench the transversal potential is put back to its original value, leaving a quasi one-dimensional condensate, occupying only the transversal ground state. Due to the fast removal of atoms the cloud starts to collapse, leading to the observed quadrupole oscillation with $\omega_b \approx 1.6\omega$. During this quench the system undergoes a crossover to the BEC regime. The crossing rate is proportional to the inverse quench rate R_Q^{-1} . Therefore defects are produced in accordance with the Kibble-Zurek mechanism. After the quench, the system is allowed to evolve until measurements are done at different hold times t_{hold} . The in Situ density is measured in absorption after a short time of free expansion τ , for which all trapping potentials are turned off. An expansion time of $\tau = 46\text{ms}$ makes the momentum space accessible via a density measurement in fluorescence. This technique will be explained in the next section (Sect. (5.2)). Note that due to the finite resolution of the density measurements ($4\mu\text{m}$), in comparison to the healing length $\xi \approx 0.33\mu\text{m}$ of the system, it is difficult to observe the solitons in Situ. A typical image of the in Situ density for one realization, obtained from our simulations, is displayed in Fig. (5.1). The upper picture shows the density of a

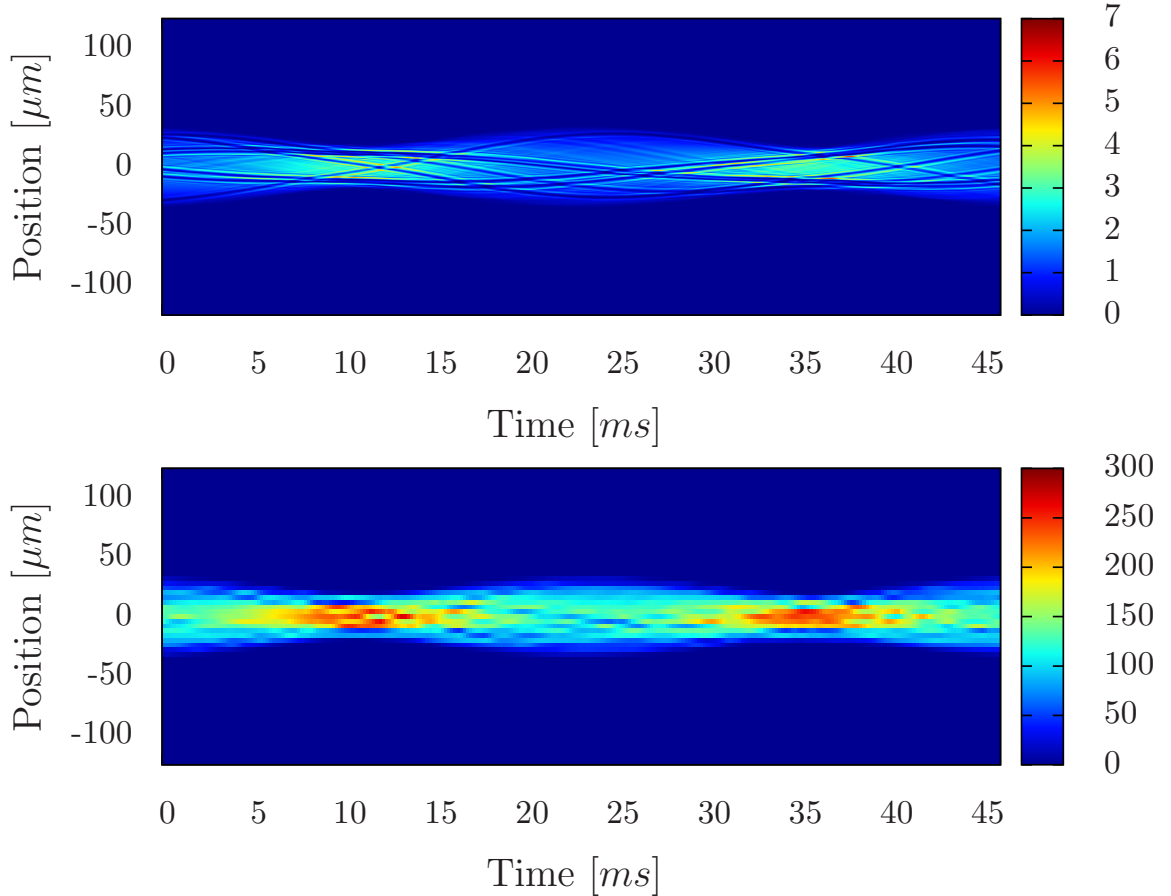


Figure 5.1: Density for one realization after $\tau = 1.5\text{ms}$ of free expansion. Upper picture: Resolution of the numerical simulations $\Delta z = a_G = 0.05\mu\text{m}$; Lower picture: Resolution of the experiment $\Delta z = 4\mu\text{m}$.

condensate with $N_s = 7$ solitons after $\tau = 1.5\text{ms}$ of free expansion, with the numerical grid resolution of $\Delta z = 0.05\mu\text{m}$, and the density encoded in colors. The lower is the same picture with a resolution of $\Delta z = 4\mu\text{m}$, gained by summation over 80 grid points. Furthermore, the limited time resolution and the destructive absorption imaging, often used in experiments, do not allow for the observation of the trajectory of a soliton. It is therefore necessary to isolate other observables to identify the solitonic state.

Hence, at this point our main interest is the impact of solitons on certain observables measurable in experiments. Because of that the quench, during which solitons are created, has not been simulated. Instead we focus on the differences that occur if solitons are present in the system. The initial state of the condensate is, in accordance with the experimental observations, approximated as an overly broad TF bulk density. Numerically this is achieved by calculating a TF state for a trapping potential $\omega_{\text{init}} < 23\text{Hz}$ and changing the frequency to the experimental value of $\omega = 23\text{Hz}$. The initial frequency ω_{init} is determined through comparison of the scaled axial amplitudes r , the initial width of the condensate, and the initial

atom number after the quench obtained from the experimental data. For a slow quench-rate, i.e. small soliton numbers and a strong breathing excitation, we get the parameters $\omega_{\text{init}} = 15\text{Hz}$, $r \approx 0.45$, and $R_{TF}^{\text{init}} \approx 34\mu\text{m}$. This regime is of particular interest because we expect finite size effects to be relevant. Furthermore, for small soliton numbers the diluteness criterion for the soliton ensemble is fulfilled, and we can safely sample the state in local density approximation. We differ from the experiment in that we take these parameters for the initial state throughout this chapter. In the experiment the number of solitons is dependent on the quench rate, and for different quench rates the parameters for the initial state change. Because the results obtained in this chapter can be utilized for a wide range of systems we restrict for simplicity the presented analysis to the parameters given above. The effects of highly excited states are addressed in the last part of Sect. (5.3).

The influence of temperature is studied in the regime of a quasicondensate. Density fluctuations are found to be highly suppressed, but phase fluctuations are assumed to be still present in the system. Although it is not possible to define a temperature of the gas after the quench, the quasicondensate regime is a perfect model to study the influence of phase fluctuations on the system. The initial state in the condensate as well as the quasicondensate regime is sampled, according to the corresponding Wigner distributions (Appendix A.2).

5.2 Measurement of the single-particle momentum distribution

Since our goal is to characterize the solitonic state through the effect of solitons on the momentum distribution it is necessary to study how it can be measured in experiments. The basic idea is that for a non-interacting gas, in absence of a trapping potential, the momentum of any particle is a conserved quantity. Hence also the one-body momentum distribution is constant in time. To clarify how this can be used to measure the momentum distribution, we consider an ideal Bose gas initially confined in a region L centered around zero. The probability of finding a particle with momentum $|p| = \hbar|k|$ is assumed to be equal for any point in L . If we let the system evolve freely, *e.g.* by switching off the traps, for a time τ a particle has moved to the position $z(\tau) = (\hbar k/m)\tau + z_0$. Since every point z_0 occurs with the same probability, we see that for a given momentum k with occupation $n(k)$ all particles can be found in a region $[z^-(k, \tau), z^+(k, \tau)]$ with $z^\pm = (\hbar k/m)\tau \pm L/2$. Which means that the momentum distribution is accessible via a density measurement of the expanded cloud through the relations:

$$\begin{aligned} k &\simeq z(\tau) \frac{m}{\hbar\tau} \\ n(k) &\simeq \int_{z^-(k, \tau)}^{z^+(k, \tau)} n(z, \tau) dz . \end{aligned} \tag{5.1}$$

The exact equality only holds in the limit $\tau \rightarrow \infty$. For $\tau < \infty$ we have a finite resolution and can only distinguish between momentum modes k and $k + \Delta k$ if $z^+(k, \tau) < z^-(k + \Delta k, \tau)$, or equivalently

$$\Delta k > \frac{mL}{\hbar\tau} . \quad (5.2)$$

Together with the so called *in Situ* (iS) radius L , which is the extent of the cloud before the expansion, this inequality leads to a definition of the *in Situ radius in momentum space*:

$$k_{\text{iS}} = \frac{mL}{\hbar\tau} . \quad (5.3)$$

This sets a boundary below which the momentum distribution cannot be measured for a finite time τ of free evolution, by simply switching off the trap. In contrast to the in Situ momentum distribution numerically obtained by a Fourier transform of the field, in the following the momentum distribution obtained via a measurement of the expanded density is referred to as being *pulled back* (pb) into momentum space through Eq. (5.1). Where there is no risk for confusion the pulled back in Situ radius will simply be referred to as the in Situ radius. Usually the momenta below k_{iS} are not accessible. However, Shvarchuck et al. [61] showed that, in the presence of a quadrupole excitation, these low momenta become accessible as a consequence of the oscillating edges of the cloud

$$\frac{R(t)}{R(0)} = 1 + r \cos(\omega_b t) , \quad (5.4)$$

where ω_b is the frequency of the breathing excitation and $r = (R_{\max} - R_{\min})/2R(0)$ is the scaled axial amplitude. This means that the in Situ radius is time dependent:

$$\frac{k_{\text{iS}}(t, \tau)}{k_{\text{iS}}(0, \tau)} \approx 1 + \left(\frac{\pi\omega_z^2}{2\omega_{\perp}} - r\omega_b \sin(\omega_b t) \right) \tau . \quad (5.5)$$

The first term in brackets corresponds to the axial expansion kick caused by the decline of the chemical potential [15]. The above equation supports solutions for which the in Situ radius becomes zero. This allows for the measurement of the low momenta via a finite time of free expansion. As an analogy to optics, the measurement at this point is referred to as *in focus*. Solving it for t or τ at this point leads to:

$$\begin{aligned} \tau &= \left(r\omega_b \sin(\omega_b t) - \frac{\pi\omega_z^2}{2\omega_{\perp}} \right)^{-1} \\ t &= \frac{1}{\omega_b} \arcsin \left(\frac{\tilde{r}}{r} \right) \\ \text{with } \tilde{r} &= \frac{1}{\omega_b \tau} + \frac{\pi\omega_z^2}{2\omega_{\perp} \omega_b} . \end{aligned} \quad (5.6)$$

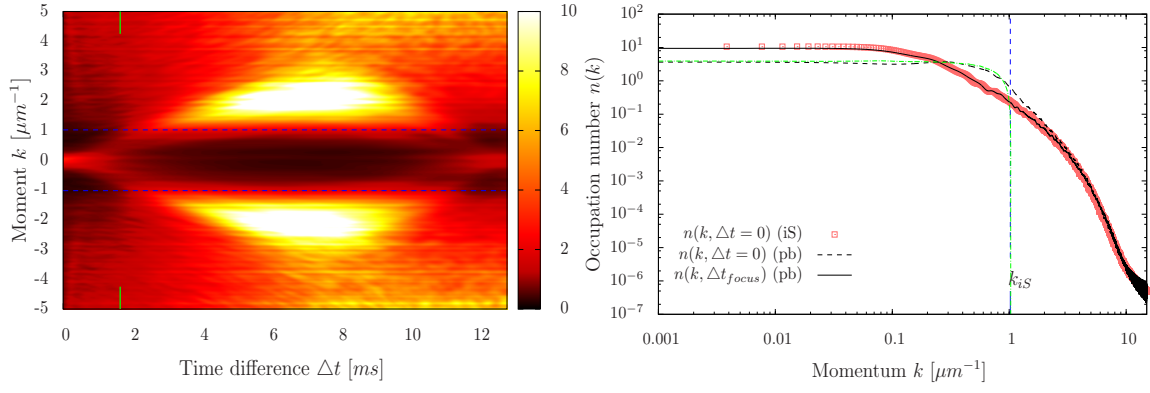


Figure 5.2: Momentum distribution measurement via free expansion. Right picture: ratio of the in Situ and pulled back momentum distribution encoded in colors as a function of the time difference Δt with the pulled back in Situ radius (blue lines) and the point of focus (green lines); Left picture: In Situ momentum distribution at $\Delta t = 0$ (red squares), pulled back momentum distribution in focus at $\Delta t = 1.64\text{ms}$ (solid black line), pulled back momentum distribution at $\Delta t = 0$ (dashed black line), pulled back in Situ density at $\Delta t = 0$ (dashed green line), and the in Situ radius (vertical blue line).

Since in our case $\tau = 46\text{ms}$ is fixed, we see from the second equation that a measurement in focus is possible for a scaled axial amplitude $r \geq \tilde{r} \approx 0.1$, obtained from the experimental parameters. In Fig. (5.2) this effect is displayed for an ensemble of 250 configurations of a condensate with $N_s = 7$ randomly distributed solitons and a breathing excitation of $r \approx 0.41$, corresponding to an experimental quench-rate $R_Q \approx 4\text{kHz/ms}$. In the left picture the ratio between the in Situ momentum distribution at the maximum extent t_0 of the cloud and the pulled back momentum distribution at a later time $t_0 + \Delta t$ for half a breathing period, is displayed in colors as a function of Δt . The horizontal blue lines mark the pulled back in Situ radius for a measurement without the breathing excitation. The vertical line (green) marks the predicted time difference $\Delta t_{focus} = 1.64\text{ms}$ for a measurement in focus. At this point we find a ratio of approximately one across the whole momentum range and therefore good accordance of the in Situ and pulled back momentum distribution. The right picture shows the in Situ momentum distribution at $\Delta t = 0$ (red squares), the pulled back momentum distribution after expansion at $\Delta t = 0$ (black dashed line) and $\Delta t = \Delta t_{focus}$ (black solid line), and the pulled back in Situ density distribution at $\Delta t = 0$ (green dashed dotted line) on a double-logarithmic scale. The horizontal line marks again the pulled back in Situ radius, below which the expanded density without a breathing excitation displays the in Situ density rather than the in Situ momentum distribution. This can also be seen in the left picture, where the ratio is smaller than one for times $\Delta t < \Delta t_{focus}$. At later times $\Delta t > \Delta t_{focus}$ we see a ratio bigger than one for $k > k_{is}$ caused by the widening of the in Situ momentum distribution and the collapse of the expanded density. As can be seen from the right

picture, it is possible for an expansion time of $\tau = 46\text{ms}$ to identify the solitonic state using the typical shape of the spectrum, as described in the last chapter, if we measure in focus. Otherwise k_{iS} is too large and that the k^{-2} power-law cannot be observed.

In the case of an interacting gas the momentum of a particle is, due to collisions, in general not preserved and *e.g.* hydrodynamic equations have to be used to describe the free evolution [64]. This problem can be solved by using Feshbach resonance [17], where the scattering length is turned to zero and the gas is non-interacting. However, if the gas is diluted during the expansion, so that the mean time between collisions becomes larger than τ , effects caused by the collisions of atoms can safely be neglected. For a quasi-one-dimensional condensate the latter is applicable. Due to the tight confinement the gas first expands rapidly in the transversal directions [15], whereas the longitudinal density and momentum distributions remain nearly unchanged, thereby diluting the gas so that the expansion becomes ballistic and the formulae given above can be used. In order to analyze the influence of the diluting process, we simulated a free expansion of the cloud, where the coupling constant was ramped down during the first period τ_{ramp} . For parameters $\tau_{\text{ramp}} = 0.5\text{ms}$ and $g_{1D}(\tau) = \sqrt{1 - (\tau/\tau_{\text{ramp}})^2}$, no change in shape of the momentum distribution is found. Therefore it is possible to observe the typical solitonic momentum distribution, even if the gas is still interacting as it undergoes the diluting process.

5.3 Time evolution

We will now examine the time evolution of the system, regarding two different initial soliton distributions (Fig. (5.3)). The distribution in the left picture is flat inside a circle of radius one around the center of phase space (referred to as PSD1). The distribution on the right side has a higher probability of finding a soliton near the center of phase space (PSD2) and is one example of a non-uniform distribution for which the finite size effects are enhanced. It can *e.g.* be achieved through condensate collisions with an imprinted phase difference between the condensates. Also the effects of an anharmonicity of the longitudinal trapping potential are analyzed. The particular shape of the anharmonic potential will be given later on. In the following all simulations are done on a grid of $G = 32768$ grid points, with a grid spacing $a_G = 0.05\mu\text{m}$, obeying the conditions given in Chapter 2, and therefore ensuring the independence of the solutions on the energy cutoff and convergence of the expanded density to the in Situ momentum distribution. The in Situ density images are in general not presented, because of their similarity to Fig. (5.1), and are only shown if significant differences occur. Because we are also interested in the applicability of the results to experimental measurements, we present here the coarse-grained images of the expanded density with a resolution of $4\mu\text{m}$.

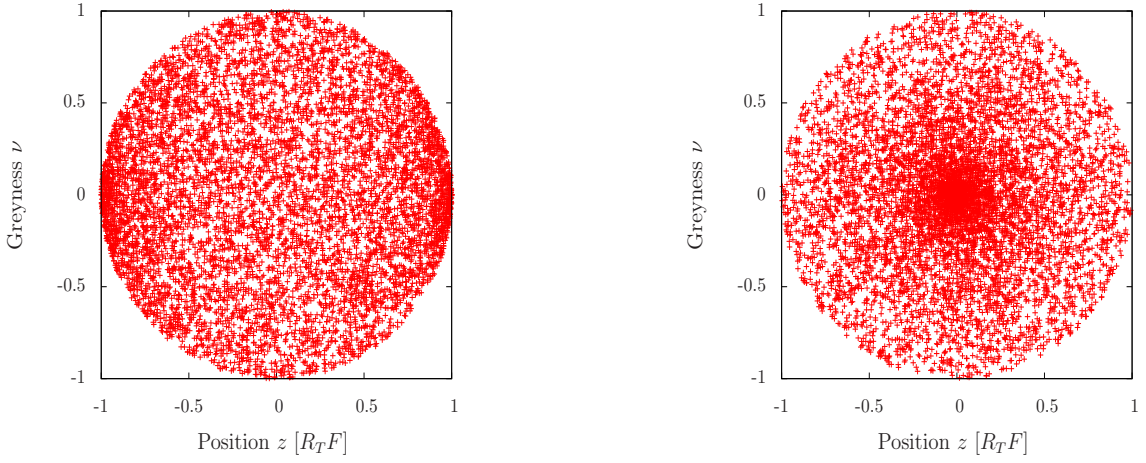


Figure 5.3: Initial soliton distributions displayed in phase space. Left picture: Flat distribution inside a circle of radius one (PSD1); Right picture: Higher probability of finding a soliton near the center of phase space (PSD2)

5.3.1 Condensate regime

Let us first take a look at the case of a harmonic trapping potential. The picture at the top of Fig. (5.4) shows one breathing period of the density after free expansion for a condensate with no solitonic excitations. In the in Situ momentum space the cloud oscillates with twice the breathing frequency, whereas in the density after free expansion the two periods do not have the same length. This is a result of the finite expansion time τ , for which a collapsing cloud has its focus at non-vanishing momenta of the edges. Therefore the released condensate has a minimal width shortly before the point of minimal extent in Situ. Although there is an interior structure present, caused by the interaction of particles, the momentum distribution is almost constant and peaked around zero. Furthermore, these structures become less pronounced for longer hold times, and since the solitonic state is a quasi-stationary state during the time evolution to thermal equilibrium, the effects caused by solitons are stable over many breathing periods. A closeup of the first and second breathing mode (middle and bottom picture of Fig. (5.4) respectively) shows that during the inward breathing phase (middle picture) the momentum distribution is always peaked around zero, whereas for the outward breathing phase (bottom picture) a double peak structure appears. However, since the occupation number of the zero mode rises shortly after the appearance of the double peak structure, this effect is not very strong. Also, close to the points of smallest extent the momentum distribution has a pronounced peak at the zero mode.

We will now investigate how the momentum distribution changes if solitonic excitations are present. In Fig. (5.5) one breathing mode of the condensate with one soliton distributed according to PSD1 (top picture), according to PSD2 (middle picture), and two solitons distributed according to PSD2 (bottom picture) are displayed. For small soliton numbers finite size effects become relevant, as can be seen

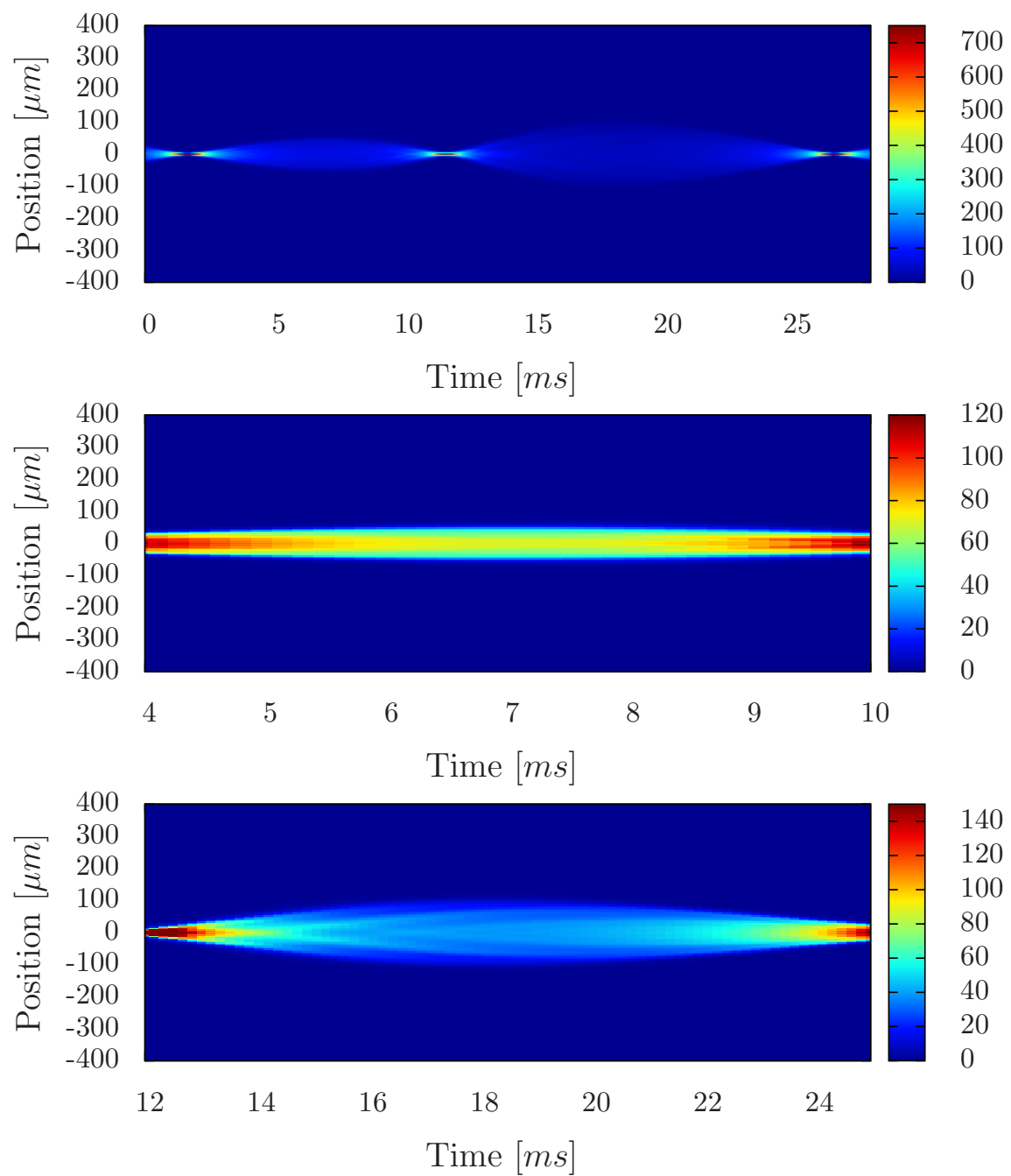


Figure 5.4: Time evolution of the density after free expansion for a condensate without solitonic excitations. Upper picture: One breathing period; Middle picture: Closeup on the first (inward breathing) period; Lower picture: Closeup on the second (outward breathing) period

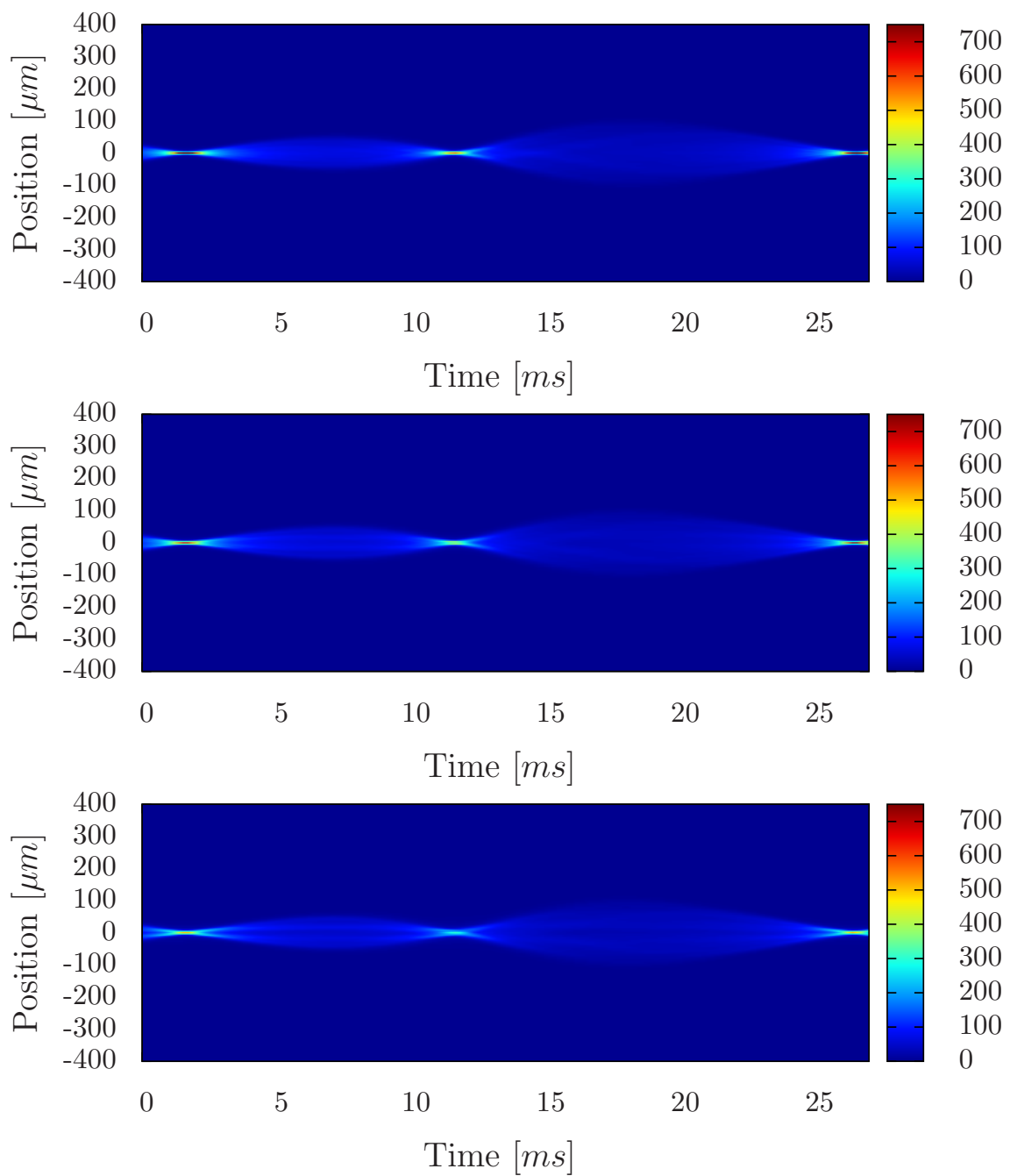


Figure 5.5: Time evolution of the expanded density for one breathing period. Upper picture: One soliton distributed according to PSD1; Middle picture: One soliton distributed according to PSD2; Lower picture: Two solitons distributed according to PSD2. We can see the finite size effects increase from top to bottom.

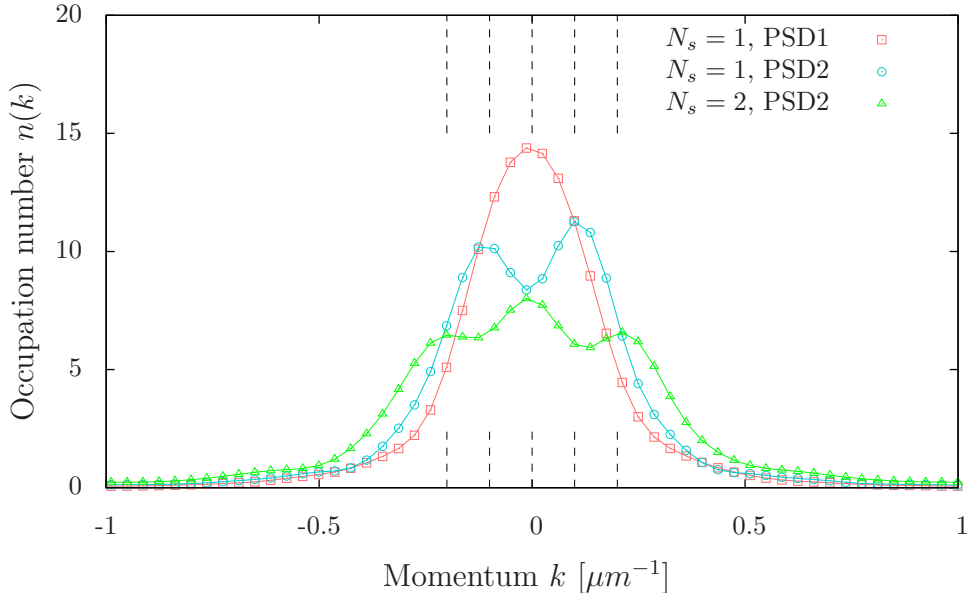


Figure 5.6: Snapshot of the pulled back momentum distribution in focus for the point of smallest extent of the condensate for: One soliton distributed according to PSD1 (red); One soliton distributed according to PSD2 (blue); Two solitons distributed according to PSD2 (green). The solid lines are a guidance for the eye. Horizontal lines mark the equidistant positions of the peaks.

from the double peak structure near the outward breathing phase. This is more prominent in the case of an inhomogeneous soliton distribution, where it takes the form of a stable double peak structure during the inward breathing phase. In the case of a homogeneous distribution the latter effect is not visible, which is in accordance with the analytical predictions, because the critical velocity for the emergence of a double peak structure is close to zero. Nevertheless, a double peak emerges shortly after the point of smallest extent in the expanded density. The solitons are slowed down during the inward breathing phase, by collisions with the edges of the cloud, and are at the point of smallest extent near the center of the trap. Therefore the double peak structure becomes visible near this point. As the cloud expands, the mean velocity of the solitons rises causing the double peak to vanish. For the inhomogeneous soliton distribution (PSD2) the mean velocity of solitons is smaller, therefore the finite size effects are visible over a longer period of time. For two solitons distributed according to PSD2, a double peak structure is visible even during the outward breathing phase. Fig. (5.6) shows a snapshot of the expanded density in focus for the resolution of the numerical grid simulations at the point of smallest extent, where finite size effects are most dominant. The solid lines are a guidance for the eye. The horizontal lines are the analytical predictions for the positions of the peaks. Note that they are equidistant, due to the convolution argument given before. The small asymmetry of the double peak shows a mean flow of the system

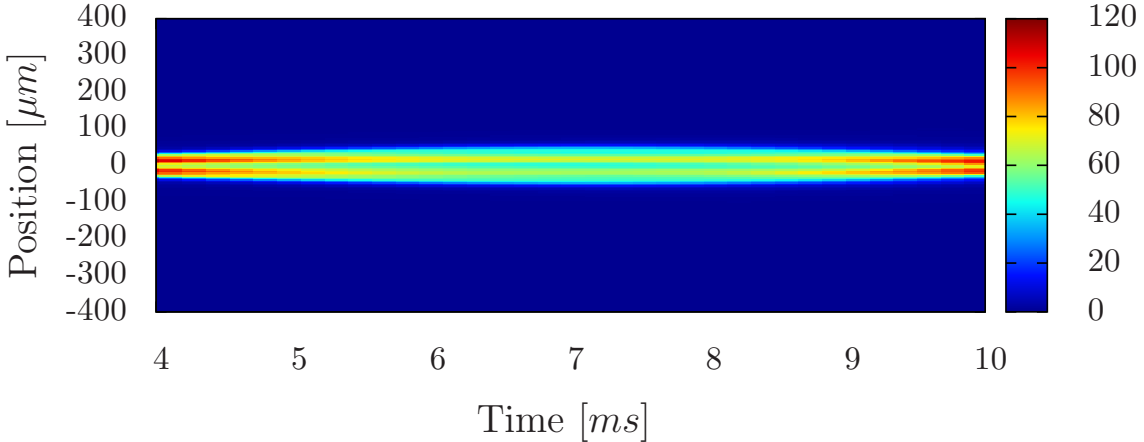


Figure 5.7: Closeup on the second breathing mode of the expanded density for a condensate with two solitons distributed according to PSD2. Note the finite size effect in the form of a stable double peak structure.

and is an effect of the finite number of simulations used for the plot. It vanishes in average for a higher number of realizations. The reason that a triple-peak structure for two solitons in the time evolution of the condensate is not seen, lies in the fact that the breathing oscillation diminishes the occupation numbers of the low energy modes. Therefore only a double peak structure is visible (Fig. (5.7)). However, this ensures the emergence of a double peak even if the soliton number is small but different in every realization, which is a more probable scenario than a fixed number of solitons in every run. It is worth mentioning that the structure of the momentum distribution is also visible for a resolution of $4\mu m$. For higher soliton numbers these effects vanish in accordance with the convergence of \tilde{g}_1 to an exponential function. The results are in good accordance with the analytical predictions. Due to the fact that we simulated the free expansion of the cloud and adopted a realistic resolution for the measurements, the results suggest new possibilities for characterizing the soliton distribution and the point at which solitons start to form or at which nearly all of them have decayed.

Anharmonicity of the trapping potential

Until now we have regarded a condensate in an harmonic confinement at $T \ll T_\theta$, for which phase fluctuations are suppressed. As a next step we investigate, how a small anharmonicity of the trapping potential affects the dynamics of the condensate. We chose the simplest form of an anharmonic trapping potential

$$V(z) = \frac{1}{2}m\omega^2(z^2 + \lambda z^4), \quad (5.7)$$

with the strength of the anharmonicity given by λ . The potential is harmonic near the center of the trap, but has a steeper rise at the edges. The position at which

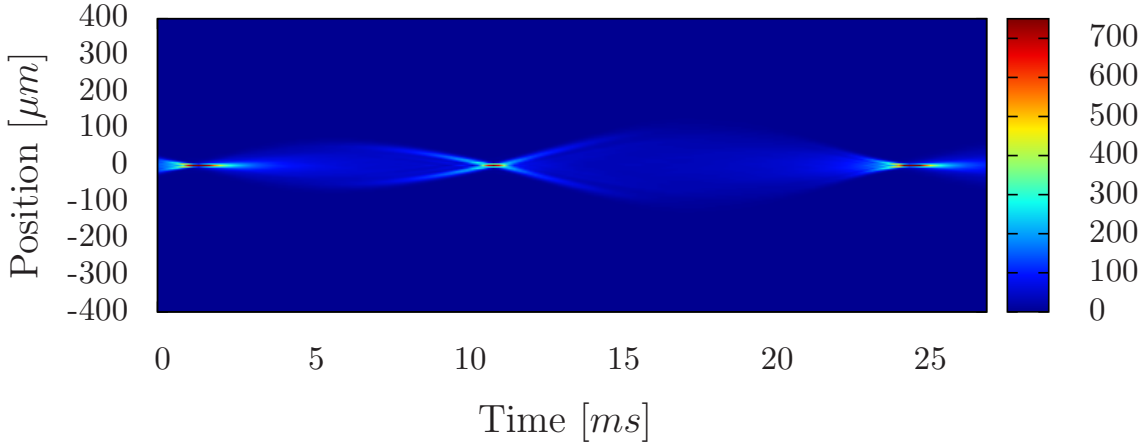


Figure 5.8: First breathing period of the density after free expansion for a condensate without solitons in an anharmonic potential. Note the strong double peak structure around the point of smallest extent of the in Situ density

the anharmonicity becomes relevant depends on the value of λ . The time evolution of the density after free expansion for a condensate without a solitonic excitation and an anharmonicity of $\lambda = 4 \times 10^{-7}$ is shown in figure (5.8). The factor λ was chosen so that the time evolution in Situ does not differ drastically as compared to the case of an harmonic confinement. However, note the slightly shorter period of the breathing. A strong double peak structure is visible before and after the point of minimal extent. It is caused by the anharmonicity of the potential. The atoms at the edge of the cloud have a higher potential energy, as compared to a harmonic confinement. Therefore the edges move faster than the interior of the cloud, leading to an increase of the density as the cloud collapses and expands. The strength of the anharmonicity λ defines the distance from the center of the trap where the peaks vanish, due to the dominance of the z^4 -term in the trapping potential. In the case of an ensemble of solitons distributed according to PSD1 we cannot see the finite size effects, because of the strong double peak caused by the anharmonic potential. However, for solitons distributed according to PSD2 the most prominent effect is the stable double peak structure during the inward breathing phase. As can be seen in Fig. (5.9), which shows a closeup of the inward breathing phase without (upper picture) and with one soliton distributed according to PSD2 (lower picture), this effect is still visible even in the presence of an anharmonicity. Since an imperfection of the trapping potential is not unusual for an experimental setup, we show that a characterization of the solitonic state through the measurement of the momentum distribution in focus is still possible. Therefore we simulate the time evolution of a condensate with $N_s \in [8, 12]$ solitons randomly chosen for every realization and distributed according to PSD1. Interestingly the strong double peaks caused by the anharmonicity become less pronounced as we increase the number of solitons (see Fig. (5.10)). This displays the effect, that with an increasing number of defects, exterior influences become less pronounced. We will discuss this behavior in the last

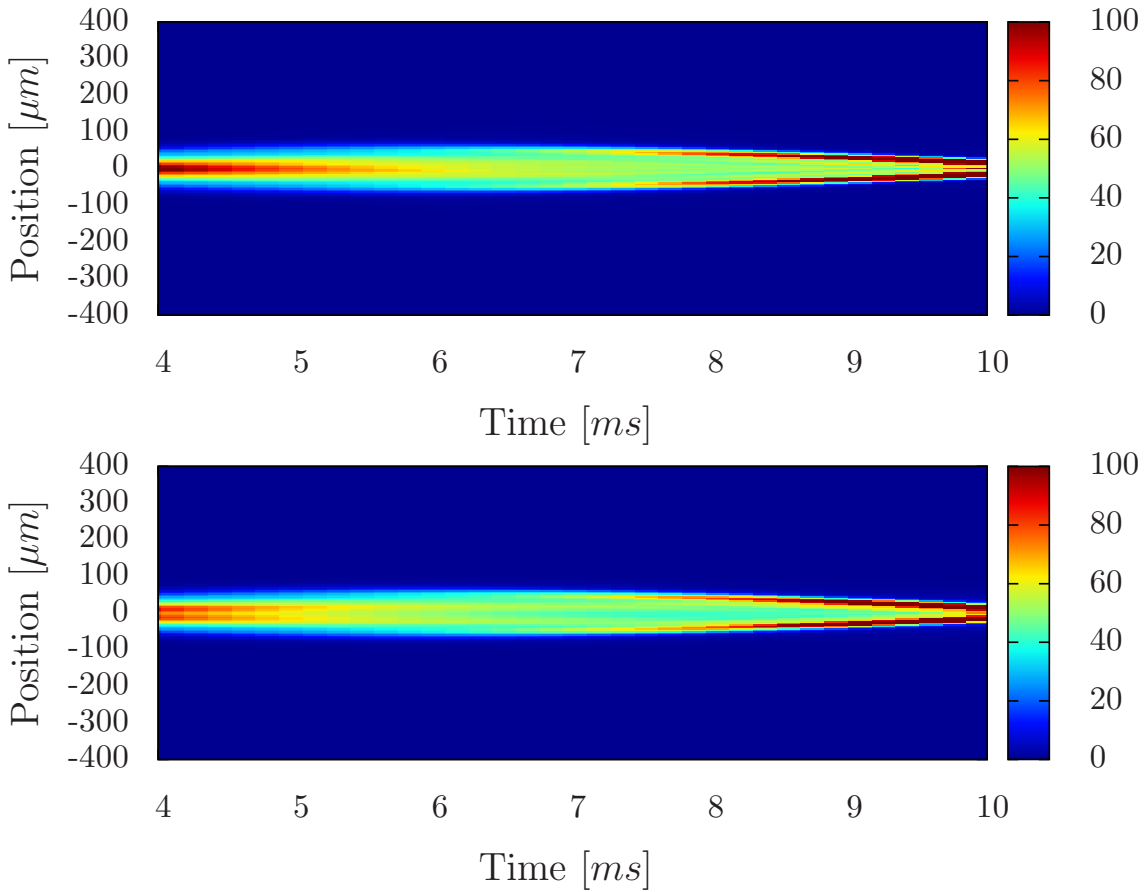


Figure 5.9: Closeup on the inward breathing phase of the density after free expansion for an anharmonic trapping potential. Upper picture: condensate without solitons; Lower picture: One soliton distributed according to PSD2. Note the smaller double peak structure for the lower picture caused by the soliton.

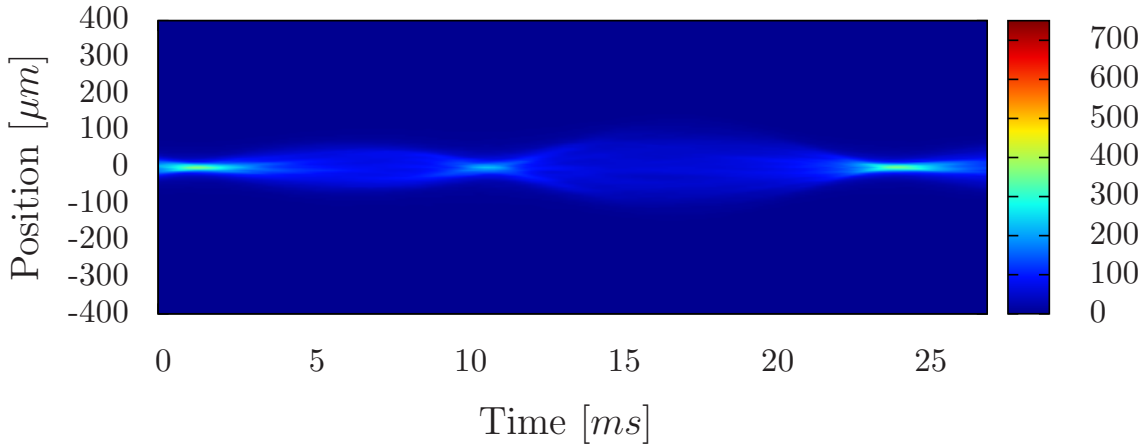


Figure 5.10: One breathing period of the density after free expansion of a condensate with $N_s \in [8, 12]$ solitons in an anharmonic trapping potential.

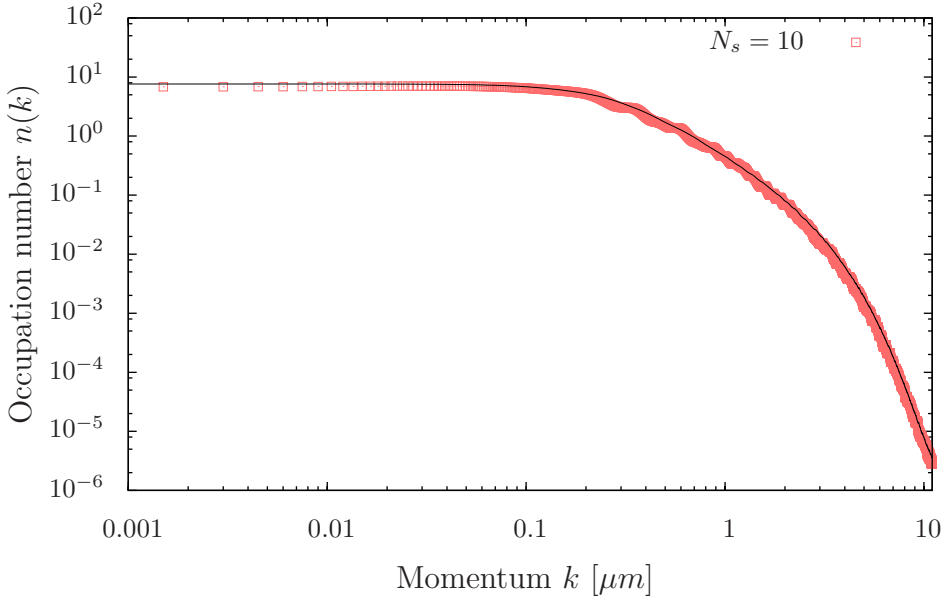


Figure 5.11: Snapshot of the pulled back momentum distribution of Fig. (5.10) measured in focus for the point of maximal extent in Situ. The typical shape of the momentum distribution is preserved in the presence of an anharmonic confinement.

part of this section. For a momentum distribution measured in focus at the maximal extent of the cloud in Situ we get the expected shape in the presence of solitons (Fig. (5.11)). The solid line is the analytical prediction of equation (4.32). The point of maximal extent in Situ was chosen because the soliton density n_s is small, *i.e.* $k_{n_s} \ll k_{\text{kink}}$, and the power-law regime is clearly visible. Although, we see good accordance and are therefore able to identify the solitonic state via a measurement of the momentum distribution in the presence of an anharmonic trapping potential, it is necessary to identify the specific anharmonicity in an experiment, in order to estimate its influence. This can e.g. be done by measuring the frequency for a dipole oscillation of the cloud.

5.3.2 Quasicondensate regime

Since the influence of solitons on the low momentum modes is a consequence of the accompanying phase jumps, it is of great relevance to study the effects of other random phase fluctuations on the momentum distribution. As discussed in Chap. (2.1) the quasicondensate regime is dominated by rare but strong phase fluctuations that increase with temperature (see Fig. (2.1)). This behavior of the phase is comparable to an ensemble of solitons randomly distributed in phase space, which shows the particular difference between solitons and the quantized defect in two and three dimensions. The similarity can also be seen by comparing the normalized first order coherence function for a quasicondensate with $T_\theta \ll T \ll T_d$ and for a soliton

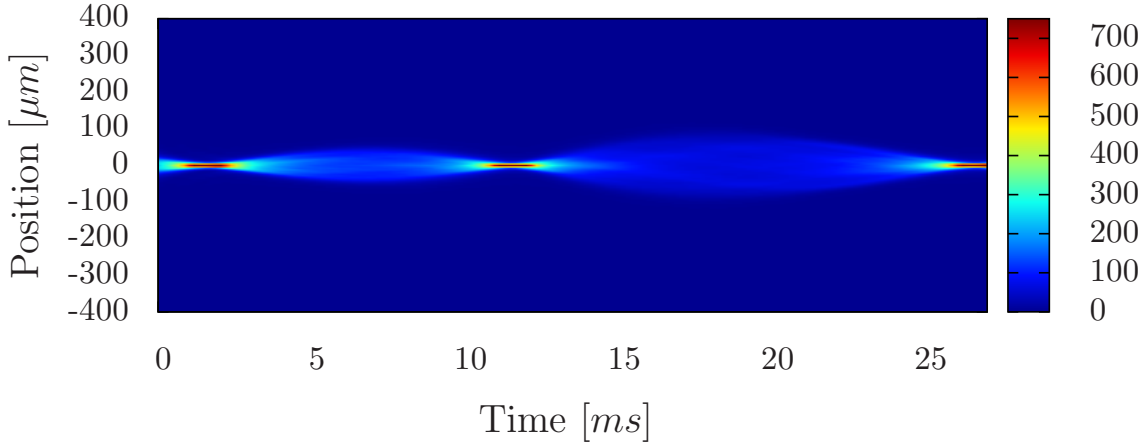


Figure 5.12: Time evolution of the density after free expansion for a quasicondensate at $T = 30\text{nK}$ without solitons.

ensemble with $N_s \geq 10$, where both exhibit an exponential behavior. In this regime the main difference between a solitonic state and a quasicondensate is the density depression associated with the soliton. This leads to the characteristic exponential decay of the momentum distribution for momenta larger than the inverse healing length. Whether or not this exponential decay is visible depends on the temperature of the system. For a rising temperature the thermal tail of the spectrum rises. If it reaches the occupation number of the solitonic power-law (at $k < k_{\text{kink}}$) the exponential decay vanishes and a single k^{-2} power-law is visible reaching far beyond k_{kink} . In the right hand picture of Fig. (5.13) we show the spectra for different temperatures for an ensemble of 1000 configurations with $N_2 = 10$ solitons distributed according to (PSD1). We can see that the high energy modes rise with temperature causing the exponential decay to vanish. It is therefore clear that we can observe the typical shape of the solitonic spectrum, if the temperature is sufficiently low. Fig. (5.12) shows the time evolution of the expanded density for a quasicondensate with $T = 30\text{nK}$ and no solitonic excitations. The shape of the cloud is nearly the same, as compared to the condensate regime, except that the interior structure is less symmetric, caused by the initial random phase fluctuations. However, the momentum distribution in focus has a prominent change in shape, as can be seen on the left hand side of Fig. (5.13). The solid black line shows the k^{-2} power-law present due to the thermal fluctuations of the phase. Note that the power-law regime reaches far beyond k_{kink} making it possible to distinguish this spectra from the solitonic case.

The double peak structure, caused by solitons, is in the thermal state only visible for $T \leq T_\Theta$. For higher temperatures it is obvious that the finite size effects vanish, as the g_1 already exhibits a sharp decline due to the thermal phase fluctuations. The very low temperature boundary for the disappearance of the double peak structure is reasonable considering the similarity of a quasicondensate state and an ensemble of randomly distributed solitons. The random phase fluctuations lead to an effective rise of the mean velocity of the soliton ensemble as compared to the condensate

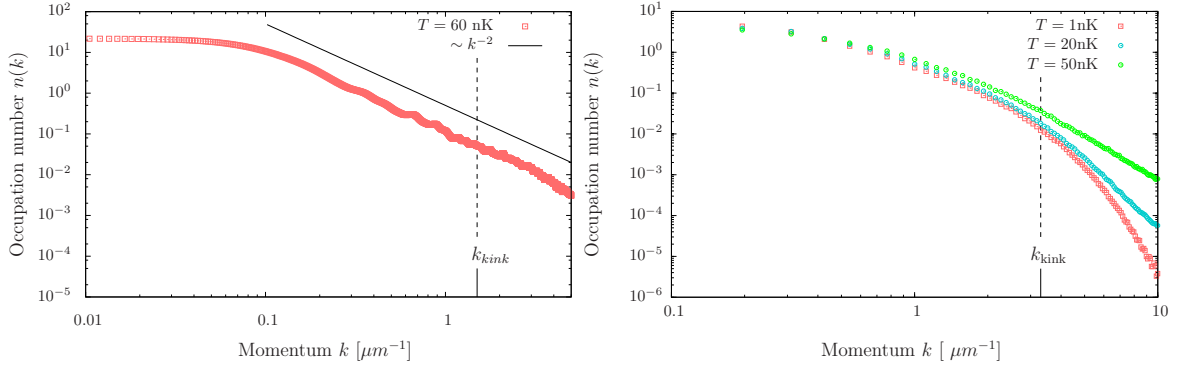


Figure 5.13: Momentum distribution for different quasicondensates. Left picture: Pulled back momentum distribution in focus corresponding to Fig. (5.12). The thermal power law reaches far beyond k_{kink} ; Right picture: Momentum distribution for an ensemble of 1000 configurations with $N_s = 10$ solitons randomly distributed according to (PSD1) for $T = 1 \text{ nK}$ (red squares), $T = 20 \text{ nK}$ (blue circles) and $T = 50 \text{ nK}$ (green triangles). Note the rise of the thermal tail and the vanishing exponential decay above k_{kink} (dashed horizontal line) for increasing temperature.

regime. Therefore the mean velocity lies above the critical velocity ν_{crit} for the emergence of a double peak structure and the finite size effects vanish. However, it depends on the certain distribution of solitons if these finite size effects occur at higher temperatures.

5.3.3 Many soliton state

Having seen the influence of small soliton numbers, we now like to examine the other extreme, namely the case of highly excited states. In the regime of an intermediate number of defects it depends on the soliton distribution if finite size effects are still visible. However, as long as $k_{n_s} \ll k_{\text{kink}}$ we can determine the solitonic state through the characteristic momentum distribution for a measurement in focus. If we increase the number of solitons further we enter the state where the momentum distribution is dominated by the defects. Exterior influences, such as e.g. the quadrupole excitation, only affect the shape of the momentum distribution implicitly by modulating the density of defects. Fig. (5.14) shows the in Situ density (left column) and the density after free expansion (right column) for an ensemble of 50 configurations with $N_s = 30, 50, 100$ solitons (from top to bottom) distributed according to PSD1. The different densities, in Situ and after free expansion, are due to the different resolutions of $0.05 \mu\text{m}$ and $4 \mu\text{m}$ respectively. There is a drastic change in the behavior of the system as compared to the time evolution for small soliton numbers. The oscillations of the in Situ density decrease and have nearly vanished in the last picture. The effect is more prominent in the expanded density, which for small soliton numbers oscillates, apart from the asymmetry explained before, with

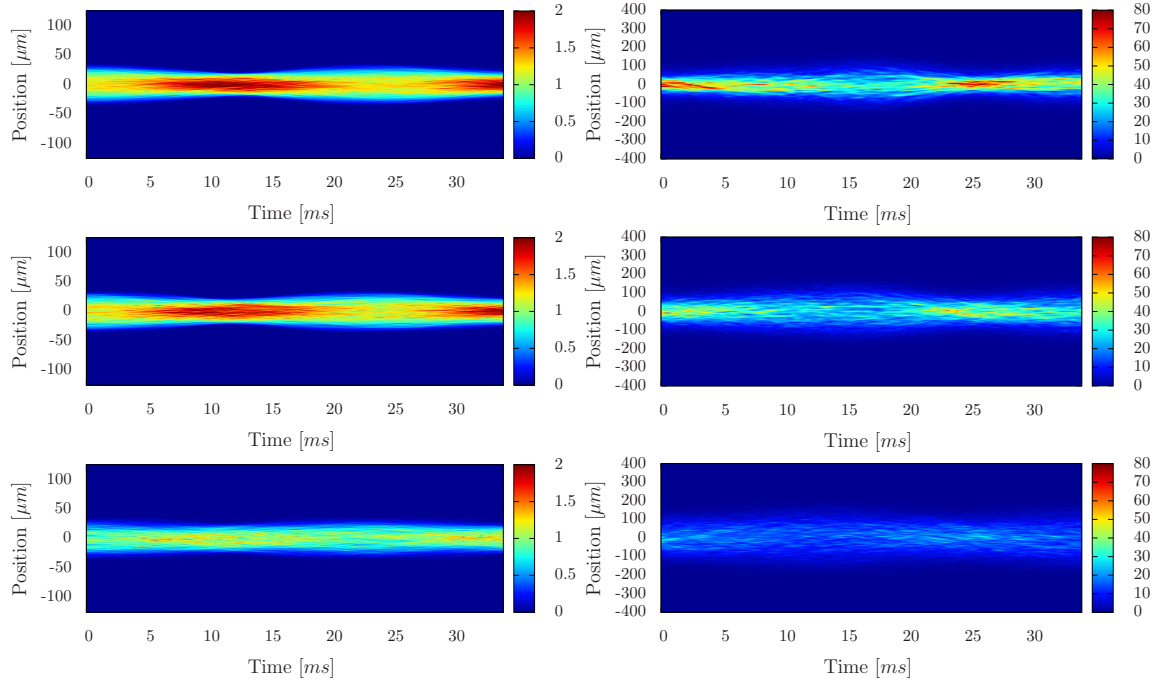


Figure 5.14: One breathing period averaged over 50 realizations for highly excited states. Left column: In Situ density; Right column: Density after free expansion respectively, with the density encoded in colors. differences in the density are caused by different resolution. Upper picture: $N_s = 30$; Middle picture: $N_s = 50$; Lower picture: $N_s = 100$. Note the decrease of the breathing oscillation in Situ, and the change in the oscillation for the expanded density

twice the breathing frequency. In contrast we see an oscillation with frequency ω_b for the highly excited states. For $N_s = 30$ there is still a small decrease in width at the point of minimum extend in Situ, which vanishes completely as N_s is increased further. This effect is best seen in the time evolution of the kinetic (solid lines) and potential (dashed lines) energy (Fig. (5.15)). For comparison we show the time evolution of the energies for a condensate without solitons (red lines), which has the expected shape of vanishing kinetic energy at the turning points and maximum kinetic energy at the points of maximum inwards and outwards velocity. The initial kinetic energy rises with the number of defects. For $N_s = 30$ solitons we can still see a slight decrease of the kinetic energy, but for $N_s = 100$ solitons it is peaked around the point of minimum extent. This displays the fact, that the kinetic energy, and therefore the momentum distribution, is dominated by the density of the defects rather than the quadrupole excitation of the condensate. Although our analytical formula is not applicable for highly excited states, because it requires a dilute ensemble of solitons, we are still able to understand the effect by analyzing the characteristic momentum scales. For $k_{n_s} \ll k_{\text{kink}}$ we see a plateau in the momentum distribution for $k < k_{n_s}$ and an exponential decay for $k \gg k_{\text{kink}}$. If the

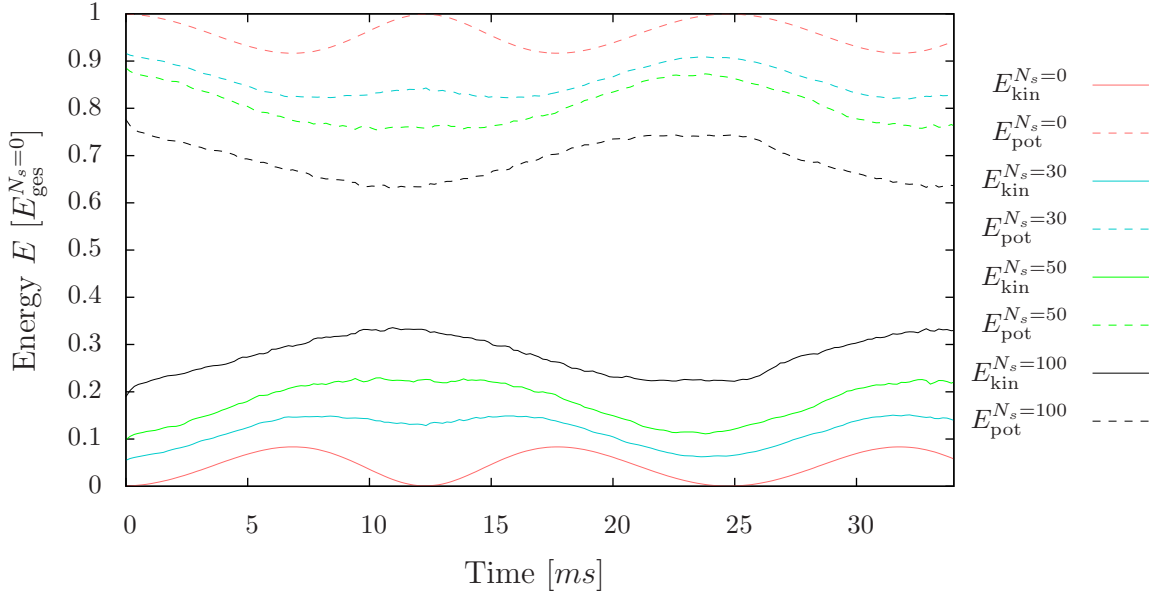


Figure 5.15: Time evolution of the kinetic (solid lines) and potential (dashed lines) energies for different soliton numbers. Note the change in frequency from $\omega_b/2$ (red) to ω_b (black) as the soliton density increases.

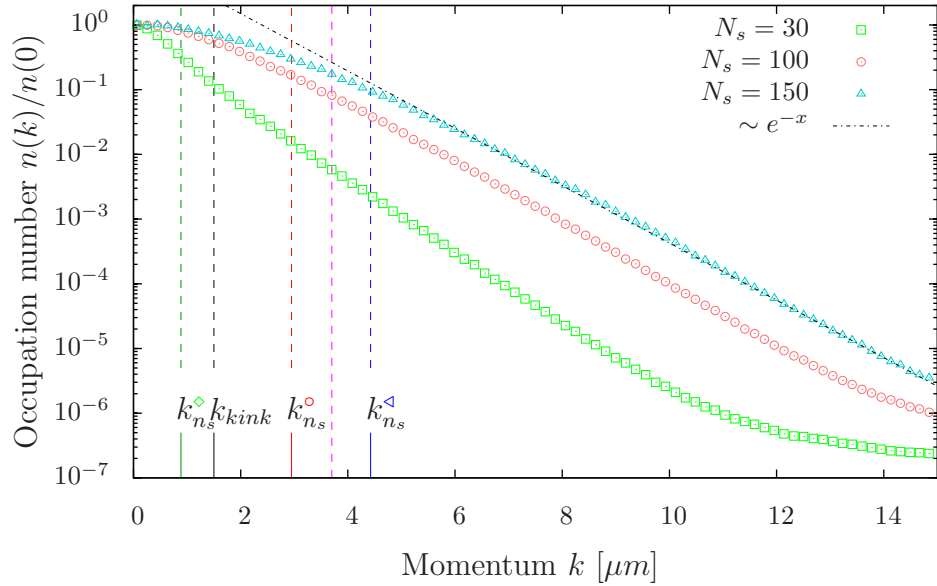


Figure 5.16: In Situ momentum distribution for $N_s = 30$ (green squares), $N_s = 100$ (red circles), and $N_s = 150$ (blue triangles), the vertical lines are the respective soliton densities (green, red, blue), the inverse healing length (black) and the FWHM at the point of maximum outward velocity for a condensate without solitons (purple). Note that for high soliton numbers, the exponential decay is given by k_{n_s} (dashed dotted line).

soliton density reaches the point where the inter soliton distances become of the order of the inverse healing length, the plateau reaches above k_{kink} and the exponential decay is characterized by the soliton density, rather than the width of the solitons. Fig. (5.16) shows the normalized in Situ momentum distribution for an ensemble of 5000 configurations with $N_s = 30$ (green squares), $N_s = 100$ (red circles) and $N_s = 150$ (blue triangles) solitons randomly distributed according to PSD1. The horizontal lines show the respective soliton densities (red, blue, green), the inverse healing length (black) and the full width half maximum (FWHM) of the expanded cloud without solitons at the point of maximum outward velocity (purple). We can see for high numbers of solitons the exponential decay for $k > k_{n_s} > k_{\text{kink}}$, below which the occupancy number only slightly decreases. This enables us to reinterpret the results above. The breathing excitation greatly influences the small momentum range, therefore the momentum distribution widens up to a maximum extent given by the purple horizontal line. As the soliton density becomes comparable to this value, the initial width of the momentum distribution is given by k_{n_s} , changes in the occupancy number for $k < k_{n_s}$ are less pronounced, and the breathing excitation only influences the width of the momentum distribution by a modulation of the density of defects. This leads to the observed stiffness of the gas.

6 Discussion and outlook

In this thesis we studied the characteristics of the solitonic states of an interacting ultracold Bose gas at finite temperature in one spatial dimension.

We succeeded in describing the turbulent state within a model of randomly distributed solitons. In this model, the turbulent state was considered to be represented at every point in time by an ensemble of solitons randomly distributed in phase space. This comparison was founded on the dynamical behavior of solitons in an ultracold Bose gas. We derived an analytic expression for the spectrum of a condensate in the presence of a dilute ensemble of solitons randomly distributed in phase space.

In the thermodynamic limit we were able to give a closed formula for the momentum distribution for an arbitrary number of solitons. We found, that the spectrum is governed by two different scales: The soliton density n_s and the inverse of the healing length ξ . The healing length determines the width of a soliton. The spectrum was found to show scaling behaviour for momenta inbetween these characteristic scales. Therefore the solitonic state was interpreted as a non-thermal fixed point during the time evolution to thermal equilibrium.

In the presence of a trapping potential, we found that nontrivial differences occur in the small momentum range of the spectrum, showing a characteristic double peak structure. We derived an analytic formula in the case of an ensemble of solitons distributed flat accross the whole condensate and succeeded in explaining the emergence of the double peak structure as a consequence for the certainty of finding the solitons in a finite region in space. In the case of small soliton numbers this leads to a huge difference in the first-order coherence function g_1 as compared to the result obtained in the thermodynamic limit. For higher soliton numbers we could explain the vanishing of this structure as a consequence of the convergence of g_1 to the exponential function obtained in the thermodynamic limit. Furthermore we confirmed, that the spectrum for an ensemble of one soliton distributed according to the generally non-uniform distribution $P(z, \nu)$ is given by a continuous deformation of the momentum distribution for an ensemble of one black soliton distributed according to $P(z, 0)$. The strength of the deformation is given by the mean value of the greyness ν of the soliton ensemble. We were able to define a critical mean velocity ν_{crit} , above which the double peak structure vanishes for any number of solitons. In the case of a non-uniform distribution we found for higher soliton numbers a multi peak structure, with equidistant peaks. We explained this effect through the convolution of the spectra for one soliton and argued that for these higher order peaks the critical velocity diminishes.

In the second part of this thesis, we analyzed the possibilities of observing the solitonic state in experiments. Therefore the time evolution of a solitonic state was

simulated, by numerically solving the one-dimensional Gross-Pitaevskii equation for an ensemble of stochastically sampled initial states on a grid. The observables are obtained by averaging over different realizations.

In order to facilitate the comparison of the results to experiments, a free expansion of the gas was simulated for the measurement of the momentum distribution. We reproduced the results of Shvarchuck et al. [61] for a momentum distribution measurement in focus. At this point the low momentum range becomes accessible, as the *in Situ* radius is focused to one point. We showed, that in the presence of solitonic excitations this technique can be used to identify the typical shape of the momentum distribution for a finite time of free expansion τ .

The possibility of measuring the solitonic state was discussed in a variety of experimental setups. Of particular interest was the possibility of observing the finite size effects.

We found, that for certain non-uniform distributions of solitons finite size effects are enhanced, and show a characteristic stable double peak structure in the expanded density during the inward breathing phase. The predicted multi-peak structure was observed for a momentum distribution measurement in focus to the point of smallest extent of the cloud. In accordance with the analytical predictions this effect is not visible for randomly distributed solitons, as in this case the critical velocity is close to zero.

The influence of temperature was addressed in the context of a quasicondensate. We found that finite size effects are highly suppressed with rising temperature, and interpreted this as an effective rise of the mean velocity of the soliton ensemble due to random thermal phase fluctuations. It was shown, that even at finite temperature a characterization of the solitonic state through the exponential decay of the momentum distribution for high momenta is possible. As long as the occupation numbers of the thermal tail of the spectrum for high momenta are sufficiently smaller than the occupation numbers for the solitonic power-law, the exponential decay is visible in the intermediate regime. This allows a distinction between the solitonic and the thermal state, although the spectra both show a power-law of k^{-2} .

Furthermore we considered the case of an anharmonicity of the trapping potential. We found a strong double peak structure in the expanded density around the point of smallest extent *in Situ*. Nevertheless, it is possible to observe the finite size effects for sufficiently low temperatures. For higher soliton numbers, the double peak structure, due to the quadrupole excitation, starts to vanish. We confirmed that the typical solitonic shape of the momentum distribution is preserved in the presence of a slight anharmonicity of the trapping potential.

In the last part we analyzed the emerging effects for high soliton numbers. We showed that for these highly excited states the quadrupole excitation is suppressed and the condensate becomes stiff. For a high soliton density, the scale above which the momentum distribution exhibits an exponential decay is given by the soliton density n_s rather than the inverse of the healing length ξ^{-1} . Therefore the momentum distribution widens, and diminishes the influence of the breathing oscillation. For very high soliton numbers the gas becomes nearly independent of exterior influences

and is dominated by the density of defects.

The results of this thesis throws new light on the possibilities of observing the solitonic state. The solitonic spectrum is stable over a wide range of physical situations, making it a promissing observable for the experimental investigation. The finite size effects occur for very low temperatures or non-uniform distribution. An interesting question is how the change of the first order coherence function affects other observables. The density-density correlation after free expansion could be a promissing observable. For very low temperatures, the cloud is a true condensate and the density-density correlation after free expansion is a constant. There is a large change in the first order coherence function for small soliton numbers and further on it is distinctly different from the exponential behavior of a condensate at higher temperatures. Because of the distinct differences between solitons and vortical excitations in higher dimensions it would be interesting for future theoretical studies to investigate the transition from 1D to elongated 3D systems. Our detailed analysis of the spectrum is an excellent starting point for comparison. Also the similarities to the thermal quasicondensate regime are an interesting topic of investigation. Recent developements show that solitons can occur spontaneously in thermal equilibrium. This indicates that solitons could be present in a wide range of systems, and therefore it is necessary to further understand their dynamics and impacts.

A Appendix

A.1 Expansion of the Hamiltonian

The Hamiltonian is expanded in orders of κ_1 and κ_2 . Because they are of the same order, all terms of the same order in κ_1 , κ_2 , $\kappa_1\kappa_2$ have to be taken into account to determine the expansion of the Hamiltonian to this order. This leads to:

$$H_0 = \sum_z l \left[-\frac{\hbar}{2m} \sqrt{\rho_0} \partial_z^2 \sqrt{\rho_0} + \frac{g_{1D}}{2} \rho_0^2 + [V(z) - \mu] \rho_0 \right] \quad (\text{A.1})$$

$$H_1 = \sum_z l \left[-\frac{\hbar^2}{2m\sqrt{\rho_0}} \partial_z^2 \sqrt{\rho_0} + V(z) - \mu + g_{1D} \rho_0 \right] \delta\hat{\rho} \quad (\text{A.2})$$

$$\begin{aligned} H_2 = \sum_z l & \left[-\frac{\hbar^2}{2m} \frac{\delta\hat{\rho}}{2\sqrt{\rho_0}} \partial_z^2 \left(\frac{\delta\hat{\rho}}{2\sqrt{\rho_0}} \right) + \frac{\hbar^2 \delta\hat{\rho}^2}{8m\rho_0^{3/2}} \partial_z^2 \sqrt{\rho_0} + \frac{g_{1D}}{2} \delta\hat{\rho}^2 \right. \\ & \left. + \frac{\hbar^2}{2m} \sqrt{\rho_0(z)\rho_0(r+l)} \frac{[\hat{\Theta}(z+l) - \hat{\Theta}(z)]^2}{l^2} \right] + E_2[\rho_0] \end{aligned} \quad (\text{A.3})$$

$$E_2[\rho_0] = -\frac{g_{1D}}{2} \sum_z \rho_0 - \frac{\hbar^2}{4ml^2} \sum_z \left[\left(\frac{\rho_0(z+l)}{\rho_0(z)} \right)^{1/2} + \left(\frac{\rho_0(z)}{\rho_0(z+l)} \right)^{1/2} \right] \quad (\text{A.4})$$

A.2 Sampling of the Wigner distribution

We give the Wigner distributions for a thermal state $T \ll T_c$ in the Bogoliubov formalism, with the wave function

$$\psi(z) = \frac{\alpha_0}{\sqrt{N_0}} \phi_0(z) + \sum_{j>0} [u_j(z)\alpha_j + v_j^*(z)\alpha_j^*] . \quad (\text{A.5})$$

The condensate and quasi-particle modes are uncorrelated and therefore can be sampled independently. Because the Wigner distribution is used to sample the occupancy number of the condensate and quasi-particle states we can directly use it to sample the initial state of the quasi-condensate derived in the second chapter by replacing the annihilation and creation operators by complex variables α .

Condensate mode

The condensate mode is well approximated by a coherent state, for which the Wigner distribution takes the form

$$W(\alpha, \alpha^*) = \frac{2}{\pi} e^{-2|\alpha - \alpha_0|^2}, \quad (\text{A.6})$$

where $|\alpha_0|^2 = N_0$. For a high occupation of the condensate we can take $\alpha_0 \approx N_0$.

Quasi-particle modes

For the thermalized Bogoliubov excitations the Wigner function takes the form of uncorrelated Gaussian quasi-probability distributions, *e.g.*

$$\begin{aligned} W(\boldsymbol{\alpha}, \boldsymbol{\alpha}^*) &= \prod_{j>0} W_j(\alpha_j, \alpha_j^*) \\ W_j(\alpha_j, \alpha_j^*) &= \frac{2}{\pi} \tanh\left(\frac{\epsilon_j}{k_B T}\right) \exp\left[-2|\alpha_j|^2 \tanh\left(\frac{\epsilon_j}{k_B T}\right)\right]. \end{aligned} \quad (\text{A.7})$$

In practice the variables $\{\alpha_j\}$ can be sampled as

$$\alpha_j = \sqrt{N_j + \frac{1}{2}} \left(\frac{x_j + i y_j}{\sqrt{2}} \right), \quad (\text{A.8})$$

with normally distributed Gaussian random variables x_j, y_j with mean zero and unit variance.

A.3 Dimensionless GPE

Because we work with numerical simulations, we need all physical quantities to be dimensionless. The easiest way to do so, is to define an initial set of dimensionful quantities

$$\begin{aligned} &\{a_G, m, \hbar, k_B\} \\ &\{[\mu m], [kg], [Js], [JK^{-1}]\}. \end{aligned} \quad (\text{A.9})$$

This enables us to express every dimension (used in this thesis) as a product of these quantities. In general natural units $\hbar = k_B = 1$ can be chosen to further simplify the equations, but the above set allows us to implement parameters in SI-units, which was more practical during the work on this thesis. We define the above set of quantities by choosing a spacial lattice constant a_G and $\omega_G = \hbar/m a_G^2$ for the time spacing. Therefore a_G is the only free parameter and it has to be chosen to fulfill the inequalities (2.10). The quasi-one-dimensional GPE in the presence of an harmonic

potential $V(z) = (1/2)m\omega_{\parallel}^2 z^2$, obtained *e.g.* by variation of Eq. (2.16), is

$$i\hbar\partial_t\psi(z, t) = \left[-\frac{\hbar^2}{2m}\partial_z^2 + \frac{1}{2}m\omega_{\parallel}^2 z^2 + 2\hbar\omega_{\perp}a_s|\psi(z, t)|^2 \right] \psi(z, t) , \quad (\text{A.10})$$

and becomes dimensionless by multiplying both sides with $\sqrt{a_G}/\hbar\omega_G$, leading to

$$i\partial_{\tilde{t}}\tilde{\psi}(\tilde{z}, \tilde{t}) = \left[-\frac{1}{2}\partial_{\tilde{z}}^2 + \frac{1}{2}\left(\frac{\omega_{\parallel}}{\omega_G}\right)^2 \tilde{z}^2 + 2\left(\frac{\omega_{\perp}a_s}{\omega_G a_G}\right) |\tilde{\psi}(\tilde{z}, \tilde{t})|^2 \right] \tilde{\psi}(\tilde{z}, \tilde{t}) , \quad (\text{A.11})$$

with the dimensionless quantities

$$\begin{aligned} \tilde{z} &= a_G^{-1}z \\ \tilde{t} &= \omega_G t \\ \tilde{\psi} &= \sqrt{a_G}\psi . \end{aligned} \quad (\text{A.12})$$

A.4 Split Operator method

For the numerical simulations we use the *split-operator-method*, because it is a numerically very stable algorithm. The energy and the particle number are exactly conserved quantities. The idea is to split the Hamiltonian $H = T + V$, where $T = p^2/2m$ is local in momentum space and $V = \tilde{V}(z) + g_{1D}|\psi(z)|^2$ is local in real space. We can write the time evolution of the field as

$$\begin{aligned} \psi(z, t) &= U(0, t)\psi(z, 0) = e^{iHt}\psi(z, 0) \\ &\stackrel{(t=\sum_i \Delta t)}{=} \prod_i e^{-i(T+V)\Delta t}\psi(z, 0) \\ &\stackrel{\text{BCH}}{=} \prod_i e^{-iT\frac{\Delta t}{2}}e^{-iV\Delta t}e^{-iT\frac{\Delta t}{2}}\psi(z, 0) + O(\Delta t^3) , \end{aligned} \quad (\text{A.13})$$

where we split the finite time t in small steps Δt . For the last equality we used the *Baker-Campbell-Hausdorff* equation. If we write down the product explicitly we can combine the two operators $e^{-iT\frac{\Delta t}{2}}$ and get the final expression for the evolution of one time step $U(t, t + \Delta t) \approx e^{-iT\Delta t}e^{-iV\Delta t}$. In second order in Δt the time evolution of the field is given by two operators, that can be evaluated locally if we insert inbetween them a fourier transform of the field. The used algorithm is a discrete *Fast-Fourier-Transform* of the *gnu-scientific-library*. The algorithm is very fast and stable, ensuring $O(\Delta t^3) \ll 1$.

A.5 Detection algorithm for solitons

In order to detect solitons during the time evolution of the system various methods can be applied. We give a short description of the algorithms created and used in

this thesis.

Detection in real space

The characteristic features of a soliton, namely the density dip and phase jump, are used to detect the soliton position in real space. The algorithm therefore requires the following steps

- The density $n(z) = \psi^*(z)\psi(z)$ is scanned for a local minimum. If the point is the global minimum on a length scale of the order of the healing length ξ , this point is labeled as a potential soliton.
- First the unphysical phase jumps of 2π , due to the finite range $\Theta \in [-\pi, \pi]$, are eliminated. At every point z_i , labeled in the first step, we look for a phase jump $\Delta\Theta$ over a range from zero up to the adjusted length scale $l(\Delta\Theta, z_j)$, which depends on the phase jump and the position of the other possible solitons. The second is done to ensure that phase jump of another soliton z_j is not in the regarded region of the possible soliton z_i .
- If a Gridpoint passes the two criteria states that there is a soliton at this point. Because l becomes larger with a decreasing phase jump, we have to implement a lower boundry $\Delta\Theta_{min}$ below which we cannot detect the soliton with this method.

Detection in phase space

The detection in phase space relies on the detection in real space but also detects the greyness of the soliton. There are three possibilities to detect the greyness

- The phase jump is connected to the greyness via $\Delta\Theta = 2\arccos(\nu)$. This method can be used at very low temperatures and for relatively low soliton numbers.
- The greyness is defined through the velocity of the soliton $\nu = v_s/c_s$. This method is very accurate in homogeneous systems. However, in a trap, where the velocity is no longer preserved, problems occur because we can only measure the time averaged greyness $\langle\nu\rangle_{\Delta t}$. The time Δt has to be large enough, so that the soliton has moved a sufficiently large distance in space.
- The density depression of a soliton at position z in a homogenous medium with density n_0 is given by $n(z)/n_0 = \nu^2$. For a trapped gas we can use the approximate expression $n(z)/\bar{n} = \nu^2$ with an average over the unperturbed background density $\bar{n} = \int_{z-2\xi}^{z+2\xi} n_0(x)dx$. This allows a computation of the greyness for arbitrary small time differences Δt .

B Bibliography

- [1] G. Aarts and J. Berges. Classical aspects of quantum fields far from equilibrium. *Phys. Rev. Lett.*, 88(4):041603, 2002.
- [2] M. H. Anderson, J. R. Ensher, M. R. Matthews, C. E. Wieman, and E. A. Cornell. Observation of Bose-Einstein condensation in a dilute atomic vapor. *Science*, 269:198, July 1995.
- [3] Peter Brockway Arnold and Guy D. Moore. QCD plasma instabilities: The nonabelian cascade. *Phys. Rev.*, D73:025006, 2006. doi: 10.1103/PhysRevD.73.025006.
- [4] J. Berges and T. Gasenzer. Quantum versus classical statistical dynamics of an ultracold bose gas. *Phys. Rev. A*, 76:033604, September 2007.
- [5] J. Berges, S. Scheffler, and D. Sexty. Turbulence in nonabelian gauge theory. *Phys. Lett.*, B681:362–366, 2009. doi: 10.1016/j.physletb.2009.10.032.
- [6] Jurgen Berges and Gabriele Hoffmeister. Nonthermal fixed points and the functional renormalization group. *Nucl. Phys.*, B813:383–407, 2009. doi: 10.1016/j.nuclphysb.2008.12.017.
- [7] Jurgen Berges and Denes Sexty. Strong versus weak wave-turbulence in relativistic field theory. *Phys. Rev. D*, 83:085004, 2011. doi: 10.1103/PhysRevD.83.085004.
- [8] H. Bethe. Zur theorie der metalle i. eigenwerte und eigenfunktionen der linearen atomkette. *Z. Phys.*, 71:205, 1963.
- [9] PB Blakie, AS Bradley, MJ Davis, RJ Ballagh, and CW Gardiner. Dynamics and statistical mechanics of ultra-cold bose gases using c-field techniques. *Advances in Physics*, 57(5):363–455, 2008.
- [10] K.J. Blow and N.J. Doran. Multiple dark soliton solutions of the nonlinear schrödinger equation. *Physics Letters A*, 107(2):55 – 58, 1985. ISSN 0375-9601.
- [11] N. N. Bogoliubov. On the theory of superfluidity. *J. Phys. (USSR)*, 11(1):23, 1947.
- [12] Satyendra Nath Bose. Plancks Gesetz und Lichtquantenhypothese. [*Am. J. Phys.* 44, 1056 (1976)] *Z. Phys.*, 26(3):178, 1924.
- [13] R. Bücker. *Private communication*. Atominstitut TU Wien.

- [14] Th. Busch and J. R. Anglin. Motion of dark solitons in trapped bose-einstein condensates. *Phys. Rev. Lett.*, 84:2298–2301, Mar 2000.
- [15] Y. Castin and R. Dum. Bose-einstein condensates in time dependent traps. *Phys. Rev. Lett.*, 77:5315–5319, Dec 1996.
- [16] Y. Castin and R. Dum. Low temperature Bose-Einstein condensates in time dependent traps: Beyond the u(1) symmetry-breaking approach. *Phys. Rev. A*, 57(4):3009, April 1998.
- [17] Cheng Chin, Rudolf Grimm, Paul Julienne, and Elite Tiesinga. Feshbach resonances in ultracold gases. *Rev. Mod. Phys.*, 82:1225–1286, Apr 2010.
- [18] K. B. Davis, M. O. Mewes, M. R. Andrews, N. J. van Druten, D. S. Durfee, D. M. Kurn, and W. Ketterle. Bose-einstein condensation in a gas of sodium atoms. *Phys. Rev. Lett.*, 75:3969–3973, Nov 1995.
- [19] R. J. Donnelly. *Quantized Vortices in Liquid He II*. CUP, Cambridge, 1991.
- [20] A. Einstein. Quantentheorie des einatomigen idealen Gases. *Sitzungsber. Kgl. Preuss. Akad. Wiss., Phys. Math. Kl.*, 1924:261, July 1924.
- [21] D. L. Feder, M. S. Pindzola, L. A. Collins, B. I. Schneider, and C. W. Clark. Dark-soliton states of bose-einstein condensates in anisotropic traps. *Phys. Rev. A*, 62:053606, Oct 2000.
- [22] P. O. Fedichev, A. E. Muryshev, and G. V. Shlyapnikov. Dissipative dynamics of a kink state in a bose-condensed gas. *Phys. Rev. A*, 60:3220–3224, Oct 1999.
- [23] R. Folman, P. Krüger, J. Schmiedmayer, J. H. Denschlag, and C. Henkel. Microscopic atom optics: from wires to an atom chip. *Adv. At. Mol. Opt. Phys.*, 48:253, 2002.
- [24] Ron Folman, Peter Krüger, Donatella Cassettari, Björn Hessmo, Thomas Maier, and Jörg Schmiedmayer. Controlling cold atoms using nanofabricated surfaces: Atom chips. *Phys. Rev. Lett.*, 84:4749, May 2000.
- [25] Thomas Gasenzer, Boris Nowak, and Denes Sexty. Charge separation in Re-heating after Cosmological Inflation. *Phys. Lett.*, B710:500–503, 2012.
- [26] M. Girardeau. Relationship between systems of impenetrable bosons and fermions in one dimension. *J. Math. Phys. (NY)*, 1(6):516, 1960.
- [27] R. Grimm and M. Weidmüller und Yu. B. Ovchinnikov. Optical dipole traps for neutral atoms. *Adv. At. Mol. Opt. Phys.*, 42:95, 2000.
- [28] W. P. Halperin and M. Tsubota, editors. *Progress in Low Temperature Physics Vol. 16: Quantum Turbulence*. Elsevier, Amsterdam, 2008.

- [29] P. C. Hohenberg. Existence of long-range order in one and two dimensions. *Phys. Rev.*, 158:383–386, Jun 1967.
- [30] T. Karpiuk, P. Deuar, P. Bienias, E. Witkowska, K. Pawłowski, M. Gajda, K. Razazewski, and M. Brewczyk. Spontaneous solitons in the thermal equilibrium of a quasi-one-dimensional bose gas.
- [31] Wolfgang Ketterle and N. J. van Druten. Bose-einstein condensation of a finite number of particles trapped in one or three dimensions. *Phys. Rev. A*, 54: 656–660, Jul 1996.
- [32] P. G. Kevrekidis and D. J. Frantzeskakis. Pattern forming dynamical instabilities of Bose-Einstein condensates. *Modern Physics Letters B*, 18(05n06): 173–202, 2004.
- [33] Takashi Kimura. Breathing modes of bose-einstein condensates in highly asymmetric traps. *Phys. Rev. A*, 66:013608, Jul 2002.
- [34] Yuri S. Kivshar and Wiesław Królikowski. Lagrangian approach for dark solitons. *Optics Communications*, 114(3–4):353 – 362, 1995. ISSN 0030-4018.
- [35] Andrey Nikolaevich Kolmogorov. The local structure of turbulence in incompressible viscous fluid for very large Reynolds numbers. *Proc. USSR Acad. Sci.*, 30:299, 1941. [Proc. R. Soc. Lond. A 434, 9 (1991)].
- [36] Elliott H. Lieb. Exact analysis of an interacting Bose gas. II. the excitation spectrum. *Phys. Rev.*, 130(4):1616, 1963.
- [37] Elliott H. Lieb and Werner Liniger. Exact analysis of an interacting Bose gas. I. the general solution and the ground state. *Phys. Rev.*, 130(4):1605, 1963.
- [38] N. D. Mermin and H. Wagner. Absence of ferromagnetism or antiferromagnetism in one- or two-dimensional isotropic heisenberg models. *Phys. Rev. Lett.*, 17:1133–1136, Nov 1966.
- [39] Raphael Micha and Igor I. Tkachev. Relativistic turbulence: A long way from preheating to equilibrium. *Phys. Rev. Lett.*, 90(12):121301, Mar 2003. doi: 10.1103/PhysRevLett.90.121301.
- [40] L. F. Mollenauer, R. H. Stolen, and J. P. Gordon. Experimental observation of picosecond pulse narrowing and solitons in optical fibers. *Phys. Rev. Lett.*, 45: 1095–1098, Sep 1980.
- [41] C. Mora and Y. Castin. Extension of bogoliubov theory to quasicondensates. *Phys. Rev. A*, 67:053615, 2003.
- [42] J. E. Moyal. Quantum mechanics as a statistical theory. *Proc. Cambridge Philos. Soc.*, 45:99, 1949.

- [43] A. H. Mueller, A. I. Shoshi, and S. M. H. Wong. On Kolmogorov wave turbulence in QCD. *Nucl. Phys.*, B760:145–165, 2007. doi: 10.1016/j.nuclphysb.2006.10.023.
- [44] Ö. E. Müstecaplıoğlu, M. Zhang, and L. You. Spin squeezing and entanglement in spinor condensates. *Phys. Rev. A*, 66:033611, September 2002.
- [45] Boris Nowak, Denes Sexty, and Thomas Gasenzer. Superfluid Turbulence: Non-thermal Fixed Point in an Ultracold Bose Gas. *Phys. Rev. B*, 84:020506(R), 2011.
- [46] Boris Nowak, Jan Schole, Denes Sexty, and Thomas Gasenzer. Nonthermal fixed points, vortex statistics, and superfluid turbulence in an ultracold Bose gas. *Phys. Rev. A*, 85:043627, 2012.
- [47] L. Onsager. Statistical hydrodynamics. *Nuovo Cim. Suppl.*, 6:279, 1949.
- [48] C.J. Pethick and H. Smith. *Bose-Einstein condensation in dilute gases*. Cambridge University Press, 2006.
- [49] D. S. Petrov, G. V. Shlyapnikov, and J. T. M. Walraven. Regimes of quantum degeneracy in trapped 1d gases. *Phys. Rev. Lett.*, 85:3745, October 2000.
- [50] L. P. Pitaevskii and S. Stringari. *Bose-Einstein Condensation*. Clarendon Press, 2003.
- [51] A. Polkovnikov. Phase space representation of quantum dynamics. *Annals of Physics*, 325(8):1790–1852, 2010.
- [52] V.N. Popov. *Functional Integrals in Quantum Field Theory and Statistical Physics*. Reidel, Dordrecht, 1983.
- [53] Arttu Rajantie and Anders Tranberg. Counting Defects with the Two-Point Correlator. *JHEP*, 1008:086, 2010. doi: 10.1007/JHEP08(2010)086.
- [54] L.F. Richardson. The supply of energy from and to atmospheric eddies. *Proc. R. Soc. Lond. A*, 97:354–373, 1920.
- [55] I. Salasnich, A. Parola, and L. Reatto. Effective wave equations for dynamics of cigar-shaped and disk-shaped Bose condensates. *Phys. Rev. A*, 65:043614, 2002.
- [56] A. Scheffers and D. Kelletat. Sedimentologic and geomorphologic tsunami imprints worldwide—a review. *Earth-Science Reviews*, 63(1–2):83 – 92, 2003. ISSN 0012-8252.
- [57] Maximilian Schmidt, Sebastian Erne, Boris Nowak, Denes Sexty, and Thomas Gasenzer. Nonthermal fixed points and solitons in a one-dimensional Bose gas. *arXiv:1203.3651 [cond-mat.quant-gas]*, 2012.

- [58] J. Schmiedmayer. *Private communication*. Atominstitut TU Wien.
- [59] J. Schmiedmayer and R. Folman. Miniaturizing atom optics: From wires to atom chips. *C. R. Acad. Sci. Paris IV*, 2:333, 2001.
- [60] S. I. Shevchenko. On the theory of Bose Gas in a nonuniform field. *Sov. J. Low. Temp. Phys.*, 18:223, 1992.
- [61] I. Shvarchuck, Ch. Buggle, D. S. Petrov, K. Dieckmann, M. Zielonkowski, M. Kemmann, T. G. Tiecke, W. von Klitzing, G. V. Shlyapnikov, and J. T. M. Walraven. Bose-einstein condensation into nonequilibrium states studied by condensate focusing. *Phys. Rev. Lett.*, 89:270404, Dec 2002.
- [62] A. Sinatra, C. Lobo, and Y. Castin. The truncated wigner method for Bose-condensed gases: limits of validity and applications. *J. Phys. B*, 35(17):3599, 2002.
- [63] Roger K. Smith. Travelling waves and bores in the lower atmosphere: the ‘morning glory’ and related phenomena. *Earth-Science Reviews*, 25(4):267 – 290, 1988. ISSN 0012-8252.
- [64] S. Stringari. Collective excitations of a trapped bose-condensed gas. *Phys. Rev. Lett.*, 77:2360–2363, Sep 1996.
- [65] Lewi Tonks. The complete equation of state of one, two and three-dimensional gases of hard elastic spheres. *Phys. Rev.*, 50:955, November 1936.
- [66] Andreas Weller. *Dynamics and Interaction of Dark Solitons in Bose-Einstein Condensates*. PhD thesis, Kirchhoff-Institut für Physik, 2009.
- [67] E. Witkowska, P. Deuar, M. Gajda, and K. Rzążewski. Solitons as the early stage of quasicondensate formation during evaporative cooling. *Phys. Rev. Lett.*, 106:135301, Mar 2011.
- [68] C. N. Yang and C. P. Yang. Thermodynamics of a one-dimensional system of bosons with repulsive delta-function interaction. *Journal of Mathematical Physics*, 10:1115, 1969.
- [69] V.E. Zakharov and A.B. Shabat. Exact theory of two-dimensional self-focusing and one-dimensional self-modulation of wave in nonlinear media. *JETP*, 34:62, 1972.
- [70] V.E. Zakharov and A.B. Shabat. Interaction between solitons in a stable medium. *JETP*, 37(5):823, 1973.
- [71] WH Zurek. Cosmological experiments in superfluid helium? *Nature*, 317(6037): 505–508, 1985.

- [72] Wojciech Hubert Zurek. Cosmological experiments in condensed matter systems. *Phys. Rep.*, 276:177, 1996. URL <http://arxiv.org/abs/cond-mat/9607135>.

Danksagung

Zuerst möchte ich Herrn Prof. Thomas Gasenzer dafür danken, dass ich Mitglied seiner Arbeitsgruppe sein durfte und vor allem, dass er während dem Entstehen dieser Arbeit mit Rat und Tat zur Seite stand. Des Weiteren möchte ich mich bei Herrn Prof. Schmiedmayer für die Einladung nach Wien, den wunderbaren Aufenthalt, die Zusammenarbeit und die Zweitkorrektur meiner Arbeit bedanken. Es war eine Ehre von dem physikalischen Verständnis und den Eingebungen dieser Personen zu profitieren. In diesem Zusammenhang gilt besonderer Dank auch Robert Bücker, für die großartige Zusammenarbeit und Hilfe.

Eine wichtige Rolle hat Boris Nowak während der Entstehung dieser Arbeit gespielt. Unsere Diskussionen waren ein wichtiger Bestandteil zum gelingen dieser Arbeit. Besonderer Dank gilt auch seiner andauernden Bereitwilligkeit Zeit für Fragen, Diskussionen oder die Korrektur meiner Arbeit einzuräumen.

Weiterhin möchte ich der gesammten Arbeitsgruppe für die angenehme Atmosphäre und die bereitwillige Hilfe bei Fragen oder der Korrektur danken. Im besonderen bei: Jan Schole, Sebastian Bock, Roman Hennig, Martin Trappe und Jan Zill.

Zu guter Letzt möchte ich meinen Freunden und meiner Familie danken, die mich in allen Höhen und Tiefen unterstützt haben. Dies gilt umso mehr für meine Freundin Jeanne die in Zeiten mit und ohne Zeit, in Frust und Euphorie an meiner Seite stand.

Erklärung:

Ich versichere, dass ich diese Arbeit selbstständig verfasst habe und keine anderen als die angegebenen Quellen und Hilfsmittel benutzt habe.

Heidelberg, den 30. Juli 2012
.....